KEY DIGITAL-ROF MOBILE-FRONTHAUL TECHNOLOGIES WITH STATISTICAL DATA COMPRESSION AND MULTIBAND MULTIPLEXING

A Dissertation
Presented to
The Academic Faculty

by

Mu Xu

In Partial Fulfillment
of the Requirements for the Degree
Doctor of Philosophy in the
School of Electrical and Computer Engineering

Georgia Institute of Technology
May, 2018

KEY DIGITAL-ROF MOBILE-FRONTHAUL TECHNOLOGIES WITH STATISTICAL DATA COMPRESSION AND MULTIBAND MULTIPLEXING

Approved by:

Dr. Gee-Kung Chang, Advisor
School of Electrical and Computer Engineering
Georgia Institute of Technology

Dr. John R. Barry
School of Electrical and Computer Engineering
Georgia Institute of Technology

Dr. Xiaoli Ma
School of Electrical and Computer Engineering
Georgia Institute of Technology

Dr. Jun Xu
School of Computer Science
Georgia Institute of Technology

Dr. Mary Ann Weitnauer
School of Electrical and Computer Engineering
Georgia Institute of Technology

Date Approved: February 27, 2018

To my parents and my beloved wife Mingwen,

for their unconditional support and encouragement

ACKNOWLEDGEMENTS

I would like to take this great opportunity to express my sincere gratitude to the many people who made this dissertation possible.

Foremost, I am very grateful to my advisor, Professor Gee-Kung Chang, for his guidance, patience, and continuous support. It is my great honor and pleasure to work with him as his student. As an old Chinese idiom said, he who teaches me one day is respected as my father for life. His vast industry experience and remarkable academic leadership were catalysts for my growth. His passion and optimism continuously encouraged us generation after generation to do what a professional researcher should do.

I would also like to thank Professor Xiaoli Ma, Professor Mary Ann Weitnauer, Professor John Barry, and Professor Jun Xu for serving as my committee members and their valuable suggestions on my dissertation. I am also deeply thankful for Dr. Xiang Liu, Dr. Sufian Mitani, and Dr. Zhensheng Jia for their guidance, instructions, criticism and encouragements during my Ph.D. study, which expanded my research scope and enriched my working experiences.

I am certainly appreciative and thankful for all my colleagues in Fiber Wireless Integration and Networking (FiWIN) group. Their advice and collaboration as well as friendship have supported my professional and personal life during the five-year Ph.D. career. Thanks to Junwen Zhang, Cheng Liu, Ming Zhu, Jing Wang, Lin Cheng, Feng Lu, Jianyu Zhen, Shuyi Shen, Yahya Alfadhli, Hyung Joon Cho, Hyunwoo Cho, Chih-Heng

Yan, Jiun-Yu Sung, Beilei Wu, Qi Zhou, Rui Zhang, Shuang Yao, Siming Liu, Dicky Hsu, Peng-Chun Peng, and many other graduate students whom I have worked with.

Lastly, I would like to thank my family for all their love and encouragement. For my parents, Guoyun Xu and Xianping Wei, who did their best to give me the best education and always provide me the unconditional and uncompromised support. They raised me up and taught me how to become a considerate and responsible man for the family and the society. Saving the best for the last, I would like to thank my lovely wife, Mingwen Yang. No matter with success or depression, your constant support and love were one of the most important motivations throughout my Ph.D. life. Thank you and thank you all.

TABLE OF CONTENTS

LIST OF TABLES

LIST OF FIGURES

LIST OF SYMBOLS AND ABBREVIATIONS

ADC	Analog to digital converter
A-RoF	Analog radio over fiber
AxC	Antenna component
BBG	Baseband group
BBU	Baseband unit
BER	Bit error rate
BSC	Base station controller
CA	Carrier aggregation
CAP	Carrierless amplitude phase modulation
CC	Component carrier
CDF	Cumulative distribution function
CDMA	Code division multiple access
CE	Computational efficiency
CFO	Carrier-frequency offset
CO	Central office
CoMP	Coordinated multipoint transmission
CPRI	Common public radio interface
CU	Central unit
DAC	Digital to analog converter
DA-MZM	Dual-arm Mach-Znhder modulator
DBA	Dynamic bandwidth allocation
DC	Direct current

DCC	Digitized component carrier
DFB	Distributed feedback
DML	Directly modulated lasers
DMT	Discrete multi-tone
DOCSIS	Data over cable service interface specification
DPCM	Differential pulse code modulation
DP-IQM	Dual-polarization IQ modulator
D-RoF	Digital Radio over Fiber
DSP	Digital signal processing
DU	Distributed unit
EAM	Electro-absorption modulators
ECL	External cavity laser
EDFA	Erbium doped fiber amplifier
eMBB	Enhanced mobile broadband
eNB	Enhanced node B
E-UTRA	Evolved universal terrestrial radio access
EVM	Error vector magnitudes
FBA	Fixed bandwidth allocation
FBMC	Filter-bank multi-carrier
FBNQ	Fitting based nonlinear quantization
FDE	Frequency domain equalizer
FDM	Frequency division multiplexing
FEC	Forward error correction
FFT	Fast Fourier transform
FM-HD	Filed-modulation plus heterodyne-detection

FS	Functional split
FSE	Fast statistical estimation
GSM	Global system for mobile communication
GTC	GPON-transmission-convergence
HFC	Hybrid fiber coax
HTH	Human to human
ICC	Inter-channel crosstalk
IF	Intermediate frequency
IFFT	Inverse Fast Fourier transform
IM-DD	Intensity-modulation plus direct-detection
IoT	Internet of things
IOTA	Isotropic orthogonal transform algorithm
ISI	Inter-symbol interference
LDPC	Low density parity check
LO	Local oscillator
LTE	Long term evolution
MEC	Mobile edge computing
MFH	Mobile fronthaul
MMSE	Minimum mean-square error
mMTC	Massive machine-type communication
MMW	Millimeter wave
MPTP	Multi-point to point
MZM	Mach-Zehnder modulators
NGFI	Next generation fronthaul interface
NOMA	Non-orthogonal multiple access

NR	New radio
NSC	Nyquist supper channel
OBI	Optical beating interference
OBSAI	Open base station architecture initiative
OCS	Optical carrier suppression
OFDM	Orthogonal frequency-division multiplexing
OOB	Out of band
OQAM	Offset quadrature amplitude modulation
PAM	Pulse amplitude modulation
PAPR	Peak-to-average power ratio
PBS	Partial bit sampling
PC	Polarization controller
PCM	Pulse code modulation
PD	Photo detector
PDCP	Packet data convergence protocol
PDF	Probability density function
PHY	Physical layer
PON	Passive optical networks
PPN	Polyphase network
PSB	Physical synchronization block
PTMP	Point to multi point
PTMP	Point to multi point
PTP	Point to point
PTP	Point to point
QDP	Quadrature duobinary processing

QPSK	Quadrature phase shift keying
R&A	Report-and-adjust
R&G	Request-and-grant
RAN	Radio access network
RAT	Radio access technology
RAU	Radio access unit
RE	Radio equipment
REC	Radio equipment controller
RLC	Radio link control
RRC	Radio resource control
RRH	Remote radio head
RRS	Remote radio systems
RSOA	Reflective semiconductor optical amplifier
SCM	Subcarrier multiplexing
SDS	Service data streams
SE	Spectral efficiency
SINR	Signal-to-interference-plus-noise ratio
SQNR	Signal-to-quantization-noise ratio
SRRC	Square-root raised-cosine
SSB-DD	Single-side-band and direct-detection
SSBI	Signal-to-signal beating interference
SSMF	Standard single mode fiber
TDM	Time-division multiplexing
TE	Transmission efficiency
TFG	Truncated folded Gaussian

UE	User equipment
UL	Uplink
uRLLC	Ultra-reliable low latency communication
VT	Virtual tone
WDM	Wavelength division multiplexing
WLAN	Wireless local access network

SUMMARY

The continuously-growing demand on high-speed internet, high-definition TV, and real-time entertainment services has created a great challenge for future broadband access networks. The emerging new services, such as virtual reality and 5G-New Radio, will quickly deplete the bandwidth resource of current passive optical networks (PON), mobile fronthaul (MFH), and hybrid fiber coax (HFC) networks. On the other hand, under the impact of cell densification and spectral aggregation, significantly increased complexity in network scheduling and coordination is inevitable. Those trends force we researchers to think about revolutionary technologies empowering next-generation MFH with higher capacity and lower latency. Among them, fiber wireless integration and networking are promising solutions which integrate the fiber and wireless resources and optimize the both in a mobile fronthaul system as a whole.

MFH based on analog RoF (A-RoF) has been deeply studied recently. A-RoF based MFH has high bandwidth efficiency and simple receiver architecture. But A-RoF schemes also suffer from nonlinear degradations in power amplifiers as well as fading from chromatic dispersions. Besides, to realize a point-to-multi-point (PTMP) transmission in an A-RoF up-link (UL) remains to be a challenge. On the other hand, function-split (FS) schemes, e.g., PHY-I-Split and Mac-Split have been proposed, which could tremendously reduce the MFH data rate. Nevertheless, such a reduction is at an expense of higher complexity and cost at the radio access unit (RAU) in terms of MIMO processing and coordinated multipoint (CoMP) transmission. Furthermore, according to the in-progress 5G standards from ITU-R and 3GPP-NR, three different usage scenarios are defined,

namely, enhanced mobile broadband, machine-type communication, and low-latency vehicular communication. Thus, the compatibility with those different radio access technologies (RAT) could also be a challenge for FS based schemes.

Recently, as a candidate to support MFH, the advantage of digital RoF (D-RoF) scheme including common public radio interface (CPRI) may be under-estimated. Although, D-RoF features lower transmission efficiency (TE), it inherits part of the advantages from both A-RoF and FS. D-RoF is format agnostic with simple hardware implementation at RAUs. Meanwhile it benefits from digitization with high robustness against nonlinear degradation. Error free transmission can be obtained when using forward error correction (FEC) coding. A low-cost time-division multiplexing (TDM) based PTMP UL scheme is also highly realizable.

In this thesis work, to improve the bandwidth efficiency of D-RoF systems, the studies in the following directions have been made. Fast statistical estimation (FSE) is proposed for data compression in quantization process. Compared with existing schemes, the computational-complex fitting process is simplified and high compression radio (15 to 8 bit) can be obtained with insignificant signal-quality degradation. Nevertheless, the Gaussian distribution assumption limits the FSE only applicable to orthogonal-frequency-division-multiplexing (OFDM) format. To develop a generalized method for other different radio modulation formats, Lloyd algorithm based method is also studied. Traditional Lloyd algorithm is computational complex and in our research, a relaxed Lloyd algorithm is proposed with a good trade-off between quantization accuracy and computing speed. Meanwhile, differential coding is also combined with statistical based data compression to further reduce the quantization noise and increase the compression gain.

Other than bandwidth efficiency, another major issue in D-RoF based MFH is the data multiplexing among multiple distributed RAUs. Traditional TDM provides a matured solution but following that more attention is focused on supporting delay sensitive services in 5G, TDM may find itself insufficient in the flexibility and latency as a role in supporting ultra-reliable low latency communication (uRLLC). To mitigate such an issue, we demonstrate an offset-QAM carrier-less amplitude and phase modulation (OQAM-CAP) technique for spectral efficient multi-user transmission. The performances of OQAM-CAP and regular QAM-CAP are compared and their different applicable scenarios are also discussed.

Furthermore, except from the works on D-RoF MFH, this dissertation also briefly reviewed the research on modulation formats and digital signal processing (DSP) techniques in fiber-wireless integrated systems, such as filter-bank multi-carrier (FBMC) and bit/power loading in multiband signals. Working with advanced data compression and multi-band multiplexing, these DSP algorithms could help to improve the spectral efficiency as well as signal quality of the system, which makes them unneglectable contributors for next-generation digital/analog MFH supporting 5G mobile data networks.

CHAPTER 1. INTRODUCTION

1.1 Motivation

Driven by the continuous demands on faster connection speed and ubiquitous wireless signal coverage, the concept of fifth generation (5G) mobile data network arises, which is commonly forecasted to be deployed around 2020 [1]. Not only boosting the network throughput, 5G also brings revolutionary changes to the mobile data communication and even affecting the way we think and interact. Among all the attractive features of 5G, higher-RF-band exploration, discrete-spectral-band utilization, and small-cell deployment are of great importance to bring about two to three orders of improvement in system capacity. As shown in Figure 1, following previous industrial revolutions made by steam power, electricity, information technology, 5G is regarded as a key contributor together with artificial intelligence, cloud computing, VR and AR to stimulate the coming 4th Generation of Industrial Revolution.

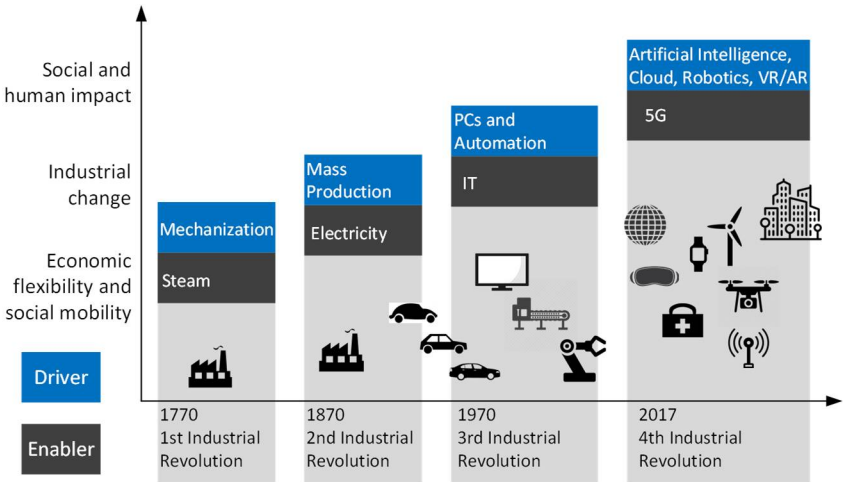

Figure 1. 5G and 4th Industrial Revolution.

Except from traditional mobile data communication, machine-type communication (MTC) and Internet of Things (IoT) are becoming the major driving power for new 5G technologies. New emerging applications in MTC and IoT gain attentions from both industry and academic area, such as AR, VR, cloud computing, self-driving car and so on. According to the in-progress 5G standards from ITU-R and 3GPP-NR [2], [3], those uses are grouped into three usage scenarios including enhanced mobile broadband (eMBB), massive machine-type communication (mMTC), and ultra-reliable and low latency communication (uRLLC) as shown in Figure. 2. Moreover, key enhancements in eight aspects are proposed by IMT-Advanced and IMT-2020, which include peak data rate (Gbit/s), user experienced data rate (Mbit/s), spectrum efficiency, mobility (km/h), latency (ms), connection density (devices/km^2), network energy efficiency, and area traffic capacity (Mbit/s/m^2). The importance of each key parameter is different in different using scenarios. For example, eMBB may emphasize on area traffic capacity and peak data rate while URLLC mainly considers latency and mobility as more important factors. Furthermore, after recent debating, major standard bodies reach a consensus to adopt both low density parity check (LDPC) and polar codes as data and control channel coding options respectively [4]. Thus, it can be inferred that except from higher throughput, being adaptive to fit different needs in varying application scenarios and making use of advantages from different unique technologies become a key point for building future 5G fiber-wireless converged heterogeneous networks.

The selected updates in key parameters and technologies in 5G-NR are shown in Table 1 [2]. It can be observed that some technical specifications are inherited from existing LTE standards. For example, OFDM is still considered as the major format in the downlink

of 5G-NR. The subcarrier spacing is based on the grid of 15 kHz. QPSK, 16-QAM, and 64-QAM are still adopted. Time division duplex is considered as the main duplex option. However, there are also some new changes which distinguish 5G-NR out of traditional wireless data communication scheme. The first change is about new bandwidth exploration. Except from centimeter waves from 0.5 to 6 GHz, new millimeter-wave carriers distributed from 10 to 100 GHz are going to be used. Non-orthogonal multiple access (NOMA) will be coexisted with orthogonal multiple access to provide higher flexibility and large system performance margin. Higher-order modulation format (1024 QAM) and larger-scale MIMO are proposed for high-capacity wireless links.

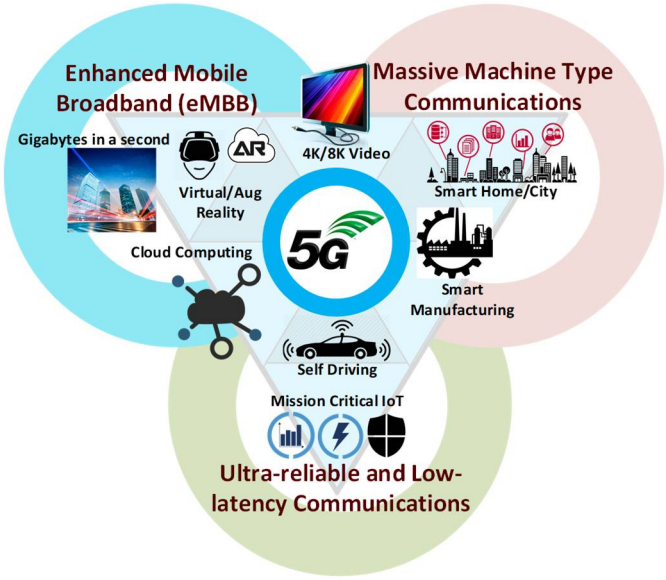

Figure 2. 5G usage scenarios.

Table 1 – Updates about 5G New-Radio Standardization

Operation Frequencies	0.5 – 100 GHz (0.5 – 6 GHz; 6 – 24 GHz; 24 – 100 GHz)
Waveform	DL: CP-OFDM; UL: SC-FDM or CP-OFDM
Subcarrier Spacing	15 kHz × 2^n
Duplex	TDD
Multiple Access Scheme	Joint **orthogonal** and **non-orthogonal** multiple access
Channel Coding	eMBB data channel: **LDPC**; eMBB control channel: **Polar Code**
Modulation Format	BPSK, QPSK, 16QAM, 64QAM, 256QAM, 1024QAM
Channel Bandwidth	0.18 – 1.4 MHz (IoT); 1.4 – 20 MHz (Current LTE); 20 – 400 MHz (eMBB)
MIMO Implementation	DL: Up to 32 streams; UL: 4 streams

Recent progresses in fiber-wireless integration and networking motivate photonic researchers to think about how optics could help 5G mobile data networks. The selected photonic technologies contributing to 5G are listed in Figure 3. They mainly fall into three categories: mobile fronthaul and radio access network; photonics assisted wireless systems; and high-capacity communication systems in mobile core network. In the area of mobile fronthaul and radio access network, MFH architecture based on time/wavelength-division

multiplexed passive optical network (TDM/WDM PON), A-RoF, as well as D-RoF are potential candidates and some challenges exist on supporting high-density small cells and all-spectrum carrier aggregation. Photonics assisted wireless systems recently become hot research topics for its capability to greatly extend the coverage, capacity, or functions of traditional wireless systems [5]. They comprise optical millimeter wave (MMW) and sub-terahertz systems, free-space optics and visible light communications, and photonics assisted coordinated multi-point (CoMP) and network MIMO. Other than the above two categories focusing on access network or user equipment, it is undeniable that photonics as well as fiber communication systems also play major roles in the mobile core network to support 5G. 100G/400G long-haul transmission, optical inter and intra data center connects, as well as high-capacity X-Haul network are the major parts in this category.

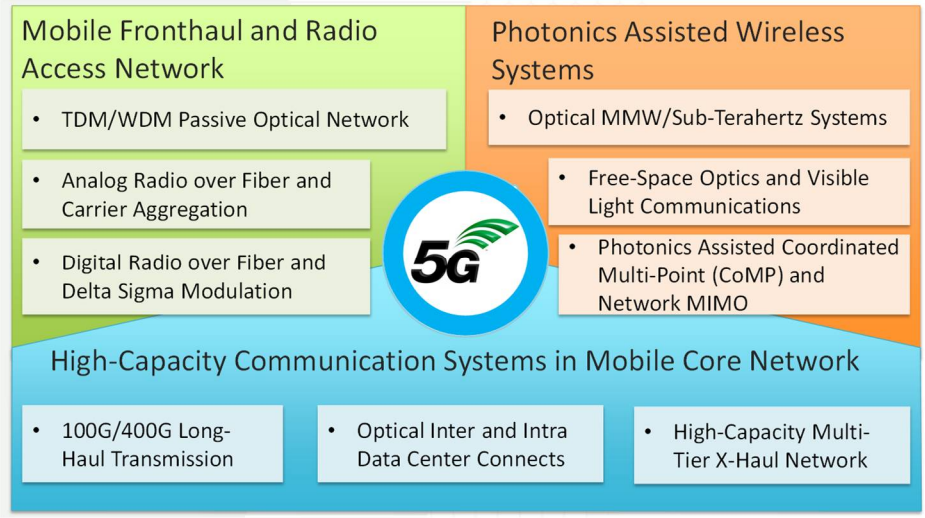

Figure 3. Photonic technologies as the fundamental behind 5G.

Among these areas, great challenges arise in mobile fronthaul systems because that most of the interactions between wireless and fiber take place behind it. In the following part of the introduction, current status of MFH will be reviewed and the technical issues

will be analyzed. The potential solutions will also be discussed in the remaining chapters of the dissertation.

1.2 Mobile Fronthaul Network Architectures

Among all the attractive features of 5G, higher-RF-band exploration, discrete-spectral-band utilization, and small-cell deployment are of great importance to bring about two to three orders of improvement in system capacity, which is also consistent with the trends of spectral aggregation and cell densification. An overall conceptual diagram of a future 5G network system with spectral aggregation and cell densification is depicted in Figure 4(b). Spectral aggregation could provide us higher radio bandwidth while it also enables the utilization of discrete fragmented bands and the coexistence of different radio-access-technologies (RATs). Meanwhile, through higher-RF-band exploitation and frequency reuse, massive deployment of small cells brings heterogeneous and ubiquitous wireless signal coverage with greatly improved subscriber experience. For comparison, Figure 4 also demonstrates the evolution of mobile fronthaul architecture from traditional distributed radio-access network (RAN) to cloud RAN (C-RAN). Date back to late 1990s until 2010, distributed RAN dominates mobile fronthaul/backhaul link and the major transmission media in MFH is copper as shown in Figure 4(a). Most base stations were connected via digital subscriber line (DSL) or coax cable. The network is based on a distributed architecture with enhanced node B (eNB) deployed at different macro cells. There are S2 and X2 links physically or logically connecting the base station controller (BSC) to eNBs and between two eNBs respectively where Ethernet packets are transmitted from point to point. The major problem of distributed RAN is that it lacks the flexibility

and scalability to support the deployment of small cells and network capacity is also seriously limited by the coax cable as well as the distributed architecture.

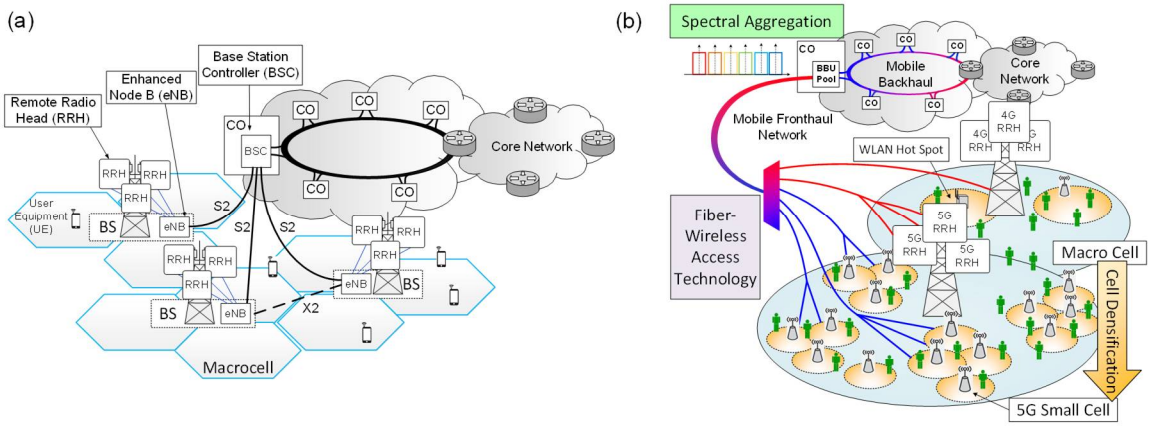

Figure 4. (a) traditional distributed radio access network (RAN) and (b) cloud RAN.

As a solution to mitigate the aforementioned challenges, the concept of cloud radio access network (C-RAN) has been proposed [6] - [8]. In C-RAN, baseband units (BBUs) are separated from the base stations (BSs) and centralized into the BBU-Pool at the CO, which connects hundreds of distributed remote radio heads (RRHs) and small cells as shown in Figure 4(b). The BBU-Pool is empowered with efficient data and information processing technologies such as cloud computing and functioning virtualization for the ease of large-scale dynamic and centralized management as well as resource allocation. In C-RAN architecture, optical fibers are considered to be an ideal media to provide a low-loss high-capacity solution to build fiber-wireless integrated links to enable data and information exchange between the BBU-Pool and distributed cells.

Although through centralized control and optimization, C-RAN could potentially achieve best radio performance, it is still not a perfect solution and exhibits some issues regarding system latency, flexibility, and nonlinear channel penalties. To meet the 5G-NR

requirements with diverse services and spectrum including enhanced mobile broadband, mission-critical IoT, and massive machine-type communications, current 4G MFH architectures need to be upgraded to meet the different latency and throughput requirements in different scenarios. Thus, the legacy C-RAN is evolving to Next-Generation Fronthaul Interface (NGFI) which calls for relocating the functionalities to the remote radio unit (RRU) to alleviate the processing burden in mobile fronthaul, namely, functional-split [9]. This design will result in two functional-split segments: radio cloud center (RCC) and radio access unit (RAU). The functionalities can be reconfigured and organized depending on the selected splitting point. For example, it can perform the RF functions only at the remote radio head (RRH) with a simple structure, known as Option-8 or so-called A-RoF. Or it can inherit a part or all the functions in physical (PHY) layer into the RAU, which is known as Option-7. Except from these splitting options, there are also many other splitting points. Each of them has its unique properties and advantages which may distinguish them fitting for different application scenarios. Therefore, it is proposed in [10] that a flexible function split can also be considered where the different split options can be coexisted and tuned dynamically over time based on different application environments.

Different functional-split option can be classified into four main categories as shown in Figure 5 below. It was mentioned in the previous part that in NGFI different functions between the central unit (CU) and distributed unit (DU) will be reorganized or redistributed. There are 8 functional-split options defined and recommended by 3GPP [11]. Different options have different requirements in terms of bandwidth, latency, jitter, and synchronization. Option 1 and Option 2 are the fully distributed architecture where most

of the functions are aggregated at the DU and CU only to perform radio resource control and data packet performance control. In these two options, Ethernet packets are transmitted between CU and DU. There is almost no wireless overhead which helps to achieve high transmission efficiency, low latency, and low synchronization requirements. But the distributed architecture makes them incompatible with MIMO and coordinated multipoint (CoMP) transmission. It is worth noting that the resources in these options can be aggregated at network edge, fascinating mobile edge computing for delay sensitive services. Option 3 to Option 5 belong to the intermediate status between distributed and partly centralized architectures. On the other hand, Option 6 and Option 7 are partly centralized options, they may realize a good trade-off between transmission bandwidth efficiency and radio performance. However, they have high synchronization and latency requirements since the resource blocks of LTE need to be aligned between the DU and RRUs. Option 8 is a fully centralized option. Some researchers also refer it as the A-RoF option. Since the LTE component carriers are not modified, MFH and air transmission can be seamlessly integrated together. Best radio performance can be obtained with centralized coordination and scheduling, which makes it fully compatible with CoMP. However, mobile fronthaul on this option will have very strict requirements on latency control and thus, the transmission distance is limited.

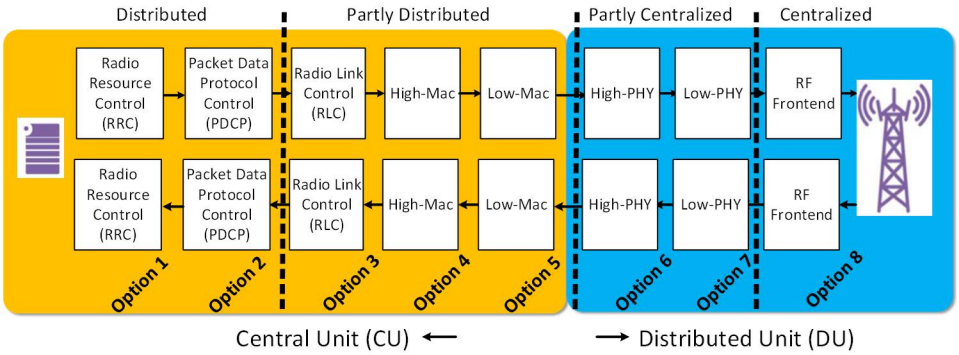

Figure 5. Conceptual diagram of functional split in mobile fronthaul.

With reconfigurable and multi-coexisted functional-split options, NGFI is proposed in the standard of IEEE 1914.1 [12]. Figure 6 shows a conceptual diagram about NGFI based mobile fronthaul network. Two-layer architecture is introduced, where Fronthaul-I is a network to connect a distributed unit (DU) and several RRUs and Fronthaul-II is used to connect central unit (CU) and multiple DUs. The location of CU could be different for different application environments. For example, CU is located at the (transport) aggregation layer, which could correspond to massive machine-type-communication scenario supporting a large number of smart things. For enhanced mobile broadband, the CU could be deployed at the access layer to boost the peak throughput and average data rate. Meanwhile, forward and backward compatibility need to be considered here. Those legacy fronthaul infrastructures inherited from 3G and 4G systems will be incorporated into Option 1 and Option 2. Small cell densifications are supported by Option 7 or Option 8. Reconfigurable functional split, or Option X (including Option 3 to 6) will also be implemented regarding the system needs and latency tolerance. Table 2 compares the application scenarios of different functional-split options in NGFI. Such a two-layer architecture could help to realize a good trade-off between latency and capacity with the implementation and switching among different options. For some services with stringent

delay requirements, like unmanned self-driving car, security, positioning, and health care, DU can make a quick decision without sending the dataflow to CU and waiting for its responses. However, for some tasks requiring complex computing and scheduling, CU can be involved with the high-performance cloud computational resources and large capacity storage space inside it. In tier-I fronthaul network, because of the limited transmission distance and relatively small link throughput, both A-RoF and D-RoF can be good candidates. Their different properties and applicable situations will be illustrated in the following parts.

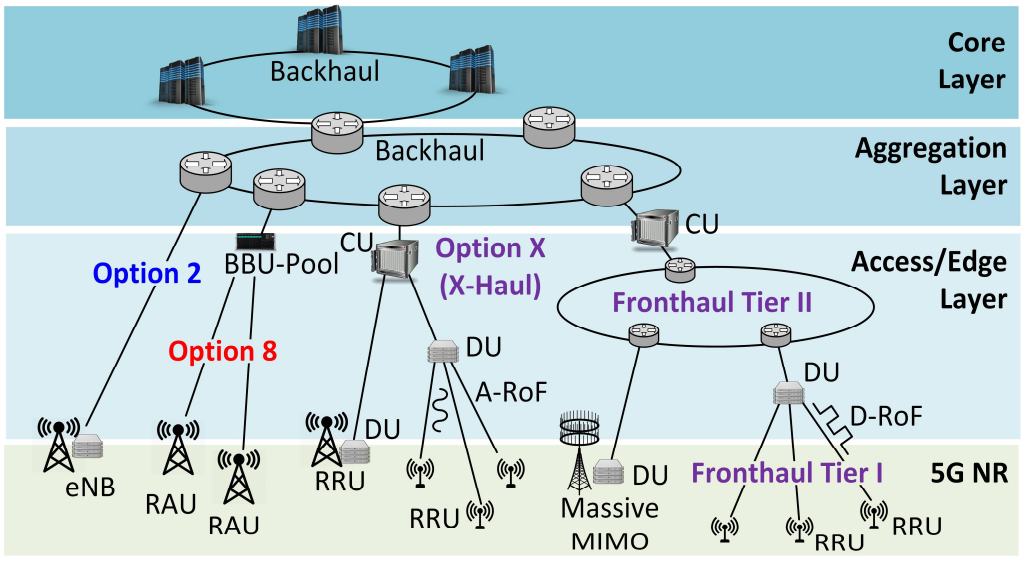

Figure 6. Conceptual diagram of next-generation fronthaul interface (NGFI).

Table 2 – Comparison of different split options in NGFI

Option	Description	Applications
Option 1	RRC-PDCP split: In this split option, RRC is in the central unit. PDCP, RLC, MAC, physical layer and RF are in the distributed unit, thus the entire user plane is in the distributed unit.	Edge computing or low-latency transmission
Option 2	PDCP-RLC split: In this split option, RRC, PDCP are in the central unit. RLC, MAC, physical layer and RF are in the distributed unit.	Low-latency transmission (Already standardized)
Option 3	Intra RLC split: Low RLC (partial function of RLC), MAC, physical layer and RF are in distributed unit. PDCP and high RLC (the other partial function of RLC) are in the central unit.	Low-latency transmission; Implementing intra-gNB RAN-based mobility; Fronthaul flow control
Option 4	RLC-MAC split: MAC, physical layer and RF are in distributed unit. PDCP and RLC are in the central unit.	Not recommended by 3GPP
Option 5	Intra MAC split: RF, physical layer and some part the MAC layer (e.g. HARQ) are in the distributed unit. Upper layer is in the central unit.	Collecting UE's statistics Fronthaul activities measure/estimate
Option 6	MAC-PHY split: The MAC and upper layers are in the central unit (CU). PHY layer and RF are in the DU. The interface between the CU and DUs carries data, configuration, and scheduling-related information (e.g. MCS, Layer Mapping, Beamforming, Antenna Configuration, resource block allocation, etc.) and measurements.	Centralized scheduling Resource pooling at MAC layer in the central office
Option 7	Intra PHY split: In the UL, FFT, and CP removal reside in the DU. Two sub-variants are described below. Remaining functions reside in the CU. In the downlink, iFFT and CP addition reside in the DU. Three sub-variants are described below. The rest of the PHY resides in the CU. Multiple realizations are possible	Centralized scheduling Compatible with joint processing and coordinated multi-point transmission Massive MIMO High-performance radio
Option 8	Option 8 allows to separate the RF and the PHY layer. This option permits centralization of processes at all protocol layer levels, resulting in very tight coordination of the RAN. This allows efficient support of functions such as CoMP, MIMO, load balancing, mobility. Realizations including A-RoF, D-RoF, and delta-sigma modulation	Low-cost RRUs Short-distance PTP transmissions Efficient support of functions such as CoMP, MIMO, load balancing, mobility

1.3 Data Transmission Interface in Mobile Fronthaul

There are different data transmission schemes proposed to support C-RAN, including the well-known common public radio interface (CPRI) [13]. A CPRI based mobile fronthaul initiates with digitizing the baseband LTE component carrier (CC) with I/Q streams at BBU-Pool and then transmits the quantized bits to the RRHs. Each digitized sample contains 15 digits plus 1-digit control words. And they are contained in one antenna component (AxC). Within an RRH, the CC will be re-constructed based on the digitized bits before sent to the radio equipment (RE). However, CPRI is a bandwidth consuming method. After digitization, one 20-MHz LTE band is converted into an about 900 Mbit/s

on-off-keying (OOK) signal. For an enhanced LTE macro cell with three sectors and 8-by-8 MIMO, it may even require a speed of 150 Gbit/s which is far beyond the capability of today's access technology. To overcome the drawback of low spectral efficiency in CPRI, channel aggregation/de-aggregation (CA/CDA) is proposed in the mobile fronthaul system [14] - [19] as shown in Figure 7. In such a scheme, multiple LTE signals are transmitted with frequency division multiplexing (FDM) over one wavelength-division-multiplexed (WDM) channel and thus the spectral efficiency can be greatly improved because there is no digital quantization process. For example, in [16], 1.5-GHz RF bandwidth is abundant to support 48 20-MHz LTE signals. The FDM could be realized by pure DSP scheme [14] - [17] or digital-analog hybrid method [18], [19]. However, current CA/CDA based mobile fronthaul is built upon a point-to-point (PTP) architecture with WDM passive optical network (PON), which also induces some problems. Above all, PTP architecture lacks the scalability to support cell splitting and expansion in 5G networks. With increased number of small cells, the available wavelengths of a WDM PON will be quickly used up and deploying dense WDM (DWDM) multiplexers as well as transceivers is too expensive. On the other hand, uplink (UL) transmission will become a challenging issue if using subcarrier multiplexing (SCM) or FDM schemes [19] - [22] in small-cell mobile fronthaul. Because each small cell is an independent unit, the optical signals among different small cells are asynchronous and incoherent with various phase and polarizations. When they beat with each other inside a photo detector (PD), the signal quality will be seriously degraded by optical beating interference (OBI) and phase noise. Nevertheless, in [19] - [22], complex optical coherent receivers are used and large guard bands have to be remained between adjacent carrier components or FDM channels, which increases the cost

and sacrifices the spectral efficiency. Moreover, OBI cannot be thoroughly eliminated through coherent receiving techniques due to the imperfection of the 90/180-degree optical hybrid. The residual OBI will still deteriorate the signal quality in the above works.

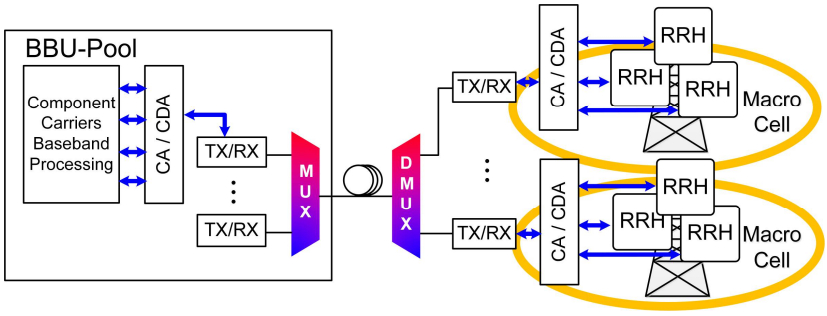

Figure 7. Architecture of channel aggregation/de-aggregation (CA/CDA) based mobile fronthaul.

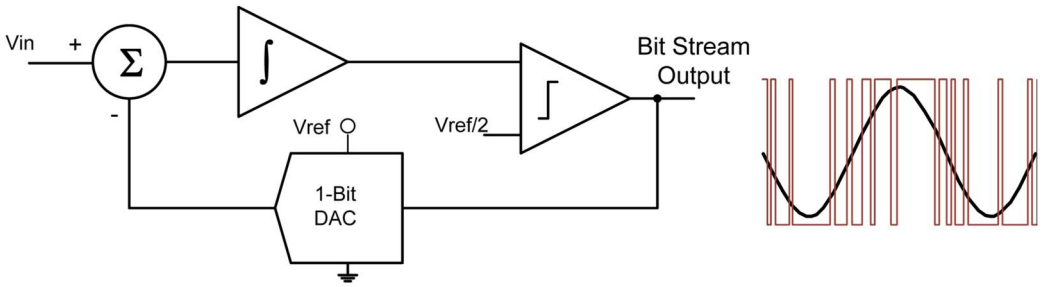

Figure 8. Delta-Sigma Modulator and Its Output

Different from conventional Nyquist ADC which is typically used in CPRI and digital quantization schemes, delta-sigma digitization features high sampling rate, few quantization bits, and more importantly, simple DAC design which can be implemented by passive filters [22], [23], which makes it suitable for mobile fronthaul networks due to the tree architecture and large number of fiber nodes. With a high-speed ADC centralized in BBU-pool and shared by multiple RAUs, and low-cost passive filters distributed in fiber

nodes, the upgrade at fiber nodes can be kept minimum. Figure 8 shows the structure and output waveform pattern of a typical delta-sigma modulator. It is noticed that the delta-sigma modulator is a closed-loop system which maintains the average number of digital ones at the output equal to the input signal's percentage of full scale. However, one issue of delta-sigma modulator based mobile fronthaul lies in that it may require a large sampling rate which is even ten times the bandwidth of the baseband signal. Furthermore, the distribution of the quantization noise is not evenly distributed. The larger the bandwidth, the higher the quantization noise level is which may seriously affect the fairness of the transmitted signal when different component carriers are aggregated in the frequency domain.

There are also other different fronthaul data transmission technologies being discussed in both academic institutes and industries. As mentioned above, analog radio-over-fiber (A-RoF) based MFH attracts interests from researchers because of its high bandwidth efficiency [14]. A-RoF systems don’t require 15-digits quantization and the wireless carriers could be aligned onto different intermediate frequencies (IFs). Therefore, a 1.5-GHz frequency band can reach 59-Gb/s common- public-radio-interface (CPRI) equivalent data rate [16]. Nevertheless, existing A-RoF systems are built upon a point-to-point (PTP) structures and they suffer seriously from nonlinear degradations in electrical amplification as well as ASE from optical amplifications. On the other hand, functional-split based mobile interfaces have incurred a lot of discussions recently [9], [24], [25]. By separating a part of the functions in MAC-layer and physical-layer out of the central unit to the remote sites, data traffic between them could be significantly reduced. Nonetheless, several issues are induced from function split. Firstly, when the split takes place deep

towards the MAC layer, the system becomes thoroughly de-centralized thus incompatible with features like coordinated multi-point (CoMP) transmission and MIMO. When the protocol stacks are split at the physical layer, digitization is still inevitable and the saved bandwidth is limited. Moreover, different applications and radio-access technologies (RATs), such as IoT and enhanced mobile, sometimes need various protocols and have significant differences in modulation formats, FEC, and channel-estimation mechanisms from MAC and physical layers, which incurs high complexity in functional split based systems and weakens its compatibility with 5G heterogeneous network.

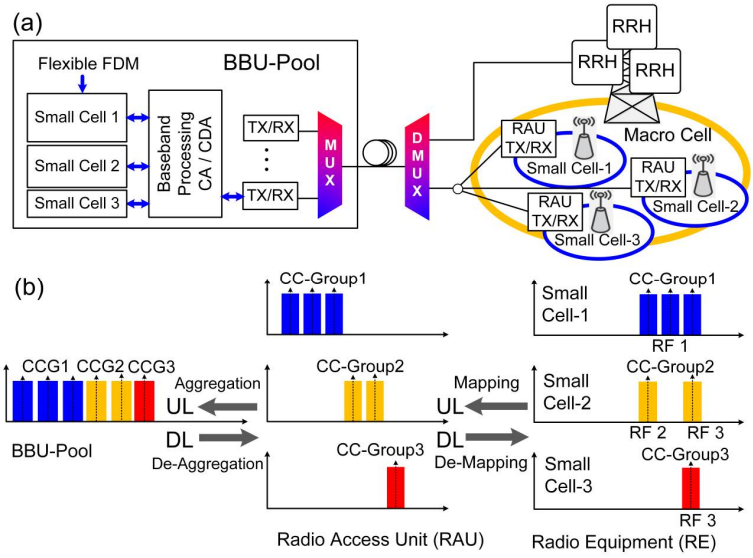

Figure 9. Small-cell compatible point-to-multi-point (PTMP) mobile fronthaul network: (a) architecture; (b) operation principle.

Other than PTP transmission, A-RoF can also be deployed into a small-cell-compatible bidirectional mobile fronthaul systems with CA/CDA. As shown by the architecture shown in Figure 9(a), the system is based on a WDM-FDM PON with a PTMP architecture. Hence, it can connect to increased number of small cells or hot spots, meanwhile still being able to support traditional macro cells which offer a complementary

coverage and assist the coordination functions. As indicated in Figure 9(b), the operation of the mobile fronthaul is composed of two parts. For the down link data transmission, the groups of wireless carriers for different cells are generated at the BBU-Pool. After fiber transmission, component-carrier groups are separated and demodulated inside the corresponding radio access units (RAUs). Then after digital signal recovery and digital frequency up-conversion, CCs are sent to the radio antennas, which transferred the signal onto its corresponding RF bands. Such a design could potentially increase the number of connected cells and the signals for different cells can be efficiently allocated and rearranged with high flexibility.

During the past few decades, various digital-RoF (D-RoF) interfaces are developed, and among them, CPRI and open base station architecture initiative (OBSAI) [27] become matured standards to provide specifications on converting and transferring digitized baseband radio carriers, between radio equipment controller (REC) and radio equipment (RE). Different radio formats are supported including global system for mobile communication (GSM), code division multiple access (CDMA), and evolved universal terrestrial radio access (E-UTRA). By applying sufficient number of quantization digits and appropriate forward error coding (FEC), after signal recovery, the digitized radio carriers can be reconstructed with no quality degradation. Nevertheless, the major disadvantage of D-RoF fronthaul is the low bandwidth efficiency. To digitize each discrete analog sample, 15 digits are needed, which brings heavy burden to the available bandwidth especially for high-speed mobile services.

However, D-RoF technologies still show advantages in the following aspects [28]. Firstly, D-RoF is format agnostic with simple hardware implementation at radio access

units (RAUs) while A-RoF signals may need to be recovered at RAU to eliminate the nonlinear distortions before sent to the antennas. Meanwhile D-RoF data shows high resistance against nonlinear distortions from both electrical and optical components. It can realize high-quality error-free transmission when using FEC, which is critical for uRLLC. These benefits make D-RoF a qualified candidate for future MFH. Recently, a lot of research progresses are made in high-order modulation techniques [29] - [31] and digital compression algorithms [32] - [37] which ignites the hope to largely improve the bandwidth efficiency of D-RoF. Among those algorithms, partial bit sampling (PBS) [32] is simple but the digitization noise grows quickly with fewer number of digits. Researchers from NTT proposed Fitting based nonlinear quantization (FBNQ) [34], [35] with improved precision. However, the execution of the algorithm is time consuming. Furthermore, it is not discussed for these methods on how to improve the compatibility of D-RoF systems with multi-RAT and diverse applications which is important in 5G NR system.

1.4 Time Division Multiplexed Passive Optical Networks for Delay Sensitive Mobile Fronthaul Network

The evolution towards next-generation mobile data network requires the consideration of both network capacity enhancement and transmission latency reduction. According to the in-progress standard framework from ITU-R International Mobile Telecommunications 2020 (IMT 2020) and 3GPP New Radio (3GPP NR) [38], 1-ms latency is required in 5G scenario of ultra-reliable and low-latency communications. Other new emerging technologies, e.g., tactile internet (TI) and virtual reality (VR) also require 1-ms end-to-end latency [39]. To date, more important than increasing the fronthaul throughput, the latency issues also become a major bottleneck limiting future fiber-wireless

access network to achieve ultra-fast response speed. To save the cost for cell expansion and densification in the near future, time-domain multiplexed (TDM) passive optical network (PON) has been proposed as a cost-effective mobile fronthaul (MFH) solution [40], [41] and fibers from existing optical distribution network (ODN) are considered to be an ideal media providing low transmission loss and high network capacity. With long fiber transmission and large-scale computing at the edge servers, the time budget for PON functioning, framing, buffering, and digital signal processing (DSP) has to be greatly reduced to meet the stringent latency requirements. Given processing time slots of 0.5 ms and 0.3 ms at the central stations and user interfaces respectively [39], the bidirectional transmission over the mobile fronthaul should be completed within 0.2 ms in order to guarantee a 1-ms round-trip delay. Moreover, this does not take into considerations the transmission time over 5 to 20-km single mode fiber. However, due to low flexibility and long idle time resulted from traditional request-and-grant bandwidth allocation process in PON, e.g., G-PON and E-PON, it is very challenging to build an optical access network with ultra-fast response time.

Based on the standards defined by ITU-T G987.X, a flex-frame timing-critical PON architecture is proposed in [42] which improves the flexibility and the response speed of the existing G-PON system. The traditional request-and-grant process in bandwidth allocation is modified to report-and-adjust scheme where the data does not need to wait in queue at the optical network unit (ONU) until granted a slot. Thus, highly flexible framing is enabled and short bursts or frames with greatly reduced idle time can be obtained especially under lower traffic load. Meanwhile based on the flex-frame design, an open architecture of the CO is designed, which is compatible with different radio interfaces and

existing G-PON protocol stacks. Different formatted data with various bandwidth allocation schemes can be coexisted, reconfigured, and coordinated without disrupting the normal PON functioning.

Figure 10 shows the conceptual flow diagram of the proposed flex-frame PON, and the bandwidth allocation methods in traditional and proposed schemes. In traditional G-PON, the service data mapping, framing, and functionalities are based on 125-μs GPON-transmission-convergence (GTC) periodicity which guarantees the reliable timing and synchronization of the system. In the DL transmission, timing and synchronization issues are mitigated due to the broadcast nature. However, in the UL transmission, because one common channel is shared among multiple ONUs, a set of complex bidirectional coordination procedures are defined for channel multiplexing and blocking avoidance, which, on the other hand, increases the system processing delay. Furthermore, the non-negligible execution time of dynamic bandwidth allocation (DBA) and the round-trip time (RTT) lead to a period of idle time gap in UL, as shown in Figure 10(b). To avoid potential collision in UL, each ONU needs to wait the grant messages from the OLT before bursting out the data from the buffers. Given a 20-km SMF link, such a process introduces 180-μs round-trip delay. When including the DBA execution time and ONU response time, the total delay is even close to milliseconds, which could be intolerable for future new-radio and fixed services with stringent latency requirements. Class interleaved scheduling is proposed [43], [44] to improve the bandwidth utilization rate, but the limitation from 125-μs fixed framework and idle period still exist in the polling process of each class or thread.

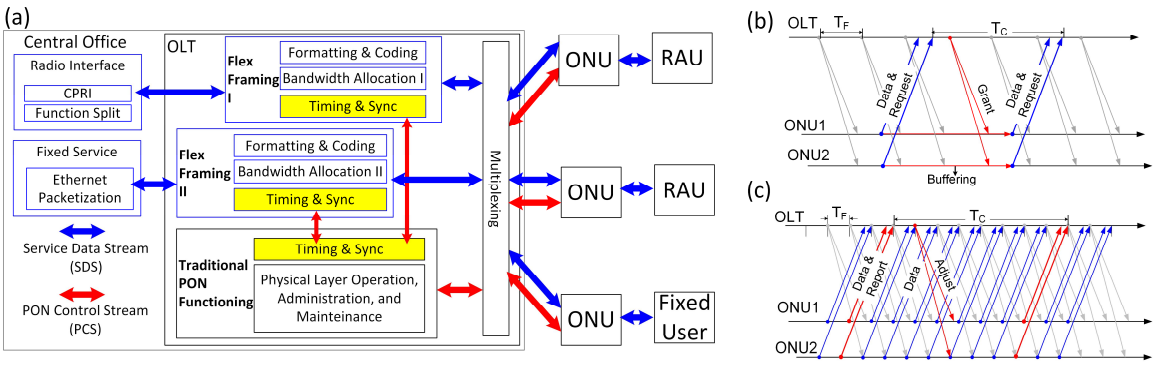

Figure 10. (a): Conceptual flow diagram of flex-frame PON. (b)-(c): Bandwidth allocation schemes in traditional and proposed schemes respectively.

To mitigate the above latency issues, a flex-frame timing critical PON is demonstrated in [42] which is compatible with conventional G-PON and meanwhile achieves fast response speed. The conceptual flow diagram of the proposed PON system and its scheduling process are shown in Figure 10(a) and (c) respectively. In this architecture, part of the functionalities, including bandwidth allocation, service data partitioning, coding and FEC, are separated from the existing PON framework and open to the outer interfaces for modifications and reconfigurations. The data flow encapsulated inside the modified frames defined by the outer interface forms the service data streams (SDS). On the other hand, to guarantee the normal operations for the PON system in terms of timing, ranging, monitoring, protection, and ONU management, PON physical-layer operation, administration, and maintenance (PLOAM) fields are inherited from XGTC specifications and PLOAM messages are transmitted by PON control streams (PCS) which could still follow 125-μs XGTC periodicity. It is worth noting that the framing of SDS can be redefined and adjusted by the outer interface to meet the more critical delay requirements, so SDS does not need to follow 125-μs grid and its frame duration could be much shorter. In the following numerical study, 12.5, 25, 62.5, and 125-μs frame durations are tested. The overhead of the SDS is also greatly reduced because the redundancies

related to PLOAM are simplified and physical synchronization block (PSB) is preserved for the ease of timing alignment.

To cope with the shortened frame duration and maintain a high bandwidth utilization rate, traditional bidirectional request-and-grant (R&G) mechanism in DBA is modified to a report-and-adjust (R&A) algorithm to support both fixed and mobile services. For fixed services, except from considering the already enqueued data of the current frame, based on network traffic self-similarity [45], the statistical information in previous frames are also utilized to predict and adjust the bandwidth needed for the following DBA cycle period. The total request bandwidth reported from ONU i is obtained by $B_i(n+1) = B_{i,Q}(n) + B_{i,P}(n)$, where $B_{i,Q}(n)$ and $B_{i,P}(n)$ are the bandwidth requirements estimated from enqueued data and previous incoming traffic flows respectively. On the other hand, for the wireless data, common public radio interface (CPRI) or split-PHY [46] is assumed to be used as the outer interface which could reconfigure the scheduling scheme based on fixed bandwidth allocation (FBA) or mobile specified DBA [40] respectively. Meanwhile, OLT could globally align and coordinate different framing schemes through PCS to guarantee the functioning of the TDM system. Thus, by separating the functionalities into different blocks and implementing novel bandwidth allocation schemes, the framing for delay-sensitive services is less limited by conventional round-trip coordination process and different services could be compatible over an open PON platform with higher flexibility.

1.5 Multiband Modulation Technologies in Fiber-Wireless Access Networks and Mobile Fronthaul

RoF with millimeter waves are qualified candidates in next-generation fiber-wireless integrated access network to provide multi-band, multi-service, and multi-user access solutions in the near future. To meet these goals, one of the key enabling techniques to boost network capacity as well as scalability is to aggregate a lot of single channels with a large density, advanced modulation formats, and digital filtering techniques. Therefore, multiband modulation become a feasible option enabling the coexistence of different users with different services on different bands. A lot of works are made in this area compiling carrier-less amplitude and phase (CAP) modulation [47], [48], Nyquist wavelength division multiplexing (N-WDM) [49] - [51], super channel operation [52] - [57], and quadrature duobinary precoding [58], [59]. However, supper channel and duobinary precoding may find their shortcomings in high computational complexity which weakens their applications in high-order modulation or high-density carrier aggregation.

However, QAM CAP and N-WDM widely adopt raised-cosine (RC) or square-root raised-cosine (SRRC) filters to shape the pulse of each channel and thus undesired out-of-band power leakages are induced. Furthermore, there are some side effects when applying RC or SRRC filters with regular QAM modulation. First of all, the bandwidth occupied by each channel is larger than Nyquist bandwidth. If the roll-off factor, β, is used to measure the ratio between the excess bandwidth against the Nyquist bandwidth, a loss in the spectral efficiency (SE) will be introduced with a factor of $1/(1+\beta)$. Secondly, in the real deployment in ASIC chips, the pulse shape of a filter needs to be truncated in order to build the discrete filter taps. When the time window span after truncation is increased, the

frequency response of the digital filter tends to its ideal shape and this will be paid by the increase in the number of digital filter taps followed by higher complexity in doing multiplications in digital convolution. Nevertheless, when choosing a small β, for example, $\beta = 0.25$, the insufficient truncation duration will lead to large out-of-band sidelobes [60] which will leak into the adjacent channels reducing the signal-to-interference-plus-noise ratio (SINR). Although, the schemes based on Nyquist supper channel or duobinary precoding can be claimed to exceed Nyquist limit [61]. They require complex DSP, precoding and decoding which significantly increase the complexity and processing latency of the systems. Thus, to control the complexity and at the mean time maintain the high flexibility, multi-band CAP modulation become a promising solution and in the following chapters, it will be demonstrated in detail about the properties of multi-band CAP modulation and its key applications. Moreover, frequency domain multi-band modulation could also be used as the data multiplexing scheme in mobile fronthaul network. Compared with traditional time-division multiplexed methods, multiband multiplexing could bring higher flexibility, lower requirements on synchronization, as well as higher spectral efficiency. Different data streams transmitted to different RAUs could be multiplexed onto different frequency bands and by choosing appropriate digital filters either relaxed synchronization requirements or higher spectral efficiency can be achieved.

1.6 Outline of the Dissertation

The outline and logical relations among different research topics in this dissertation are plotted in Figure 11. Most of the works are focused on mobile fronthaul technology and in our research, they fall into two categories. The first domain belongs to the fronthaul link connecting the central unit (CU) and the distributed unit (DU). In some materials, it is

also named as Tier-II mobile fronthaul [38], which is capable of transmitting data with high capacity through long distance (20 - 80 km). The high-level network architecture is more complex and flexible, emphasizing on software reconfigurability. The promising candidates comprise WDM-PON, coherent optical systems, and multilane transmission links. The second era of mobile fronthaul technology refers to the links between DU and remote radio units, which is often called Tier-I mobile fronthaul. Such links should be able to support point-to-point or one-point-to-a-few-points transmission. Low latency, high flexibility, and compatibility with mobile technologies are the key features of the systems. The desired candidates to realize Tier-I mobile fronthaul include digital radio-over-fiber (RoF), analog RoF, and delta-sigma modulation. Digital RoF features high transmission quality but needs to overcome the issues of lower bandwidth efficiency. In comparison, analog RoF shows higher spectral efficiency but has to pay extra efforts to control the distortions from nonlinearity and chromatic dispersions. The most important work in this dissertation is to study how to improve the bandwidth efficiency of the digital RoF through data compression techniques, where three methods of fast statistical estimation, Lloyd algorithm, and differential pulse code modulation are discussed. On the other hand, to reduce the bi-directional transmission latency, multiband modulation is also proposed to be implemented in both Tier-I and Tier-II mobile fronthaul to replace traditional TDM scheme, with lower synchronization requirements and higher flexibility. Meanwhile, as a minor research topic, there are also some works done in analog RoF systems which mainly consist of digital signal processing and advanced modulation formats to reduce the out-of-band power leakage and improve the spectral efficiency of the signals. It is also worth noting that multiband multiplexing could also benefit analog RoF systems when it is used

to aggregate carriers over different radio-access technologies (RAT) providing multi-service to multiple users. The brief introductions of the chapters are provided as the following.

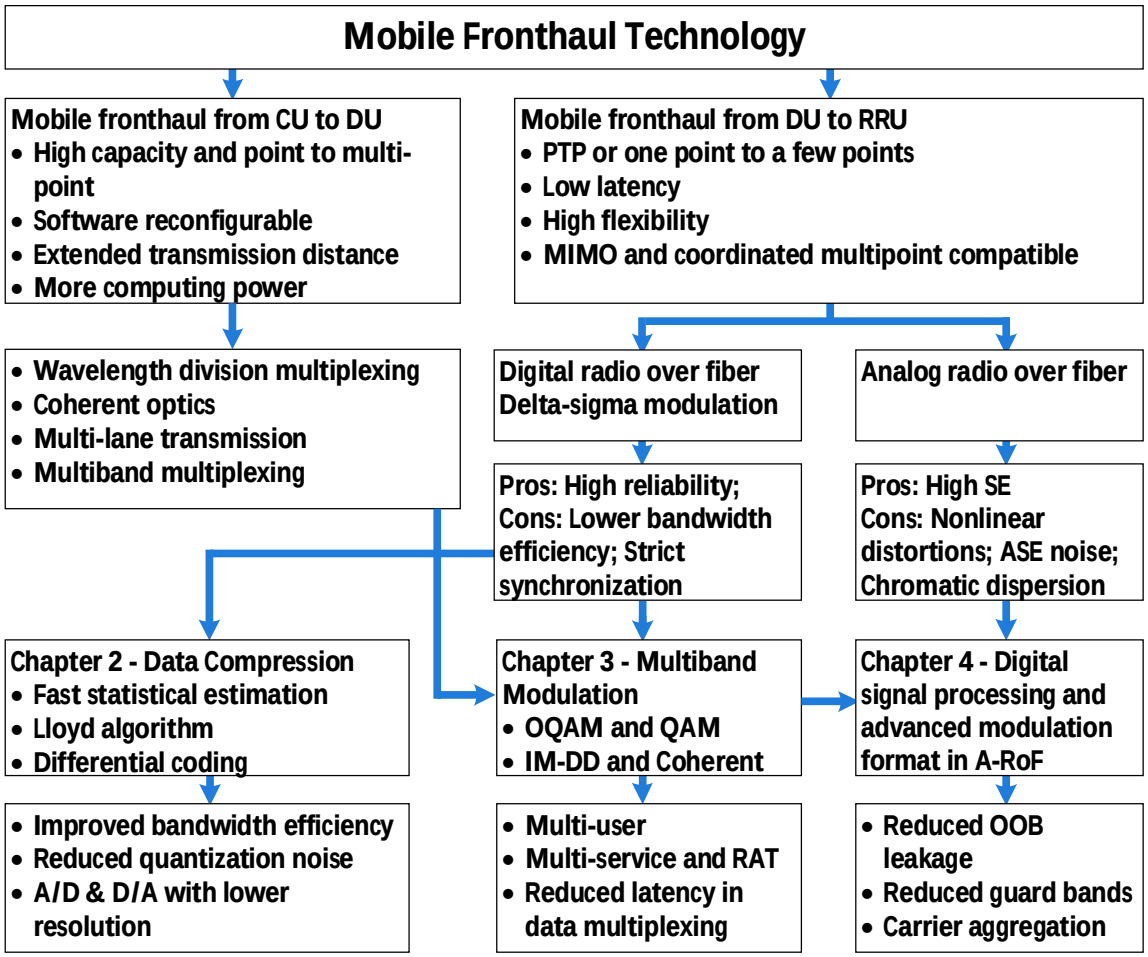

Figure 11. Logical relations of research topics.

After the introduction of research backgrounds and challenges in Chapter 1, Chapter 2 demonstrates two critical technologies to improve the transmission efficiency and flexibility of D-RoF systems. A fast-statistical estimation based data compression algorithm is proposed to reduce the number of quantization digits in a D-RoF based mobile fronthaul with low complexity and high quality. Combined with re-sampling and advanced modulation formats, data-transmission efficiency of a 25-Gbit/s D-RoF testbed is improved

by around 5 times compared with uncompressed CPRI systems. On the other hand, we also experimentally demonstrate a PTMP D-RoF system with multiband modulation, which exhibits higher flexibility and better compatibility with multiple services and different radio-access technologies compared to existing schemes based on time interleaving. An experiment of 13.3-Gbit/s 4-band PTMP bidirectional D-RoF MFH is demonstrated. Combined with data compression, error free delivery of 6.4-Gbit/s 1024-QAM 5G-NR-like signals is realized. Moreover, a data-compression technology with differential-coded Lloyd algorithm is also envisioned to improve bandwidth efficiencies in digital-mobile-fronthaul networks. We experimentally demonstrated milestone transmissions of 180 Gbps over 80-km fronthaul links encapsulating 64×100-MHz 1024-QAM 5G-NR carriers with lower-than-0.5% EVM.

Chapter 3 mainly focuses on discussing the multi-band modulation techniques in mobile fronthaul systems. An offset-QAM carrier-less amplitude and phase modulation (OQAM-CAP) technique for spectral efficient multi-user RoF systems is demonstrated. In comparison with traditional QAM based CAP modulation schemes, the digital filter for each channel in OQAM-CAP can be adaptively redesigned to obtain either higher spectral efficiency or lower computational complexity. Two kinds of digital filters, namely, square-root raised-cosine (SRRC) filters and isotropic orthogonal transform algorithm (IOTA) based filters, are studied and applied to shape the frequency window of each channel in CAP systems. We compared the performances among SRRC-OQAM CAP, IOTA-OQAM CAP, and traditional SRRC-QAM CAP. It is experimentally demonstrated that SRRC-OQAM-CAP can achieve higher spectral efficiency, IOTA-OQAM-CAP can obtain higher

computational efficiency, and SRRC-QAM-CAP can be used in uplink transmission with lower inter-channel interference.

Chapter 4 reviews some related works in analog RoF systems. The basic operation principles in a bidirectional point-to-multi-point mobile fronthaul system are discussed and different detection techniques for receiving UL signals have been compared. Wavelength division multiplexing plus frequency division multiplexing (WDM-FDM) is implemented to support remotely distributed asynchronous small cells. Intensity-modulation plus direct-detection (IM-DD) as well as filed-modulation plus heterodyne-detection (FM-HD) are used for downlink and uplink respectively. Combined with efficient virtual tone based phase recovery DSP and carrier-frequency-offset estimation, penalties and interference from undesired beating components in UL signals are mitigated. Proof-of-concept experiments are performed and 18 - 20 80-MHz component carriers (CCs) are aggregated and transmitted over 25-km standard single mode fiber (SSMF) bidirectionally. The last part of Chapter 4 investigates using filter-bank multi-carrier (FBMC) in a mobile fronthaul to reduce the guard bands between adjacent channels.

The summary of the contributions in my PhD work is rendered in Chapter 5 and future research directions are envisioned in the end.

CHAPTER 2. STATISTICAL DATA COMPRESSION IN NEXT-GENERATION DIGITAL ROF MOBILE FRONTHAUL

As a counterpart of analog radio-over-fiber (A-RoF) technology, digital radio-over-fiber (D-RoF) system, such as common public radio interface (CPRI), is a matured and robust solution to support RF signal delivery in traditional mobile fronthaul networks. In view of recent progresses in delta-sigma modulation, data compression, and advanced error correcting coding, the efficiency of D-RoF is significantly improved, which motivates researchers to re-evaluate the role of D-RoF in future mobile fronthaul networks to support 5G and beyond wireless communications. In this paper, we demonstrate two critical technologies to improve the transmission efficiency and flexibility of D-RoF systems. A fast-statistical estimation based data compression algorithm is proposed to reduce the number of quantization digits in a D-RoF based mobile fronthaul with low complexity and high quality. Combined with re-sampling and advanced modulation formats, data-transmission efficiency of a 25-Gbit/s D-RoF testbed is improved by around 5 times compared with uncompressed systems. On the other hand, we also experimentally demonstrate a point-to-multi-point (PTMP) D-RoF system with multiband modulation, which exhibits higher flexibility and better compatibility with multiple services and different radio-access technologies compared to existing schemes based on time interleaving. An experiment of 13.3-Gbit/s 4-band PTMP bidirectional D-RoF MFH is demonstrated. Combined with data compression, error free delivery of 6.4-Gbit/s 1024-QAM 5G-New-Radio-like signals is realized.

2.1 Introduction of Digital RoF Systems

Future 5G mobile data network, with its standardization getting ready, incurs a great challenge for building the mobile fronthaul (MFH) network in aspects of capacity, latency, and cost. To address these issues, different fronthaul technologies are being discussed in both academic institutes and industries. Among them, analog radio-over-fiber (A-RoF) based MFH attracts interests from researchers because of its high bandwidth efficiency [62]. A-RoF does not require 15-digit quantization and the component carriers (CCs) can be densely modulated onto different intermediate frequencies (IFs). Thus 1.5-GHz bandwidth can support 59-Gb/s common- public-radio-interface (CPRI) equivalent data rate [16]. However current A-RoF schemes are based on a point-to-point (PTP) structure and they suffer seriously from nonlinear degradations in power amplifiers as well as power fading from chromatic dispersions. On the other hand, functional-split (FS) based mobile fronthaul has triggered intensive discussions recently [9], [26]. By separating a part of the MAC-layer and physical-layer functions from the central site to the remote sites, data traffic over MFH can be greatly reduced. However, several issues are resulted from FS. Firstly, when the split happens deep towards the MAC layer, the system becomes incompatible with features like MIMO and coordinated multi-point (CoMP) transmission. When the protocol stacks are split at the physical layer, digitization is still needed. Moreover, different environments and radio-access technologies (RATs), such as IoT and enhanced mobile broadband, may require different protocols and have different data formats in MAC and physical layers, which increases the complexity of FS based systems and reduces its compatibility with 5G heterogeneous network.

During the past few decades, digital-RoF (D-RoF) interfaces, like CPRI [13] and open base station architecture initiative (OBSAI) [27], have become matured techniques to deliver digitized baseband radio carriers from radio equipment controller (REC) to radio equipment (RE) in different standards, including global system for mobile communication (GSM), code division multiple access (CDMA), and evolved universal terrestrial radio access (E-UTRA). With sufficient number of quantization digits and forward error coding (FEC), the digitized radio carriers can be reconstructed by a digital to analog converter (DAC) with no quality degradation. However, one drawback of traditional D-RoF is its low transmission efficiency (TE). To transmit each sample, it requires more than 15 digits, which will quickly deplete the available bandwidth resource when transporting high speed wireless signals. Here, TE is defined as the ratio between the effective bandwidths of the encapsulated wireless signals and the D-RoF system.

Nevertheless, D-RoF still shows several remarkable benefits [28]. It is format agnostic with simple hardware implementation at radio access units (RAUs). Meanwhile it benefits from digitization with high immunity to nonlinear distortions from power amplification. Error free transmission can be obtained when using FEC. These features imply that D-RoF has the potential to be applied in future MFH. Recent progress in advanced modulation formats [29] - [31] and data compression techniques [32] – [37] for transmitting orthogonal-frequency- division-multiplexed (OFDM) signals ignites the hope for greatly improving the TE of D-RoF systems. Among these compression techniques, partial bit sampling (PBS) [32] is easy to be implemented but the quantization noise grows fast when reducing the number of digits. Fitting based nonlinear quantization (FBNQ) is also proposed in [34], [35] and recommended by the standard of Open Radio Equipment

Interface (ORI) [36] with improved accuracy. However, the algorithm is complex and time consuming because it needs to estimate the statistical characteristics from a large number of samples which increases the system delay. Moreover, all these methods didn't study how to efficiently multiplex digitized samples in uplink (UL) and how to improve the multi-RAT compatibility of a D-RoF MFH, which are critical to support 5G New-Radio (NR) systems with distributed small cells.

In this research, to the first time, we propose a fast-statistical- estimation (FSE) algorithm for data compression in 25-Gbit/s D-RoF systems. Compared with existing schemes, the computational-complex fitting process is simplified which improves the processing speed and reduces the latency. High compression radio (15 to 8 bit) can be obtained with suppressed quantization noise. For 64-QAM LTE signals recovered after decompression, 0.56% error-vector magnitudes (EVM) and 23-dB system margin from the 64-QAM EVM threshold are achieved. Combined with 3/4 re-sampling and PAM-4 modulation, TE can even approach that of PHY-I-Split interface [9]. Meanwhile, a multiband D-RoF MFH interface is also proposed to improve the latency, flexibility, and multi-RAT compatibility of the system especially for its UL. By allocating frequency-domain bandwidths for distributed remote sides, the delay and complexity induced by traditional time-division multiplexed or time-domain interleaving based systems are reduced. Bidirectional transmission experiment is demonstrated with 4-band D-RoF channels, which is able to deliver 6.4-Gbit/s 1024-QAM 5G-NR-like CCs with less than 0.6% EVM.

The organization of the chapter is as follows: Section I presents the operation principles of data compression and compares our proposed FSE algorithm with other

existing methods. Experimental results of FSE in a 25-Gbit/s MFH is also demonstrated. Section II presents the concept of multiband D-RoF system and discusses its benefits as well as related experimental results. Section III concludes the paper.

2.2 D-RoF MFH Interface with FSE Based Data Compression

2.2.1 Operation Principles of Data Compression in D-RoF Systems

The operation principles of data compression in digitized OFDM signals are shown in Figure 12. Typically, the probability density function (PDF) for the amplitude of an OFDM signal follows Gaussian distribution characterized by expectation μ and standard deviation σ, as shown in Figure 12(a). In FBNQ method, statistical fitting is performed where the system estimates μ and σ of a given OFDM baseband signal by calculating the mean $\hat{\mu}$ and the standard variance $\hat{\sigma}$ from a large number of samples. Then the amplitudes of the real and imaginary parts of the samples are companded based on the estimated cumulative distribution function (CDF). The CDFs of the modulus for a baseband-OFDM-signal real part before and after companding are compared in Figure 12(c) and (d) respectively. It is observed that, before companding, the slope of the CDF is non-uniformly distributed. The probability increases fast when the modulus is small and the increasing rate becomes retarded when modulus gets large. If we apply uniformly distributed quantization levels to digitize the modulus, significantly large quantization errors will be resulted from the region where CDF shows a large slope. However, after linearizing the CDF through companding as shown in Figure 12(d), the error after uniform quantization can be minimized. Typically, the compression algorithm starts with companding a U-bit digitized OFDM signal based on its statistical distribution and then apply V digits (U > V)

to re-digitize the signal and meanwhile to control the quantization error below the tolerable threshold. In this case, the number of bits after compression can be reduced by a factor of $(U–V)/U$.

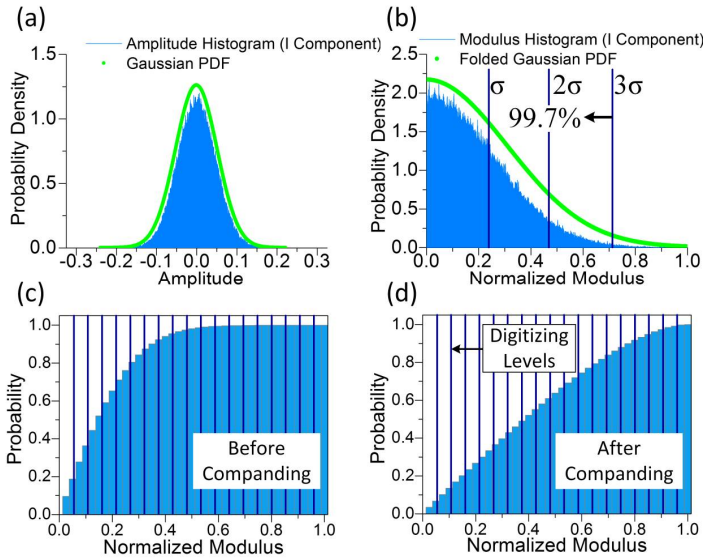

Figure 12. Probability distribution functions of (a) amplitude and (b) modulus for an LTE-like OFDM signal; (c) and (d): cumulative distribution functions of OFDM signal's modulus before and after companding respectively.

The algorithm of FBNQ is shown in Figure 13(a). The analog baseband OFDM in-phase (I) and quadrature (Q) components are digitized by a U-bit analog-to-digital converter. The statistical fitting is applied to estimate the Gaussian distribution function. Then based on the fitted Gaussian distribution and companding algorithm, original sample amplitudes with U bits are nonlinearly mapped to the compressed ones with V bits at the transmitter. Similarly, a reversed V-to-U bit mapping is applied at the receiver site to decompress those samples.

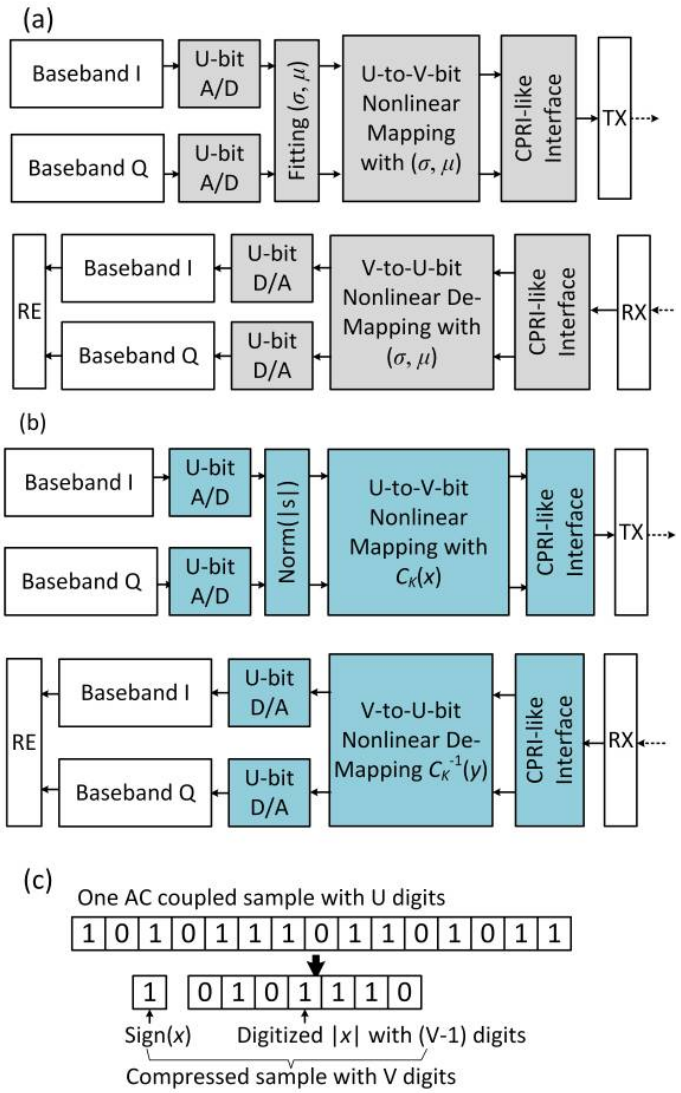

Figure 13. (a) and (b): DSP flow of FBNQ and FSE based data-compression methods respectively. (c): Digitized data formats before and after compression.

However, one drawback of existing FBNQ method is that, in order to estimate σ, the statistical fitting process needs to calculate the deviation of each sample's amplitude from the mean value, which is computational complex and time consuming. In this paper, we propose an FSE based scheme as shown in Figure 13(b). For AC-coupled CCs with no DC component, the modulus of the signal is considered instead of its amplitude. The modulus PDF of an OFDM signal is shown in Figure 12(b), which follows folded Gaussian

distribution. Compared with Gaussian distribution shown in Figure 12(a), signal modulus is always positive with an accurate zero level. After combining this property with FSE algorithm proposed in the following part, computational efficiency can be improved, which does not need to calculate the average value and deviations of the bipolar amplitudes in FBNQ. FSE algorithm supposes that the amplitude of the signals, s, is bounded by $[-K\sigma\ K\sigma]$ and the corresponding PDF and CDF of signal modulus, $x = |s|$, are modified to

$$f(x) = \frac{2}{\sqrt{2\pi}\sigma\Delta} e^{-\frac{x^2}{2\sigma^2}} \tag{2.1}$$

$$F_X(x) = \frac{1}{\Delta}\mathrm{erf}\left(\frac{x}{\sqrt{2}\sigma}\right) \tag{2.2}$$

where $\Delta = 1 - 2\Phi(-K)$ and Φ is the CDF of the standard Gaussian distribution. Such a distribution is also named as truncated folded Gaussian (TFG) distribution. The acquisition of the companding transform function, $y = C(x)$, is based on [63]. Here y is the output linearized signal modulus which obeys uniform distribution given by

$$F_Y(y) = \frac{y}{K\sigma}\ , \quad y \in [0 \quad K\sigma]. \tag{2.3}$$

Since $F_X(x)$ and $F_Y(y)$ are continuous and strictly monotone increasing functions, the following relation can be derived as

$$\begin{aligned} F_X(x) &= \mathrm{Prob}(X \le x) \\ &= \mathrm{Prob}\big(C(X) \le C(x)\big) \\ &= F_Y\big(C(x)\big) \end{aligned}. \tag{2.4}$$

Hence $C(x)$ can be immediately deduct as

$$C(x) = F_Y^{-1}\left[F_X(x)\right] \tag{2.5}$$

By substituting (2.3) and (2.4) into (2.5), one can obtain

$$C(x) = \frac{K\sigma}{\Delta}\operatorname{erf}\left(\frac{x}{\sqrt{2}\sigma}\right) . \tag{2.6}$$

Accordingly, the de-companding transform function is simply derived by taking the inverse function of (6): $C^{-1}(y)$.

One important property of zero-mean Gaussian distribution is that 99.7% of the samples fall into the range of $[-3\sigma\ 3\sigma]$, which is also known as three-sigma rule. Therefore, it can be predicted that when K approaches 3, given enough number of samples, the approximated TFG distribution could highly approach the original un-truncated folded Gaussian distribution since it considers more than 99% of the possible modulus values. It is worth noting that, because the modulus *x* is assumed to be distributed on $[0\ +K\sigma]$, after normalization, obviously, the following relations can be educed, $x_{\max\_norm} = K\sigma = 1$. Consequently, the standard variance can be immediately obtained by $\sigma = 1/K$. Compared with FBNQ method, no fitting is needed to achieve the statistical characteristics of TFG, which could significantly reduce the computational complexity and processing delay. Based on (6), the flow diagram of FSE data compression in a D-RoF system is shown in Figure 13(b), which is similar to the stacks of FBNQ shown in Figure 13(a). However, the fitting process is eliminated and the core algorithm of the system is replaced by our proposed TFG-FSE method where the compression and decompression mappers are

generated based on $y = C(x)$ and $x = C^{-1}(y)$ respectively. The following experimental results demonstrate that, except from reduced complexity, TFG-FSE is also a highly accurate method. By repeatedly testing over waveforms with more than 10,000 samples, the best K value with the smallest quantization error is found to be around 2.7. Figure 13(c) demonstrates the digitized data format before and after compression. It is noticed that the first digit of the compressed sample is the sign of the amplitude ("+" or "-"). Actually, only (V-1) digits are taken into use to realize the U-to-V-bit mapper.

Similarly, the proposed mathematical approach can also be applied to compand the power of the sample, $x = |s|^2$, $s \in [-K\sigma \;\; K\sigma]$. The number of quantization levels can also be reduced afterwards. Under this case, x follows truncated powered Gaussian (TPG) distribution. Likewise, the companding transform function can be educed as

$$C(x) = \sqrt{\left[\frac{K^2\sigma^2}{1-2\Phi(-K)}\right]\operatorname{erf}\left(\frac{\sqrt{x}}{\sqrt{2}\sigma}\right)}. \tag{2.7}$$

Except from statistical based companding methods, some matured companding methods for encoding acoustic signals are also considered here. They include μ-law and A-law [64]. The companding transform function of μ-law can be derived as

$$C(x) = \operatorname{sgn}(x)\frac{\ln(1+\mu|x|)}{\ln(1+\mu)}, \quad x \in [-1,+1] \; . \tag{2.8}$$

On the other hand, the companding transform of A-law is realized by a piecewise function, which is expressed as

$$C(x)=\begin{cases}\operatorname{sgn}(x)\dfrac{A|x|}{1+\ln A}, & 0\le|x|\le\dfrac{1}{A}\\ \operatorname{sgn}(x)\dfrac{1+\ln\left(A|x|\right)}{1+\ln A}, & \dfrac{1}{A}\le|x|\le 1\end{cases}. \tag{2.9}$$

2.2.2 Experimental Verifications and Discussions for D-RoF MFH with Data Compression

To compare the performance of the aforementioned data compression methods, we set up a simple back-to-back intensity-modulation and direct-detection (IM-DD) link with a 10-GHz directly modulated laser (DML) and a 10-GHz avalanche photodetector (APD) used as the transmitter and receiver respectively. The electrical signal is generated by a 10-GSa/s DAC and sampled by a 20-GSa/s digital oscilloscope. One digitized 30.72-MHz LTE OFDM CC carrying QPSK, 16QAM, and 64QAM signals are firstly companded and mapped to 8-digit binary signals. Signal components are reconstructed offline after 8-to-15-bit de-mapping. The results of the EVM for decompressed signals after applying different algorithms are compared in Figure 14(a) to (d). Since there are nonreversible information losses when we forcibly reduce the quantization resolution, the quality of the signals will be degraded after data compression by so called quantization noise. One key objective to study companding algorithm is to minimize the resulted quantization noise. For comparison, blue lines with an EVM value of 0.94% are marked in Figure 14(a) to (d), which are obtained from PBS method with low-order digits directly removed at the transmitter and replaced with random digits at the receiver [32]. It can be observed that, by optimizing the parameter of the algorithm, EVM can be improved. Among these methods,

TFG-FSE obtains the highest improvement when K is ranged from 2.5 to 3.2 with the lowest EVM value of 0.56% at K≈2.76.

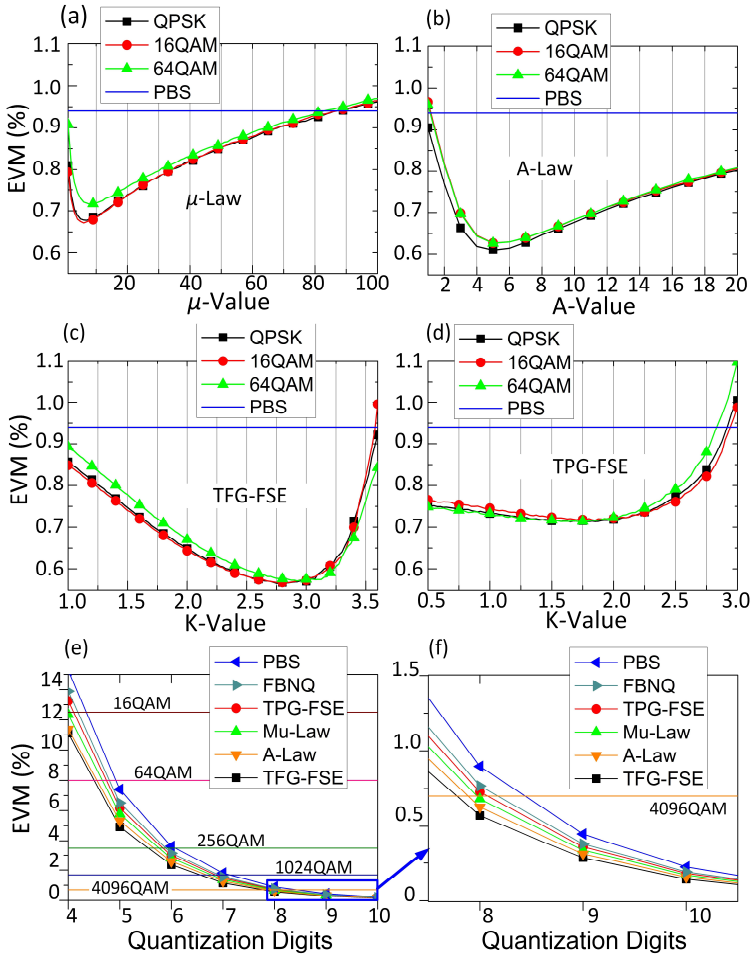

Figure 14. (a) to (d): EVM performance versus key parameters in μ-Law, A-Law, TFG-FSE, and TPF-FSE methods respectively. (e): EVM versus number of quantization digits for different companding methods. (f): Enlarged diagram of (e) when number of digits is varied from 8 to 10.

Figure 14(e) and (f) compare the EVM performance as a function of the number of quantization digits. It is observed that, for all the cases, EVM is degraded with fewer number of quantization levels, which is induced by larger quantization noise. The EVM thresholds of 16-, 64-, and 256-QAM modulated OFDM signals before air transmission are 12.5%, 8%, and 3.5%, respectively, which are quoted from 3GPP release 12 [24].

Meanwhile, the thresholds of 1024- and 4096-QAM are also marked in Figure 14(e) and (f) with EVM values of 1.68% and 0.7%, respectively, which are defined in DOCSIS 3.1 [65]. From these results, it is worth mentioning that, actually 5 digits are enough to sample a 64-QAM OFDM signal with EVM passing the 8% threshold. However, in a real system, because of the variance in amplitude of the received signals, around 20-dB margin should be left for dynamic-range tolerance. That is why in [32] and [36], 10 digits after compression are recommended for RF signal delivery. However, it is observed that, with advanced companding algorithm, the quantization error can be further suppressed with a better signal quality after decompression. Namely, as shown in Figure 14(f), by utilizing TFG-FSE, A-law, or μ-law, EVM values could pass the 4096-QAM threshold with 28 quantization levels. For comparison, when U=15 and V=8, EVM values achieved by TFG-FSE, A-law, μ-law, FBNQ and PBS methods are 0.56%, 0.63%, 0.68%, 0.767%, and 0.897% with 23.098-, 22.075-, 21.4-, 20.4-, and 19.0-dB system margins from 8% 64-QAM threshold respectively. Table I summarizes the net bits of original symbols, minimum required number of bits after compression, and the number of bits in CPRI standard. It is found that when lower-order modulation formats are applied, e.g., QPSK or 16-QAM, higher compression ratio can be potentially achieved compared with CPRI. On the other hand, with higher-order modulation formats such as 256-QAM or 1024-QAM, after compression, the number of digits of each sample approaches the number of corresponding net bits. This fact indicates that, with advanced compression method, the D-RoF based MFH could realize high TE approaching that of PHY-I-Split scheme [9] where the OFDM modulation functions are moved to the RAU site and the MFH directly transmits the net bits of each symbol before the inverse fast Fourier transform (IFFT).

Combining with simple hardware implementations at the distributed RAUs, compressed D-RoF could still be a competitive option against FS in certain application scenarios.

Table 3 – Minimum number of bits for different modulation formats.

Formats	QPSK	16-QAM	64-QAM	256-QAM	1024-QAM
Net Bits	2	4	6	8	10
Minimum Bits after Compression	8 (2×4)	8 (2×4)	10 (2×5)	12 (2×6)	14 (2×7)
Bits in CPRI	30 (2×15)	30	30	30	30

2.2.3 Experimental Demonstrations of 25-Gbit/s Compressed D-RoF MFH with Re-Sampling and PAM-4

Despite using data compression technique, itself, it can also be combined with re-sampling and advanced modulation formats to further improve the TE of D-RoF MFH. To demonstrate the feasibility and performance of TFG-FSE data compression scheme jointly working with other techniques, a D-RoF MFH test bed is set up with the system diagram shown in Figure 15. At the BBU-Pool the OFDM modulated LTE-like baseband components (BCs) are generated with a sampling clock of 30.72-MHz and bandwidth of 20-MHz. Then each BC is down-sampled by a rate of 3/4 before quantization with 15 digits. Therefore, the sampling clock is reduced from 30.72 MHz to 23.04 MHz. Afterwards TFG-FSE based data companding process depicted in Figure 13(b) is applied to map each 15-digit sample into 8 digits and 1-digit control word is added to every digitized sample to compose one antenna carrier (AxC) chip. AxC chips from 54 different BCs are interleaved and multiplexed in time domain to form CPRI-like frames. To

guarantee the error-free performance, the data is encoded with CPRI-like Reed-Solomon forward error correction coding (RS-FEC 528/514) [13]. Subsequently, the binary data is mapped to PAM-4 symbols. A square-root raised cosine (SRRC) filter with a roll-off factor of 0.2 is applied to shape the pulses of the PAM-4 symbols. A Keysight M8195A arbitrary waveform generator is used to generate the PAM-4 modulated waveforms and the signal is modulated onto the light by a 10-GHz DML operated at 1310 nm. After 20-km standard-single-mode-fiber (SSMF) transmission, at the RAU site, a 10-GHz APD is used to convert the signal from the light into electrical domain before sampled by a digital oscilloscope. Then processes of zero-forcing equalization, FEC decoding, decompression, and 4/3 up-sampling are performed offline successively to recover the OFDM signals. The PAM-4 MFH test bed is operated with a data rate of 25 Gbit/s which encapsulates 54 20-MHz LTE signals with I and Q components. The TE of the MFH is defined as the number of LTE symbols transmitted between the BBU-Pool and RAU during each unit time slot. By estimation, 3/4 re-sampling, 15-bit-to-8-bit data compression, and PAM-4 modulation can improve the TE by factors of 4/3, 16/9, and 2, respectively. Hence the TE can be improved by 4.74 in total compared to that of existing CPRI.

The measured (bit-error-rate) BER results and the Matlab-plotted received eye diagrams of the PAM-4 signals are shown in Figure 16(a). After FEC decoding, error free performance can be obtained when the BER passes the threshold of ~5E-4 with a received power around -16 dBm. Under error-free condition, the quantization error induced by TFG-FSE based compression and decompression method is insignificant. Figure 16(b) shows the recovered constellations of 64-QAM and 256-QAM wireless signals with EVM values

of 0.57% and 0.56% respectively, which demonstrates the feasibility of the compressed D-RoF MFH solution.

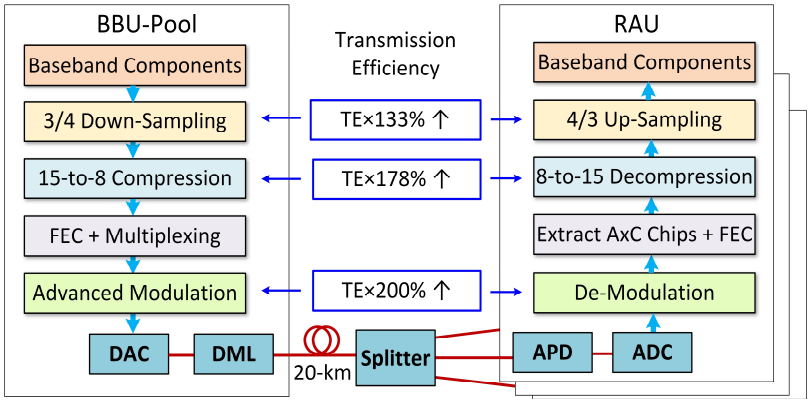

Figure 15. Experimental set-up and function stacks of 25-Gbit/s IM-DD D-RoF based MFH.

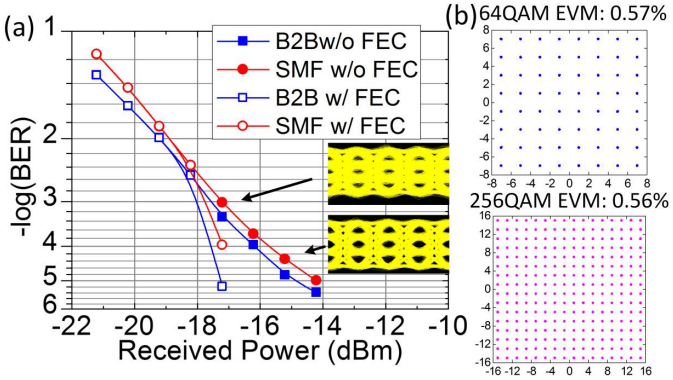

Figure 16. (a): BER performance as a function of received optical power. (b): Selected constellations of LTE-like OFDM signals after 15-to-8-bit compression and decompression.

2.3 D-RoF MFH Interface with FSE Based Data Compression

2.3.1 Operation Principles of Frequency-Domain Multiband Multiplexing versus Time-Domain Interleaving

In existing D-RoF based MFH, like CPRI, to reduce the latency and avoid using complex dynamic bandwidth allocation (DBA) algorithm in traditional TDM systems,

time-domain interleaving is used for multiplexing the digitized signals to different radio transmitters [66]. As shown in Figure 17(a), to construct a CPRI basic frame, digitized samples are interleaved and arranged in order per AxC chip, e.g., AxC Chip 1 first, AxC Chip 4 last. Such time-domain interleaving is straightforward but it suffers from some drawbacks which may not keep up with the requirements of future 5G mobile data networks. The first issue is that in order to realize the interleaving operation, the sampling clock of every CC should be equal to or integer multiple of one unit clock reference. Although such a condition is met for current LTE system, it limits the system flexibility and weakens the compatibility with multi-RAT coexistence in a 5G heterogeneous network. On the other hand, after re-sampling operation, maintaining the same 30.72-MHz clock reference becomes difficult, e.g. with 3/4 down-sampling for 20-MHz CC and 4/5 down-sampling for 15-MHz CC, which complicates the interleaving algorithm. Moreover, time interleaving requires strict synchronization among all the AxC chips, which becomes a great challenge for developing a multi-point-to-point (MPTP) network for UL transmission supporting distributed multiple RAUs.

In this paper, to resolve the aforementioned issues, we propose to introduce frequency-domain multiband multiplexing in a D-RoF MFH network with its flow diagram shown in Figure 17(b). The inputs of the system are the baseband groups (BBGs) from different cells. Each BBG is composed of one or multiple interleaved baseband components of the wireless signals. After applying digitization and compression following the process shown in Figure 13(b), the BBGs are converted into digitized component carriers (DCCs). Then frequency-domain multiband multiplexing is introduced to multiplex different DCCs into different frequency bands. Modulation formats like carrierless amplitude and phase

modulation (CAP) [67], [68] and multiband discrete-Fourier-transform-spread OFDM (DFTS-OFDM) [69] can be used here. Both methods have comparable spectral efficiency and lower peak-to-average power ratio (PAPR) than OFDM. The bandwidth and modulation formats of each DCC can also be flexibly adjusted in CAP without limitation of using the same clock reference. With highly efficient FFT algorithm, DFTS-OFDM has better computational efficiency and flexibility but more sensitive to timing as well as frequency offset than CAP. With digital filtering, the adjacent channels in CAP modulation can be isolated with slightly increased computational complexity. The guard band can be reduced in CAP modulation for PTMP UL transmission and it does not require strict synchronization. In the following part, we apply CAP to experimentally demonstrate the operation of multiband D-RoF MFH network.

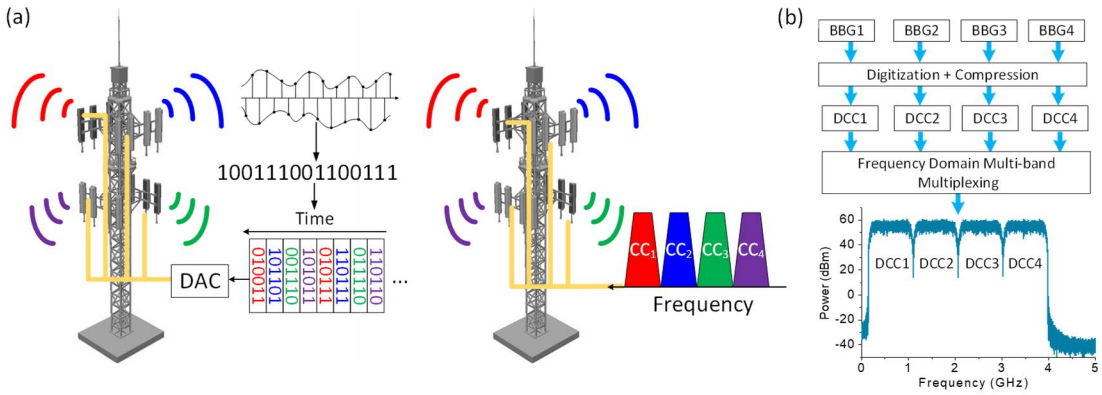

Figure 17. (a): Operation principles of data multiplexing in traditional MFH. (b): Flow diagram of proposed data multiplexing in MFH incorporating frequency-domain multiband modulation.

2.3.2 Experimental Demonstration and Results of Bidirectional Multiband D-RoF MFH

The system diagram of the bidirectional D-RoF MFH with multiband modulation is shown in Figure 18(a). In the experiment, for both DL and UL transmission, four 16-QAM modulated DCCs are multiplexed in frequency domain and each DCC is filtered by a digital SRRC filter with a roll-off factor of 0.15. The channel separation and baud rate of the DCCs are 958.3 MHz and 833.3 MHz respectively. Thus, considering 15-to-8-bit data compression and 3/4 down sampling, the data rate of each DCC with 3.33 Gbit/s is enough to encapsulate one 5G-NR-like CC at the sampling rate of 245.76 MHz (8×30.72 MHz) with I and Q components. Therefore, four D-RoF bands with a total data rate of 13.3 Gbit/s could carry compressed high-quality 5G-NR-like data at a speed up to 6.4 Gbit/s under 1024-QAM modulation.

The proof-of-concept D-RoF MFH is composed of one BBU-Pool and two RAUs as shown in Figure 18(a). The odd and even DCCs are allocated for RAU1 and RAU2 respectively with their offline-generated electrical spectra shown in Figure 18(b) and (c) respectively. The DL of the system is based on an IM-DD architecture. Light from a distributed feedback (DFB) laser operated at 1551.3 nm is boosted by an erbium doped fiber amplifier (EDFA) to reach the power of 13 dBm. A Mach-Zehnder Modulator (MZM) biased at $V\pi/2$ is used to modulate the four-band D-RoF signals onto the light. After 15-km-SSMF transmission, the optical signals are received by photo detectors (PDs) at RAU sites with the electrical spectrum shown in Figure 18(d). The wireless signals from odd and even bands are recovered offline in RAU1 and RAU2 respectively.

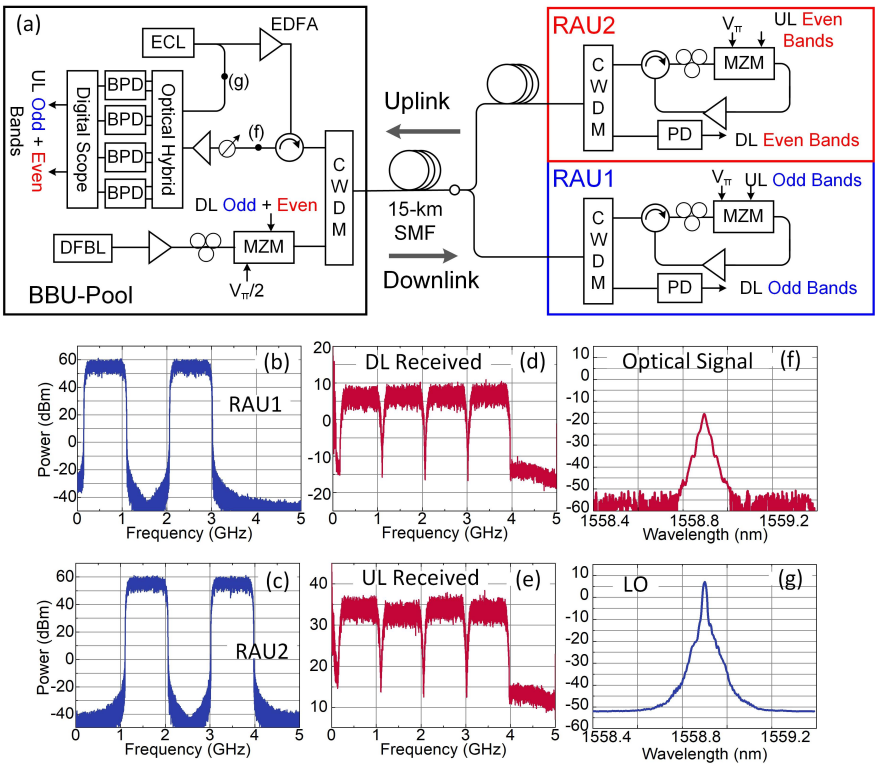

Figure 18. (a): Experimental system diagram of the bidirectional D-RoF MFH with multiband modulation; (b) and (c): electrical spectra of signals sent from RAU1 and RAU2 respectively; (d) and (e): received electrical spectra for DL and UL transmissions respectively; (f) and (g) optical spectra of signal and LO lights as marked in (a) respectively.

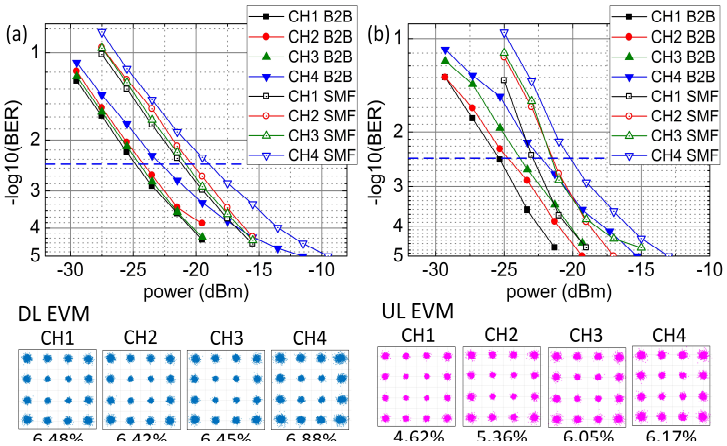

Figure 19. EVM performance versus received optical power for different channel under (a) DL and (b) UL transmissions. Insets show the selected pre-equalized CAP-16 constellations with no bit errors.

On the other hand, because of the impairments induced by combining incoherent optical signals [22], [70], the PTMP UL transmission scheme is more complicated than DL transmission. Either cost-effective coarse wavelength-division multiplexing (CWDM) based band mapping [71] or optical-spectral-efficient coherent detection scheme [21] can be used. It is worth mentioning that the advantages of different UL methods are not the key point to be discussed in this manuscript. Coherent detection scheme is used in the UL experimental demonstration here just to verify the concept as well as feasibility of a multiband D-RoF system. When using the same wavelength, since the phase and polarization of the frequency-division multiplexed signals from two independent RAUs are not correlated, after combination and photo-detection, there are intensity fluctuations due to phase-noise beating terms and polarization mismatch. Thus, coherent detections are needed and phase variance on the optical signal I and Q components are tracked. To eliminate the carrier-frequency offset (CFO) among the signal lights and the optical local oscillator (LO), one ECL is split to be used as the LO as well as the light sources for two RAUs. At each RAU, an MZM biased at $V\pi$ is used to modulate the corresponding signals onto the electrical field of the light and a polarization controller (PC) is inserted before the MZM to adjust the polarization state of the light to maximize the modulation depth. Then the signal lights from two RAUs are combined and transmitted back to the BBU-Pool. The signal and LO are combined through a 90-degree optical hybrid and sent to the optical coherent detector with their optical spectra shown in Figure 18(f) and (g) respectively. Coherent signal recovery algorithms are applied and the combined signals are demodulated and decompressed offline with the electrical spectrum shown in Figure 18(e).

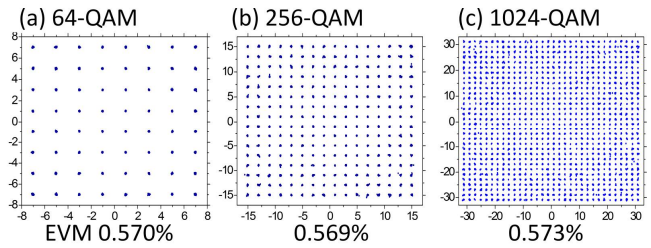

Figure 20. Selected constellations of extracted de-compressed 5G-NR-like wireless signals with (a) 64-QAM, (b) 256-QAM, and (c) 1024-QAM.

The experimental results of BER as a function of received optical signal power for both DL and UL are shown in Figure 19(a) and (b) respectively. For all the cases, the BER curves can pass the 7%-hard-decision-FEC threshold of 3.8E-3. In DL transmission, the receiver sensitivities at the FEC threshold are around -24.1, -23.8, -24 and -22 dBm for 3.33-Gbit/s 16-QAM signals from Channel 1 to Channel 4, respectively. The BER performances for the four channels have been balanced through digital pre-equalization. There are around 4-dB power penalties after 15-km fiber transmission, which are mainly attributed to chromatic dispersion induced power fading and increased amplified spontaneous emission (ASE) from the EDFA. In UL transmission, the receiver sensitivities at BER of 3.8E-3 are about -25, -23.2, -22.5, and -21.4 dBm for Channel 1 to 4 respectively. The power penalty induced by fiber transmission is around 2.5 dB. The constellations of 25,000 error-free DL and UL 16-QAM symbols after fiber transmissions are shown in Figure 19(a) and (b) with corresponding received optical signal powers around -5 and -7 dBm, respectively. Less than 7% EVM can be obtained for all the four channels. The constellation- dependent noise distribution could be attributed to the residual phase noise and nonlinear distortions from the electrical amplifications. After extracting the AxC chips and performing 8-to-15-bit decompressions, the encapsulated 5G-NR-like wireless OFDM signals with a sampling rate of 245.76 MHz can be reconstructed. The selected

constellations of those 5G-NR-like signals with 64-, 256-, and 1024-QAM are shown in Figure 20(a) to (c) respectively. Less than 0.58% EVM values have been obtained. Typically, because of nonlinear distortions and noise floor, without the help from compressed D-RoF techniques, such low EVM values and high-order modulation formats are very challenging to be achieved in conventional A-RoF systems after 15-km fiber transmission.

2.4 Novel Data-Compression Technologies for Digital Mobile Fronthaul with Lloyd Algorithm and Differential Coding

2.4.1 Motivation and Backgrounds

The continuously-growing performance requirements of 5G new-radio (NR), high-speed internet access, and high-resolution multi-media entertainment with virtual reality have fostered great R&D challenges for future fiber-wireless integrated mobile fronthaul (MFH), where an upgrade of system capacity and spectral efficiency is urgently needed. The latest 5G-NR specifications are featured by orthogonal frequency-division multiplexing (OFDM) and higher order of modulations (256 and 1024-QAM). However, to bring about desirable operation flexibility and higher spectral efficiency, integration of these two technologies also leads to several new challenges, such as high sensitivity to nonlinear distortions and increased requirements on high-resolution digital-to-analog converters (DAC), which limit the quality and transmission distance of analog radio-over-fiber (A-RoF) optical networks in MFH [9], [14], [72]. On the other hand, digital RoF (D-RoF) [24], [28], [73] becomes a preferred technology recently. It is compatible with different formats, which is suitable for 5G NR environment with diverse services and

spectrum. It also has high immunity to nonlinear distortions. Error-free transmissions can be realized when using forward-error-correction (FEC) coding. The shortcoming of low bandwidth efficiency can also be mitigated with data compression [28], [73] and advanced modulation formats, which makes D-RoF as a promising candidate to digitally transport high-quality wireless signals between the baseband unit pool (BBU-pool) and radio access units (RAU) with increased transmission distance and improved power budgets.

In this section, relaxed Lloyd (R-Lloyd) algorithm is proposed to further improve the compression efficiency of D-RoF MFH supporting 1024-QAM and beyond in latest 5G-NR specifications. In this approach, traditional Lloyd algorithm is used to determine the major quantization levels and uniform interpolation is applied to calculate the minor quantization levels. An optimal trade-off is obtained between computational complexity and signal quality. Compared with existing methods such as partial-bit sampling (PBS), μ-law, and A-law [73], the quantization noise can be reduced by as large as 4.8-dB. Different from other statistical estimation methods [73], Lloyd algorithm is format agnostic and applicable to non-Gaussian modulation formats, like single-carrier frequency-division multiplexing (SC-FDM). Meanwhile, differential pulse code modulation (DPCM) is also employed in the compression process to further suppress the quantization noise, where a 1.4-dB improvement in signal-to-quantization-noise ratio (SQNR) is achieved. The proposed technology is experimentally demonstrated over a 180-Gbit/s coherent optical fronthaul system encapsulating 64×100-MHz 5G-NR carriers with 1024-QAM. The compression performance under the influence of bit errors is also measured.

2.4.2 Operation Principles

The operation process of the digital RoF system is shown in Figure 21(a). The analog wireless OFDM waveform is firstly sampled into a discrete signal. Each data sample is then quantized with 2U levels and converted into a binary AxC chip with U digits. In the standard of common public radio interface (CPRI), $U = 15$. Through compression process, each AxC chip is mapped from U digits to V digits ($V < U$) and the bandwidth efficiency can thus be improved by $(U - V)/V \times 100\%$. The Lloyd algorithm [74] is based on minimum mean-square error (MMSE) criterion. It firstly divides the probability density function (PDF) of the signal amplitudes into multiple segments with the boundaries defined by the thresholds $[t_i \ \ t_{i+1}]$ as shown in Figure 21(b). After quantization, the amplitudes falling into each segment will be quantized as level li. To minimize the MSE between the quantized and original signals, $\{t_i, \ t_{i+1}\}$ and l_i are related by

$$l_i = \int_{t_i}^{t_{i+1}} xf(x)dx \Big/ \int_{t_i}^{t_{i+1}} f(x)dx \tag{2.10}$$

and

$$t_i = \left(l_i + l_{i+1}\right)/2 \tag{2.11}$$

where $f(x)$ is the PDF of signal amplitudes. The flow diagram of R-Lloyd algorithm is shown in Figure 21(c). Firstly, the quantization thresholds are initiated as $(t_{1,0}, t_{2,0}, \dots, t_{2P+1,0})$ with uniform separations, where P is the number of major digits. Then the quantization levels $(l_{1,1}, l_{2,1}, \dots, l_{2P,1})$ are calculated using $(t_{1,0}, t_{2,0}, \dots, t_{2P+1,0})$ based on Equation (2.10). Similarly, $(t_{1,1}, t_{2,1}, \dots, t_{2P+1,1})$ are subsequently obtained using

$(l_{1,1}, l_{2,1}, \dots, l_{2P,1})$ and Equation (2.11). Following the loop as shown in Figure 21(c), the quantization thresholds and levels are repeatedly updated based on their counterparts' former values until the iteration index reaches M. In this process, both quantization levels and thresholds gradually converge to the positions resulting in the minimum MSE between original and quantized signals.

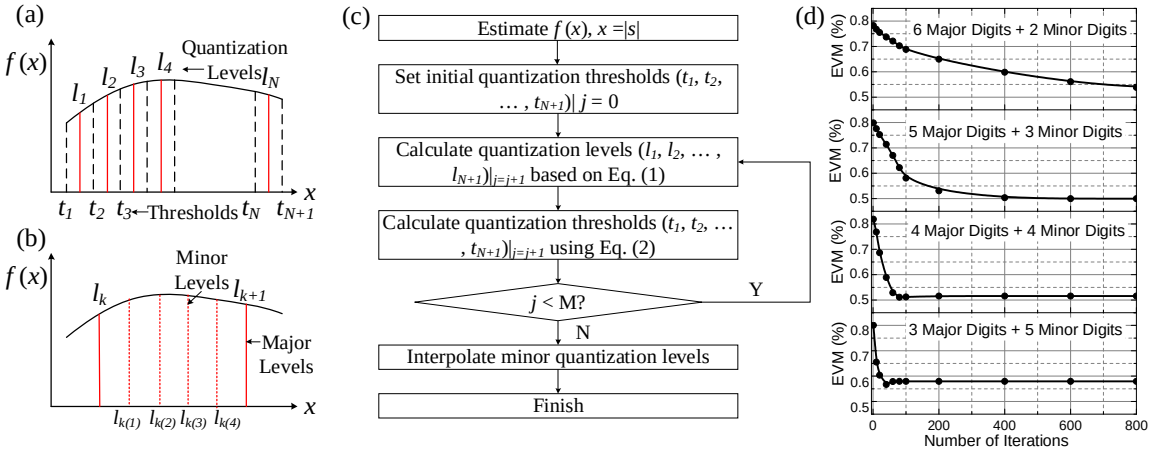

Figure 21. (a) – (c) Operation principles of Lloyd algorithm based data compression; (d): EVM versus number of iterations.

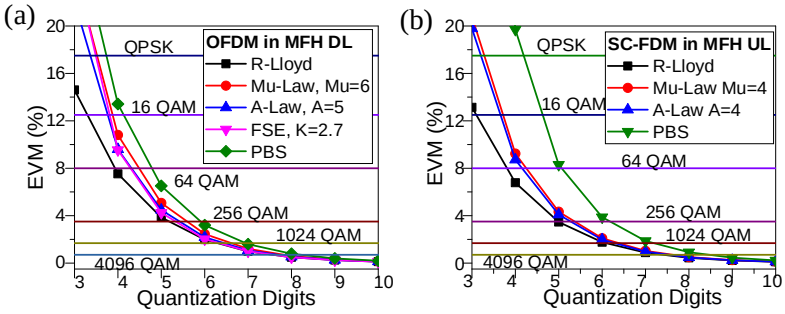

Figure 22. EVM versus quantization digits when Lloyd method is used for OFDM and SC-FDM respectively.

Given the compressed AxC chip with V digits, to reduce the complexity of traditional Lloyd algorithm, R-Lloyd method is used where 2^P out of 2^V levels are computed using

Lloyd algorithm first as the major levels and $2^{(V-P)}$ minor quantization levels are uniformly interpolated between $[l_i \ l_{i+1}]$. The selection of P and V is determined by a trade-off between the quantization accuracy and convergence speed. The OFDM error-vector-magnitude (EVM) convergence speed when applying different number of major digits is shown in Figure 21(d) under 15-to-8-digits compression (U=15 and V=8). It is observed that, with fewer major digits, faster convergence speed can be achieved with fewer number of iterations. When applying 4 major digits (P=4), the converged EVM value can be obtained with 100 iterations. To balance the complexity and accuracy, 4 and 5 major digits are recommended. The EVM performances of OFDM and SC-FDM radio signals after 15-to-8-digit compression and de-compression are shown in Figure 22(a) and (b) respectively. It is noticed that, compared with other existing methods, e. g., μ-Law, A-Law, or FSE, R-Lloyd algorithm can achieve the best EVM performance, especially with a fewer number of quantization digits. Meanwhile, some methods, like FSE [73], are specially designed for OFDM signal with Gaussian distributed amplitudes. They fail to work under non-Gaussian signals, like SC-FDM. However, the performance of Lloyd algorithm is independent of the signal's statistical property. As shown in Figure 22(b), good EVM is still obtained when using Lloyd algorithm to compress SC-FDM radio signals. The required EVM thresholds of 64-, 256-, 1024-, and 4096-QAM are set as 8%, 3.5%, 1.68%, and 0.7% [28], respectively.

Except from R-Lloyd algorithm, another important technique to further improve the signal quality after compression is DPCM. Compared with regular pulse code modulation (PCM), which digitizes the original radio signal x(k), DPCM is used to predict and digitize the differential signal, e. g., $x(k) - x(k-1)$. The concept of DPCM is based on that most

source signals exhibit some correlations between successive samples and through differential precoding, the correlation induced redundancy can be reduced which enables representing the information with fewer digits. To reduce the complexity, first-order differentiator is used with the pre-coded signals denoted as $d(k) = x(k) - \beta x(k-1)$ here. In simulations, the value of β is optimized to be 0.6. Two important issues to be addressed in DPCM are the quantization error in the compression process and decision error at the DPCM decoder. Those two kinds of errors will be propagated and accumulated subsequently from the beginning towards the end of the whole frame, which seriously degrades the quality of the reconstructed analog RF signals. Therefore, a feedback loop based differential quantizer [74] is applied to mitigate the quantization error transferring issue.

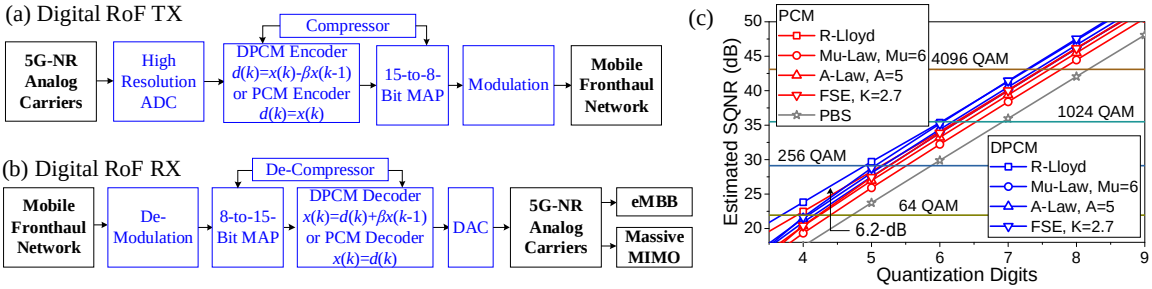

Figure 23. (a)-(b): System architecture of D-RoF transmitter and receiver respectively in 5G-MFH. (c): SQNR as a function of quantization digits when different coding plus compression methods are applied. eMBB: enhanced mobile broadband.

2.4.3 Experimental Results and Discussions

The architectures of the transmitters and receivers in D-RoF based MFH are shown in Figure 23(a) and (b) respectively. A simple IM/DD link is set up to test the performance of compressed D-RoF link. At the transmitter, one 20-MHz LTE OFDM component is sampled with a resolution of 15-digit/sample at a sampling rate of 30.72-MHz. Then

DPCM or PCM encoders integrated with Lloyd based quantizers are used to convert the quantized samples into binary AxC chips. A 15-to-8-bit map is used to compress each AxC chip from 15-bit/chip to 8-bit/chip. The compressed AxC chips are interleaved and mapped into NRZ symbols. At the receiver site, a set of reversed procedures is used to reconstruct the analog components from decompressing the digital signals. The recovered analog component carriers will be sent to wireless antennas in RAUs. The EVM performances of the recovered analog signals are compared between DPCM and PCM encoded schemes. It is observed that, if DPCM is used instead of PCM, there is around 1.4-dB improvement in SQNR, which is estimated as $SQNR \approx 1/EVM^2$. Compared with partial bit sampling (PBS) with low-order digits directly removed, around 6.2-dB gain in SQNR is obtained when combining DPCM with Lloyd algorithm.

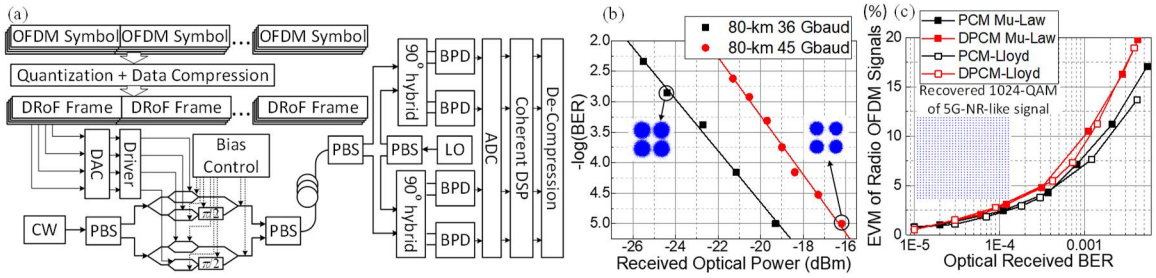

Figure 24. (a): System diagram of high-capacity digital MFH based on coherent transmission technology. (b): BER versus received optical power. (c): EVM of recovered wireless signal under the influence of bit errors. BPD: balanced photodetector.

A 5G-NR compatible digital MFH link based on coherent optical transmission system is shown in Figure 24(a). 5G-NR-like OFDM symbols are digitized and encapsulated into AxC chips, which are interleaved and packetized into D-RoF frames. A dual-polarization IQ modulator (DP-IQM) is used to modulate four streams of D-RoF signals for I and Q tributaries on both polarizations based on QPSK modulation formats. After 80-km SSMF transmission, the signals are fed into the coherent receiver and then

followed by a 4-channel real-time sampling oscilloscope before applying offline digital signal processing for signal recovery. DP-QPSK with 128- and 180-Gbps data rates are applied, which can encapsulate 48 and 64 100-MHz 5G-NR-like OFDM components with 1024-QAM respectively. The BER performance of DP-QPSK and selected constellation of recovered OFDM signal with 0.46% EVM under error-free coherent transmission are shown in Figure 24(b) and (c) respectively. The quality of the recovered OFDM signal under the influence of bit errors is also tested as shown in Figure 24(c). It is observed that, because of error transferring issue in differential decoding, DPCM is more sensitive towards the bit errors than PCM methods. It is expected that the issue can be mitigated by applying Reed-Solomon FEC coding (RS-FEC 528/514) according to CPRI specifications and it will be studied in our future work.

2.5 Summary

In summary, we have demonstrated two critical technologies including flexible data compression and multiband modulation for improving the TE, flexibility, and multi-RAT compatibility in next-generation MFH networks.

In order to achieve efficient data compression, a TFG-FSE based algorithm is proposed, which is based on Gaussian amplitude distribution in OFDM signals and using TFG function bounded by 0 to Kσ to approximate the real PDF of the modulus. Compared to the existing data compression techniques such as PBS, FBNQ, μ-law, and A-law, lower quantization error and high computational efficiency have been achieved. Furthermore, through combining data compression, re-sampling, and advanced modulation formats, the TE of an MFH network is significantly boosted. In the experimental demonstration of a

25-Gbit/s IM-DD D-RoF based MFH over 20-km SSMF transmission, 54 20-MHz LTE-like CCs are encapsulated and TE is proved to be improved by around 5 times compared with existing CPRI based scheme. Meanwhile, high transmission quality is realized that, for 8-to-15-bit decompressed LTE signals, 0.56% error-vector magnitudes (EVM) and 23-dB system margin below the 64-QAM EVM threshold are obtained.

In addition, a frequency-domain multiband multiplexing based D-RoF interface is proposed to upgrade existing time-domain interleaving based scheme. With multiband multiplexing, different DCCs don't need to be interleaved by the same sampling clock thus improving the flexibility and multi-RAT compatibility of the MFH. Multiband modulation also enables PTMP UL transmission because it does not require strict synchronization among distributed RAUs when using digital-filtered CAP modulations. A proof-of-concept experiment is conducted over a bidirectional MFH with a symmetric capacity of 13.3 Gbit/s which is able to deliver 6.4-Gbit/s four-band 5G-NR-like signals with 1024-QAM modulation between BBU-Pool and two RAUs. Good BER performance and high-quality constellations of 64-, 256-, and 1024-QAM are achieved which shows that, superior to traditional CPRI or A-RoF based schemes, highly compressed multiband D-RoF technology can also be a desired option for future format-transparent high-capacity MFH supporting 5G-NR systems.

Moreover, we have also designed, for the first time, the combinational data-compression algorithms based on both Lloyd algorithm and DPCM to improve the SQNR and bandwidth efficiency in D-RoF systems for next-generation 5G-NR-compatible digital MFH. With 8-digit quantization, the proposed D-RoF link is capable to support up-to 4096-QAM OFDM or SC-FDM formats with up to 6.2-dB SQNR improvement. In addition, 128

and 180-Gbps high-capacity MFH links based on coherent transmission technology have been demonstrated for transmitting 48 and 64×100-MHz 5G-NR-like OFDM components, respectively, with high-order 1024-QAM format.

CHAPTER 3. MULTIBAND CAP MODULATION FOR SPECTRAL EFFICIENT DATA MULTIPLEXING IN MOBILE FRONTHAUL WITH ADVANCED DIGITAL FILTER DESIGN

In this chapter, to the first time, we demonstrate an offset-QAM carrier-less amplitude and phase modulation (OQAM-CAP) technique for spectral efficient multiband mobile fronthaul systems. In comparison with traditional QAM based CAP multiband modulation, the digital filter for each channel in OQAM-CAP can be adaptively redesigned to obtain either higher spectral efficiency or lower computational complexity. Two kinds of digital filters, namely, square-root raised-cosine (SRRC) filters and isotropic orthogonal transform algorithm (IOTA) based filters, are studied and applied to shape the frequency window of each channel in multiband systems. We compared the performances among SRRC-OQAM CAP, IOTA-OQAM CAP, and traditional SRRC-QAM CAP. It is experimentally demonstrated that SRRC-OQAM-CAP can achieve higher spectral efficiency, IOTA-OQAM-CAP can obtain higher computational efficiency, and SRRC-QAM-CAP can be used in uplink transmission with lower inter-channel interference. Bidirectional experiments are conducted with around 2-GHz nine aggregated channels on 60-GHz optical millimeter wave. Less than 7% error vector magnitudes are realized over 15-km standard single-mode fiber and 1.5-m wireless channel.

3.1 Introduction of Multiband Modulation in Mobile Fronthaul Networks

The continuous growth of demands in ubiquitous high-speed wireless services has triggered the investigation of next generation high capacity radio over fiber (RoF) systems

[75], [76]. Meanwhile, millimeter wave (MMW) technologies have already been standardized in emerging wireless local access network (WLAN) protocol IEEE 802.11ad [77], and 28-GHz or 38-GHz bands are very hopeful to be applied for future fifth generation (5G) mobile data network [78]. Thus, it can be forecasted that MMW RoF systems can become a strong candidate in fiber-wireless integrated mobile fronthaul network to provide multi-band, multi-service, and multi-user access solutions in the near future.

To meet these goals, one of the key enabling techniques to increase the system capacity as well as scalability is to densely aggregate multiple single-carrier channels with advanced modulation formats and digital filtering techniques. Tremendous works have been done in this regime including quadrature amplitude modulated carrier-less amplitude and phase (QAM CAP) modulated multiband [67], [79], Nyquist wavelength division multiplexing (N-WDM) or frequency division multiplexing (N-FDM) [49], [80], [81], Nyquist super channel (NSC) generation [52] - [57], and quadrature duobinary processing (QDP) [58], [59].

However, in QAM CAP and N-WDM, raised-cosine (RC) or square-root raised-cosine (SRRC) filters are typically used in pulse shaping of each channel to eliminate the undesired out-of-band power leakage. Nevertheless, there are several issues if RC or SRRC filters are used with traditional QAM modulation. Above all, the bandwidth occupied by each channel is beyond Nyquist bandwidth. If we use roll-off factor, β, to measure the ratio between the excess bandwidth and the Nyquist bandwidth, the spectral efficiency (SE) will be reduced by a factor of $1/(1+\beta)$. Furthermore, in real implementations on digital domain, the pulse shape of a filter is truncated and digitized to generate finite-impulse-response (FIR) filter taps. When the truncated time span is increased, the frequency

response of the digital filter approaches its ideal shape at the expense of increased number of taps and computational complexity. However, when β is small, e. g. β = 0.25, the truncation with insufficient time duration will result in large out-of-band sidelobes [60] which will leak into the adjacent channels thus degrading the signal-to-interference-plus-noise ratio (SINR). On the other hand, the schemes based on NSC or QDP can approach or even be claimed to exceed Nyquist limit [61]. However, they require adaptive filtering as well as differential coding and decoding processes which adds to the complexity, delay, and cost at the transmitter and receiver sides.

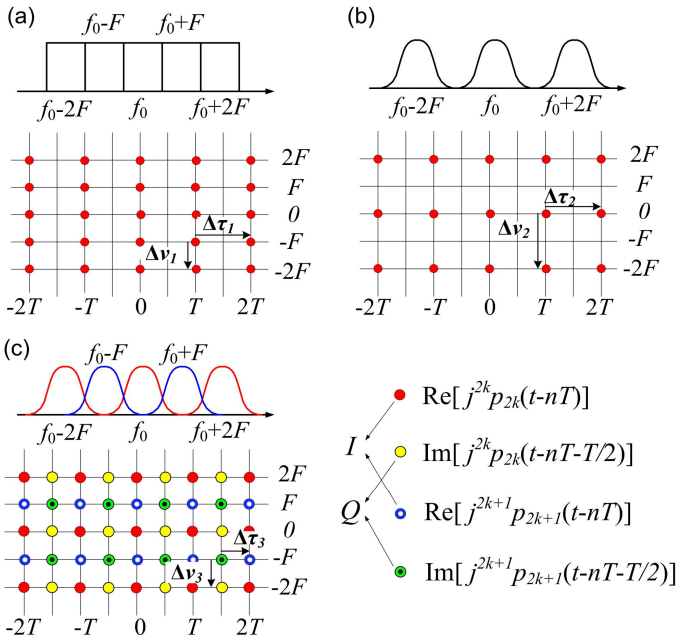

Figure 25. Power spectrum and time-frequency lattice structure of (a) QAM CAP multiband with rectangular filtering; (b) OQAM CAP with only one subset of lattice points; and (c) OQAM CAP with staggered four subsets of lattice points.

In this chapter, we propose to use isotropic orthogonal transform algorithm (IOTA) based filters [51], [82] and SRRC filters with large roll-off factors as the frequency window of each CAP channel and applying off-set QAM (OQAM) modulation in an RoF system supporting multiuser and multiservice. In comparison with traditional QAM CAP

multiband modulation, experimental results demonstrate that higher SE with lower computational complexity can be achieved in downlink (DL) transmission. When IOTA filters are used, SE can be improved by 9% with 50% - 85% less number of filter taps. While slow -decaying SRRC filters are used with $\beta = 0.5$, SE can be improved by 12% with 30% - 70% less number of taps. However, traditional QAM CAP can still be used in uplink (UL) transmission because the adjacent channels are isolated with each other and they do not require strict synchronization. Proof-of-concept experiments are conducted on a bidirectional intensity-modulation/direct-detection (IM/DD) RoF testbed. The testbed operates with an MMW frequency around 60 GHz. Bidirectional transmissions of 2.25-GHz 9 aggregated channels modulated with quadrature phase shift keying (QPSK) and 16QAM are realized over 15-km standard single-mode fiber (SSMF) and 1.5-m wireless channel.

3.2 Fundamental Concepts and Principles

In traditional multi-band CAP modulation schemes, the transmitted signal can be derived as

$$\begin{aligned} x(t) &= \mathrm{Re}\left[\sum_n \sum_k s_k(n)\, p_k(t-nT)\right] \\ &= \sum_n \sum_k \{I_k(n)\,\mathrm{Re}[p_k(t-nT)] - Q_k(n)\mathrm{Im}[p_k(t-nT)]\}, \end{aligned} \tag{3.1}$$

Where k is the channel index; $s_k(n)$ is the n^{th} complex data symbol modulated on the k^{th} carrier with its real and imaginary parts denoted as $I_k(n)$ and $Q_k(n)$ respectively; $p_k(t) = p(t)e^{j2\pi f_k t}$ is the pulse up-converted by the k^{th} carrier at the frequency of f_k; $p(t)$ is the pulse of the selected prototype filters; and T is the symbol duration. If $s_k(n)$ is

a QAM symbol, in order to recover the signals without contamination from the adjacent symbols, matched filtering demodulation technique is used and $p_k(t)$ should meet the orthogonality condition as [83]

$$\int_{-\infty}^{+\infty} p_k(t-mT)\, p_l^*(t-nT)\mathrm{d}t = \delta_{kl}\delta_{mn}\,, \tag{3.2}$$

where * denotes a complex conjugate operation. Define $\mathcal{A}\big((f_k - f_l),(m-n)T\big) = \int_{-\infty}^{+\infty} p_k(t-mT)\, p_l{}^*(t-nT)dt$ as the ambiguity function of the filter's time response $p(t)$ and consider a QAM modulated multiband system using rectangular filters with multiple channels centered at $f_k = kF, k = 0, \pm 1, \pm 2, \ldots$. Then $\mathcal{A}$ can be mapped onto a time-frequency phase space as shown in Figure 25(a), where the unit lattice area is $\Delta\tau_1\Delta\nu_1 = TF = 1$. Because of the orthogonality defined in Equation (3.2), after matched filtering, the QAM symbols carried by pulses at one lattice point is free from the interference generated by the symbols at the other points.

However, except from the filters with $\Delta\tau_1\Delta\nu_1 = 1$, like rectangular filters, there exists another set of filters which satisfies the relaxed orthogonality condition with $\Delta\tau_2\Delta\nu_2 = 2$ as

$$\int_{-\infty}^{+\infty} p_{2k}(t-mT)\, p_{2l}^*(t-nT)\mathrm{d}t = \delta_{kl}\delta_{mn}\,, \tag{3.3}$$

and the extreme points of its ambiguity function are depicted in Figure 25(b). The relaxation of the orthogonality condition loosens the criteria in filter design and enables us to use new types of prototype filters. Although the lattice density of such a system is halved in comparison with that in Figure 25(a), by applying lattice staggering [51] in combination

with OQAM modulation, the SE can be even higher. The simplified concept of lattice staggering is illustrated in Figure 25(c). By duplicating and shifting the lattice points shown in Figure 25(b), we achieve a time-frequency lattice space with a unit lattice area of $\Delta\tau_3\Delta\nu_3 = 0.5$ as shown in Figure 25(c), which is composed of four subsets of lattice points highlighted as red, yellow, blue, and green. Suppose that $p(t)$ is an even function, i. e., $p(t) = p(-t)$; the modified inner products between red and yellow, red and blue, as well as red and green subsets can be derived as

$$\int_{-\infty}^{+\infty} \mathrm{Re}\left(j^{2k} p_{2k}(t-mT)\right) \mathrm{Im}\left((-j)^{2l} p_{2l}^{*}(t-nT-T/2)\right) \mathrm{d}t = 0\,, \tag{3.4}$$

$$\int_{-\infty}^{+\infty} \mathrm{Re}\left(j^{2k} p_{2k}(t-mT)\right) \mathrm{Re}\left((-j)^{2l+1} p_{2l+1}^{*}(t-nT)\right) \mathrm{d}t = 0\,, \tag{3.5}$$

$$\int_{-\infty}^{+\infty} \mathrm{Re}\left(j^{2k} p_{2k}(t-mT)\right) \mathrm{Im}\left((-j)^{2l+1} p_{2l+1}^{*}(t-nT-T/2)\right) \mathrm{d}t = 0. \tag{3.6}$$

Equation (3.3) to (3.6) demonstrate that although the lattice density is doubled by introducing four subsets of lattice points on time-frequency phase space in comparison with that shown in Figure 25(a), the real or imaginary portions of the filters located on these points can still be orthogonal with each other, which enables us to design the new OQAM based CAP modulation format.

In OQAM CAP multiband modulation, the transmitted signal can be expressed as

$$x(t) = \sum_n \sum_k \begin{matrix} \{I_k(n)\,\mathrm{Re}[\,j^k p_k(t-nT)] \\ -Q_k(n)\mathrm{Im}[j^k p_k(t-nT-T/2)]\}\,, \end{matrix} \tag{3.7}$$

where $I_k(n)$ and $Q_k(n)$ can be recovered by using modified inner products defined in Equation (3.3) to (3.6). In comparison with QAM based CAP modulation demonstrated in Equation (3.1), there is a $T/2$ timing offset between the in-phase (I) and quadrature (Q) components which is in accordance with the definition of OQAM. Meanwhile it is worth noting that, in traditional QAM CAP modulation indicated by (1), each pulse $p_k(t-nT)$ can carry one complex QAM symbol with I and Q components on its real and imaginary portions respectively. However, in OQAM CAP modulation scheme, each pulse ($p_k(t-nT)$ or $p_k(t-nT-T/2)$) can only carry one real-valued pulse amplitude-modulated (PAM) symbol which contains half the information content compared with one QAM symbol. Thus, although the lattice density of OQAM CAP is doubled in comparison with that of QAM CAP, their quantities of information per unit area on the time-frequency phase space are the same. Nevertheless, as we will discuss in the following parts, in physically realizable systems with band-limited filters, OQAM CAP modulation is more spectral and computational efficient since it is built upon a relaxed orthogonal system which allows spectral overlap between adjacent channels as shown in Figure 25(c).

Based on Equation (3.1) and (3.7), the digital signal processing (DSP) block stacks of the transmitter and receiver for conventional QAM CAP and the proposed OQAM CAP modulation schemes are shown in Figure 26(a) and (b) respectively. The QAM CAP modulation is initiated by mapping the original bits to symbols of m-QAM, and then the mapped symbols are up-sampled to match the sampling rate of the shaping filter pairs. Next the up-sampled symbols are convoluted with digital filters where the discrete tap gain coefficients are generated by digitizing the baseband time response $p(t)$ mixed with a carrier component, $F(f_K) = \exp(j2\pi f_k t)$. Consequently, symbols from channel 1 to

channel K are pulse-shaped and up-converted to equally spaced intermediate frequencies (IFs) located from f_1 to f_k. After convolution, different signal bands are combined and fed into the digital to analog converter (DAC) before sent to the RoF transmitter.

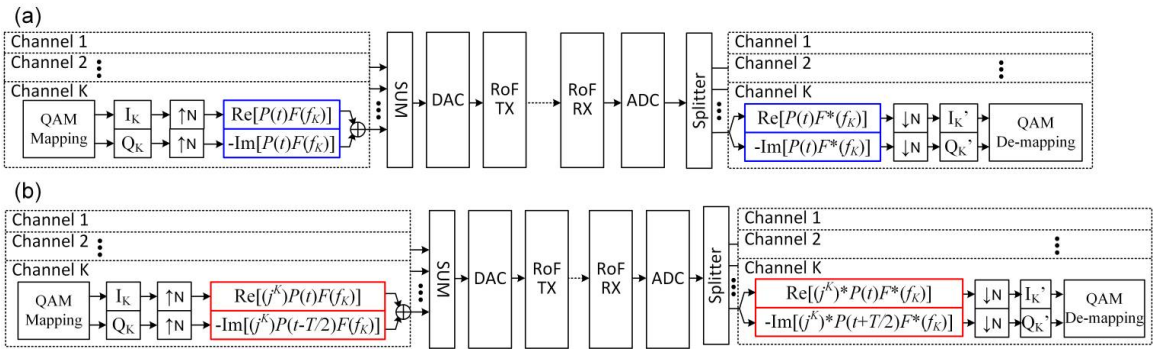

Figure 26. DSP blocks of generation and reception for CAP multiband modulation based on (a) traditional QAM and (b) OQAM.

At the receiver site, the analog signals are firstly over-sampled by an analog to digital converter (ADC). A group of matched filter pairs are applied to down-convert the signals and remove their out-of-band noise before down-sampling and QAM de-mapping. The up-sampling and down-sampling operations in the transmitter and receiver shown in Figure 26 are done by interpolating and deleting $N-1$ samples in every symbol period respectively. It is worth noting that in both QAM and OQAM CAP modulation schemes the real and imaginary parts of the complex filter taps are separated to filter the I and Q signal components respectively as indicated in Equation (3.1) and (3.7). For OQAM CAP multiband shown in Figure 26(b), the signal generation and reception process is similar to that shown in Figure 26(a) except that a periodic half-π phase shift factor, j^K, is multiplied to $p(t)$ and a $T/2$ timing off-set is introduced between the I and Q components which are consistent with Equation (3.7). In comparison, within each band, I and Q parts of QAM CAP multiband are synchronized without timing off-set.

3.3 Design and Comparison of Digital Filters Used in CAP Multiband

Since multiband CAP modulation divides the whole available spectrum into several sub-bands and uses filters as well as matched filters with orthogonal waveforms to separate data streams from different sub-bands, the digital filters need to be carefully designed and engineered. In this paper, we mainly focus on studying three categories of filters: fast-decaying SRRC filters, slow-decaying SRRC filters, and IOTA filters. The first one is used in QAM CAP and the latter two are used in OQAM CAP.

3.3.1 Introduction of IOTA Based Filters

IOTA targets to generate a set of filters which preserves the optimum time-frequency concentration property of Gaussian filters, and to modify them to satisfy the orthogonality condition in Equation (3.3). As we know, one interesting property of Gaussian filter is that the time response $\mathcal{G}(t)$ and its Fourier transform $G(f)$ maintains the same shape with an axis scaling factor σ, which can be modeled as

$$g(x/\sigma) \propto G(\sigma x)\,. \tag{3.8}$$

Although Gaussian filters have the best localization property compared to other filters and they decay fast in both time and frequency, they do not satisfy the orthogonality condition given in Equation (3.2) or (3.3) [84]. However, based on IOTA, we can force the Gaussian filter to satisfy Equation (3.3) and meanwhile maintaining its time-frequency concentration property.

Define $\mathcal{O}_a$, $\mathcal{F}$, and $\mathcal{F}^{-1}$ as the orthogonalization, Fourier transform, and inverse Fourier transform operators respectively. When they are applied to a particular function, we obtain the following relations:

$$\mathcal{O}_a x(u) = \frac{x(u)}{\sqrt{a\sum_{k=-\infty}^{\infty}\left|x(u-ka)\right|^2}}, \tag{3.9}$$

$$\mathcal{F}x(t) = \int_{t=-\infty}^{\infty} x(t)e^{-j2\pi ft}\mathrm{d}t, \tag{3.10}$$

$$\mathcal{F}^{-1}X(f) = \int_{f=-\infty}^{\infty} X(f)e^{j2\pi ft}\mathrm{d}f. \tag{3.11}$$

Then the orthogonalization process for Gaussian filter is expressed as

$$p(t) = \mathcal{F}^{-1}\mathcal{O}_{\nu 0}\mathcal{F}\mathcal{O}_{\tau 0}g(t). \tag{3.12}$$

After orthogonalization, given $\Delta\tau_0\Delta\nu_0 = 0.5$, null points at $\nu = \pm 1/\tau_0, \pm 2/\tau_0, \pm 3/\tau_0, \ldots$ and $\tau = \pm 1/\nu_0, \pm 2/\nu_0, \pm 3/\nu_0, \ldots$ will be introduced in its ambiguity function $\mathcal{A}_p(\nu,\tau)$. Therefore, the unit lattice area $\Delta\tau \cdot \Delta\nu = 1/\tau_0\nu_0 = 2$, and by applying time-frequency scaling transform, it can be proved that $p(t)$ satisfies the relaxed orthogonality condition given in Equation (3.3). The frequency and time responses among IOTA, Gaussian, and SRRC filters (roll-off factor = 0.5) are compared in Figure 27(a) and (b) respectively. It is observed that there is a trade-off between localization in time and frequency domains for SRRC filters. However, both IOTA and Gaussian filters yield isotropic response in time and frequency with optimally-concentrated distributions. Gaussian filters decay faster than IOTA filters but, with periodic notches on its time-

frequency response, IOTA filters fulfill Nyquist orthogonal criterion after matched filtering. On the other hand, it is shown that while SRRC filters have higher immunity to the dispersions in time domain, Gaussian and IOTA filters yield a better balance in doubly dispersive channels [83].

3.3.2 Time and Frequency Responses of Multi-Band CAP Systems Using SRRC and IOTA Filters

A multiband QAM CAP system with a time-frequency grid shown in Figure 25(a) reaches the so-called Nyquist limit [61] with a maximal SE for inter-symbol interference (ISI) and inter-channel interference (ICI) free transmissions. However, such a limit is difficult to be obtained in traditional N-WDM or N-FDM systems because it requires the use of rectangular filters which are physically unrealizable. In a typical system with SRRC filtering, the roll-off coefficient β will reduce the SE by a factor of $1/(1+\beta)$ and the strict orthogonality condition is thus adjusted to

$$\begin{aligned}&\int_{-\infty}^{+\infty} p_k(t-mT)\,p_l^*(t-nT)\mathrm{d}t\\&=\int_{-\infty}^{+\infty} p(t-mT)\,p^*(t-nT)e^{j2\pi(k-l)\cdot(1+\beta)Ft}\mathrm{d}t\\&=\delta_{kl}\delta_{mn}\end{aligned}. \tag{3.13}$$

For example, in standards of IEEE 802.11ad and IEEE 802.15.3c, roll-off factor of SRRC filters can be set to 0.25 in single-carrier modulations [85]. It is worth noting that when β approaches 0, the SE also approaches Nyquist limit, but such a quasi-rectangular filter requires an infinitely large number of taps which will tremendously increase the computational complexity at DSP part. However, the above issue can be resolved by loosening the orthogonality condition from Equation (3.2) to (3.3) and applying OQAM

modulation. It can be proved that both SRRC and IOTA filters satisfy the relaxed orthogonality condition in Equation (3.3), which indicates either of them can be used as a prototype filter to build an OQAM based multiband CAP system.

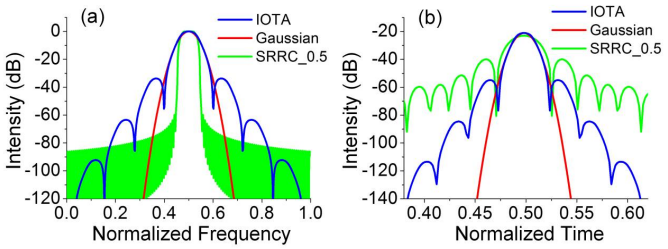

Figure 27. (a) Frequency and (b) time responses of IOTA, Gaussian, and SRRC (roll-off factor = 0.5) filters.

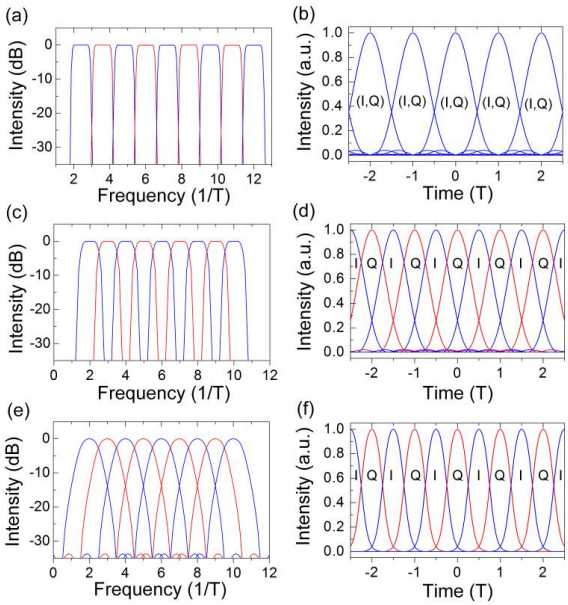

Figure 28. Spectral and time responses different signals.

Figure 28(a) to (f) compared the frequency and time responses of SRRC-QAM, SRRC-OQAM, and IOTA-OQAM multiband CAP. As shown in Figure 28(b), envelopes of I and Q components are exactly coincided in SRRC-QAM system, while they are interleaved by $T/2$ under OQAM schemes as shown in Figure 28(d) and (f). The advantage of SRRC-QAM lies in that there is no overlap between adjacent channels, as shown in

Figure 28(a), which extinguishes it as a promising modulation format for uplink transmission. Because the channels used by different users are isolated with each other without crosstalk and they don't need to be strictly synchronized. SRRC-QAM CAP can also achieve high SE with a small roll-off factor at the expense of greatly increased computational complexity.

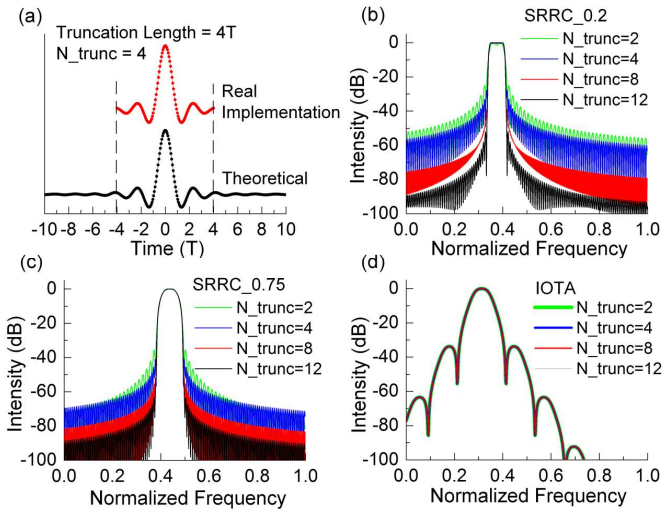

Figure 29. (a) Truncation of digital filters and its effect on (b) fast-decaying SRRC filters, (c) slow-decaying SRRC filters, and (d) IOTA filters.

Nonetheless, as shown in Figure 28(c) and (e), the adjacent channels in SRRC-OQAM and IOTA-OQAM can be overlapped and the interference can be cancelled out by applying Equation (3.4) to (3.6) when signals are synchronized with a half-π phase shift between the adjacent bands. OQAM-CAP systems do not require filters with a fast decay. Thus, IOTA or slow-decaying SRRC filters with a large roll-off factor (e. g. $\beta = 0.5$) can be used as the window functions to generate the densely aggregated channels operating at Nyquist limit. In the following parts, it is demonstrated that, when IOTA or slow-decaying SRRC filters are used in OQAM CAP multiband, the required number of filter taps can be

reduced, which significantly increases the computational efficiency (CE) and meanwhile maintaining a high SE.

3.3.3 Truncation Effect and Its Influence on Multi-Band Systems

In real applications, the time response of the digital FIR filters cannot last infinitely. As shown in Figure 28(a), the pulse shape has to be truncated from $-N_{trunc}T$ to $+N_{trunc}T$, where N_{trunc} is a positive real number. However, the truncation of SRRC filters results in strong out-of-band side lobes in frequency domain as shown in Figure 28(b) and (c). It is observed that the side lobes become stronger when N_{trunc} decreases. As shown in Figure 28(b), given a roll-off factor of 0.2, the normalized power of the first order side lobe increases from -51 dB to -25 dB when N_{trunc} is reduced from 12 to 2. However, those undesired sidelobes grow much slower with slow-decaying SRRC filters ($\beta = 0.75$) as shown in Figure 28(c). To control the out-of-band leakage, a large N_{trunc} is required especially when β is small, which on the other hand, increases the number of taps and reduces the CE. However, because of the fast decay in both time and frequency domain, IOTA filters are insensitive to truncation effect. As shown in Figure 28(d), no side lobe higher than -100 dB is observed when N_{trunc} is reduced from 12 to 2.

Suppose the window function $w(t)$ used for truncation is a rectangle which can be written as

$$w(t) = \begin{cases} 1 & -N_{trunc}T \le t \le N_{trunc}T \\ 0 & \text{otherwise} \end{cases}, \tag{3.14}$$

with its Fourier transform as

$$W(f) = N_{trunc} T \,\mathrm{sinc}(N_{trunc} T \cdot f) \ . \tag{3.15}$$

Then the truncated pulse $P_{trunc}(t)$ is obtained by multiplying $w(t)$ with the original pulse $P(t)$ in time domain which corresponds to convolution in frequency domain as follows [60]:

$$H_{trunc}(f) = \int_{-\infty}^{\infty} H(\varphi) W(f - \varphi) \mathrm{d}\varphi \,, \tag{3.16}$$

where $H_{trunc}(f)$ and $H(f)$ are the frequency responses of $P_{trunc}(t)$ and $P(t)$ respectively at Channel A. Given an adjacent channel B with the frequency response as $G_{trunc}(f - F)$; then the normalized power of the inter-channel crosstalk (ICC) leaking from Channel A to B after matched filtering can be deduced as [86]

$$P_{crosstalk} = \int_{-\infty}^{\infty} H_{trunc}(f) G_{trunc}(f - F)^{*} e^{j2\pi ft} \mathrm{d}f \ . \tag{3.17}$$

Equation (3.15) to (3.17) could help us qualitatively analyze the results from truncation effects which are demonstrated in the following parts.

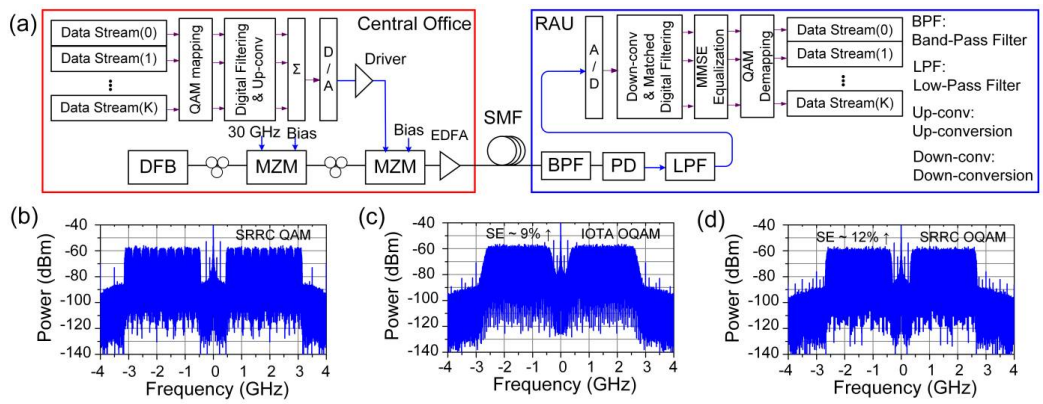

Figure 30. (a) Experimental set-up to study truncation effect on digital filters. (b)–(d) Electrical spectra of SRRC-QAM, IOTA-OQAM, and SRRC-OQAM CAP respectively.

Simulations and experiments are conducted to study the signal quality degradation resulted from truncation induced ICC. In the simulations for both QAM and OQAM CAP, nine bands are aggregated from 0 to 3 GHz and the symbol rate for each band ($1/T$) is 250 MHz. The separations between the adjacent bands are $(1+\beta)/T$ and $1/T$ for QAM CAP and OQAM-CAP respectively. QPSK is applied and the signal-to-noise ratio of the system is set to be 24dB. The simulated error-vector-magnitude (EVM) performances of the received signal are shown in Figure 31(a) to (c). As indicated in (15) and (16), the main lobes in $W(f)$ becomes stronger with a smaller N_{trunc}, which thereby increases the span of $H_{trunc}(f)$. Consequently, the overlapping region between $H_{trunc}(f)$ and $G_{trunc}(f-F)$ becomes larger. Thus, in general, the EVM performances for all the scenarios are deteriorated with a short truncation length. As shown in Figure 31(a) to (c), because of larger pulse durations in the time response, fast-decaying SRRC filters with a small roll-off factor are more vulnerable to truncation effect in both OQAM and QAM cases. Meanwhile, given the same roll-off factor, the EVMs of OQAM CAP are slightly worse than that of QAM-CAP, which is attributed to the smaller channel separations in OQAM CAP. Nevertheless, among all the cases, IOTA-OQAM CAP can achieve the best EVMs.

The EVM penalties are insignificant even with a truncation length less than $1.25T$. To achieve a small EVM less than 5%, IOTA-OQAM CAP, SRRC-OQAM CAP with $\beta = 1.0$, and SRRC-QAM CAP with $\beta = 0.2$ require truncation lengths of at least $1.25T$, $1.75T$, and $4.25T$ respectively, while the SRRC-QAM CAP will also reduce the SE by 20% ($\beta = 0.2$). It is worth noting that the ripples of the curves shown in Figure 31(a) to (c) are resulted from the integration of the sinc functions in (3.16) and (3.17).

An experiment with the set-up shown in Figure 30(a) was conducted to study the transmission performance degradation resulted from truncation effect. Three modulation formats are compared in the experiment, namely, the SRRC-QAM CAP (β = 0.08, 0.12, 0.2, and 0.3), IOTA-OQAM CAP, and SRRC-OQAM CAP (β = 0.25, 0.5, 0.75, and 1.0). For all the scenarios, nine bands are aggregated with 250-MHz baud rate for each band. At the central office (CO), light is firstly modulated by a 40-GHz Mach-Zehnder modulator biased at minimum intensity-output point to generate optical-carrier-suppressed (OCS) two tones with 60-GHz spacing. Then the second-stage Mach-Zehnder modulator (MZM) is quadrature biased to modulate the multiband CAP signals onto the lights. After 15-km standard-single-mode-fiber (SSMF) transmission, at the remote-access-unit (RAU) site, one of the two sidebands is filtered out by an optical filter, and the signals carried by the remaining sideband are directly detected by a photo detector (PD). By doing this, we avoid the extra penalties from chromatic dispersion after fiber transmission as well as electrical nonlinearities in 60-GHz detection, amplification, and down-conversion processes, which could distort the results of comparisons. The electrical spectra of the SRRC-QAM ($\beta = 0.2$), IOTA-OQAM, and SRRC-OQAM CAP ($\beta = 0.5$) signals before transmission are shown in Figure 30(b) to (d) respectively. When the channels are densely aggregated at

Nyquist limit, the 20-dB bandwidths occupied by IOTA-OQAM and SRRC-OQAM CAP modulations are reduced by at least 9% and 12% respectively. At the receiver site, after matched filtering and digital down-conversion, a frequency-domain equalizer (FDE) [87] is applied to eliminate the ISI resulted from the chromatic dispersion and electrical filtering. The equalizer coefficients are estimated using minimum-mean-square-error (MMSE) algorithm with training sequences. The measured EVMs versus truncation lengths are shown in Figure 31(d) and (e) where the colored dots represent the experimental results and the dashed curves are fitted from the corresponding simulation results. It is observed that the experimental results are perfectly matched with the simulation results which further verifies the above theoretical analysis.

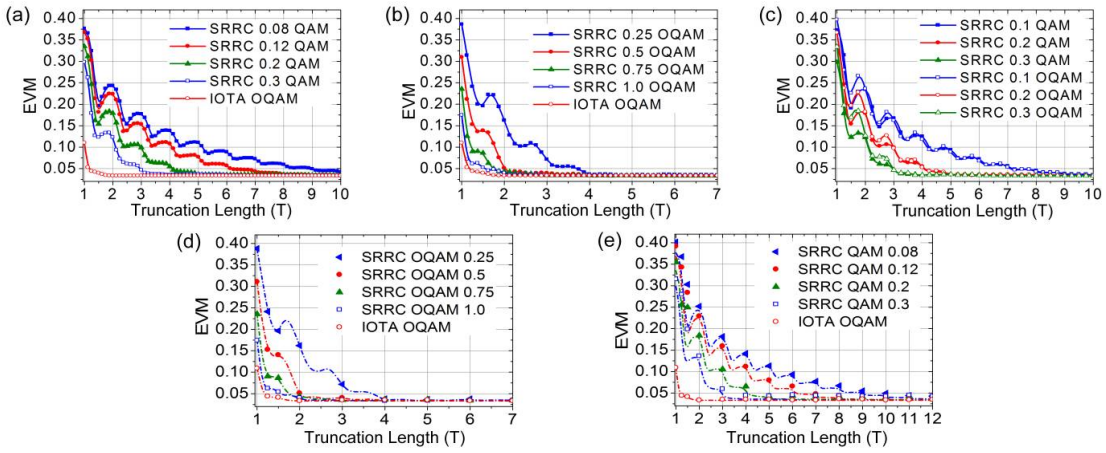

Figure 31. EVM as functions of truncation length: (a)–(c) simulated results and (d)–(e) experimental results.

From both simulated and experimental results, it is demonstrated that IOTA-OQAM and slow-decaying SRRC-OQAM CAP are spectral efficient and insensitive to truncation effects. Given the same EVM performance, they require much shorter truncation length with less number of filter taps than traditional SRRC-QAM CAP scheme. To guarantee an EVM of 0.05, in comparison with SRRC-QAM CAP ($\beta = 0.2$), SRRC-OQAM CAP with

$\beta = 1.0$ and IOTA-OQAM CAP can reduce the number of filter taps by 58.8% and 70.6%, thus leading to 2.4-fold and 3.4-fold increases respectively in digital-filtering CE which is inversely proportional to the size of the digital filters. Furthermore, there is a trade-off between SE and CE under different roll-off factor β. Each CAP band could become narrower with a smaller β at the expense of more filter taps as well as higher computational complexity. Typically, IOTA-OQAM CAP has the highest CE but less SE than SRRC-OQAM CAP. Furthermore, in real systems, it could be possible to adjust the roll-off factor and truncation length of the digital filters in a software-defined network to optimize the throughput, system delay, and power consumption considering different time, services, and users.

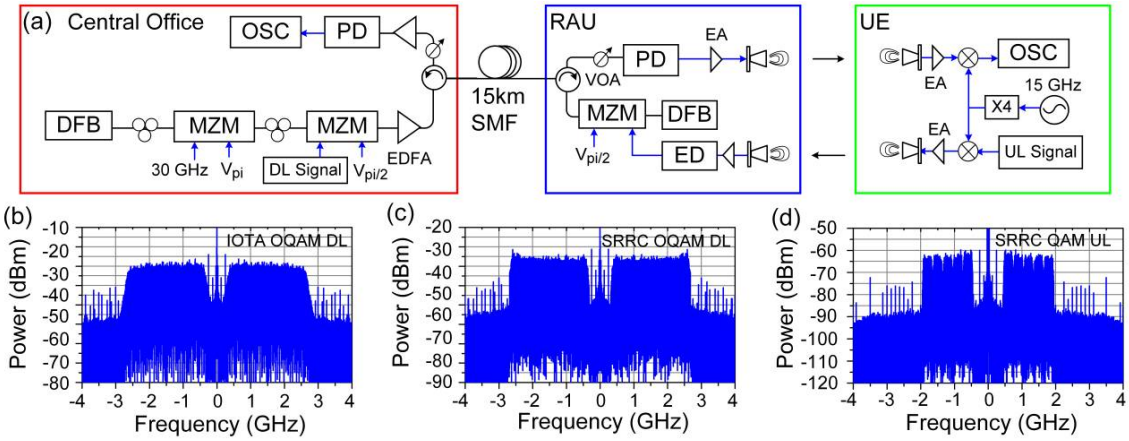

Figure 32. (a) Bidirectional RoF transmission experimental set-up. (b)–(d) Electrical spectra of IOTA-OQAM CAP for DL, SRRC-OQAM CAP for DL, and SRRC-QAM CAP for UL respectively.

3.4 Bidirectional Transmission Experimental Setup and Results

Figure 32(a) shows the proof-of-concept RoF testbed to demonstrate the bidirectional transmission performance of the proposed modulation formats. The testbed is composed of one CO, one RAU, and one user equipment (UE) terminal. It is assumed that high

performance digital signal processors and computing machines are located at the CO site, which is able to generate large-bandwidth, synchronized multi-band CAP signals. Thus IOTA-OQAM and SRRC-OQAM CAP signals could be used in DL because they are more spectral and computational efficient meanwhile requiring strict synchronization between adjacent bands. On the other hand, since there is no overlap between adjacent channels in SRRC-QAM CAP, different users using different bands do not need strict synchronization which makes it a qualified candidate for UL transmission in this experiment.

The roll-off factors are set to be 0.5 and 0.2 for SRRC-OQAM and SRRC-QAM CAP modulations respectively and the truncation lengths are $2T$, $4T$, and $8T$ for scenarios of IOTA-OQAM, SRRC-OQAM, and SRRC-QAM CAP respectively. IM/DD scheme is applied in both DL and UL transmissions as shown in Figure 32(a). For the DL part, one DFB laser working at 1550.1 nm is used as the light source. A 40-GHz MZM biased at the minimum intensity-output point is used to suppress the central optical carrier. Two optical side bands with 60-GHz separation are preserved. Nine OQAM CAP channels with center frequencies at 0.5, 0.75, 1.0, 1.25, 1.5, 1.75, 2, 2.25, and 2.5 GHz are generated and sent to Tektronix 7122C arbitrary waveform generator (AWG) with a sampling rate of 8 GSa/s and symbol duration T_S of 4 ns. An intensity modulator is used to modulate the signals onto the light. An erbium-doped fiber amplifier (EDFA) is used to boost the optical power thus compensating the transmission loss. After 15-km SSMF transmission, the optical MMW signals are detected by a U2T 70-GHz photodetector (PD). A pair of horn antennas with 25-dBi gains is used to deliver and receive the MMW signals. The wireless transmission distance from the RAU to the UE terminal is set to be 1.5 m. Within the UE terminal, a MMW mixer is used to down-convert the signals before they are received by a digital scope

and processed offline. The received electrical spectra of IOTA-OQAM and SRRC-OQAM CAP are shown in Figure 32(b) and (c) respectively. Pre-equalization is applied to compensate the chromatic dispersion induced power fading after fiber transmission.

The UL transmission is initiated by up-converting the baseband SRRC-QAM CAP signals onto the MMW with a 60-GHz local oscillator (LO). A pair of horn antennas is also set up to transmit and receive the 60-GHz signals over 1.5-m wireless channel. It is worth noting that, limited by the response bandwidth of the envelop detector (ED), only five CAP bands are generated for UL transmission with central frequencies at 0.6, 0.9, 1.2, 1.5, and 1.8 GHz. After down-converted by the ED, the signals are amplified and then modulated onto the light by a 10-GHz intensity modulator. After 15-km SSMF transmission, the signals are detected by a 10-GHz PD and demodulated offline. The electrical spectrum of the UL SRRC-QAM CAP signal is shown in Figure 32(d).

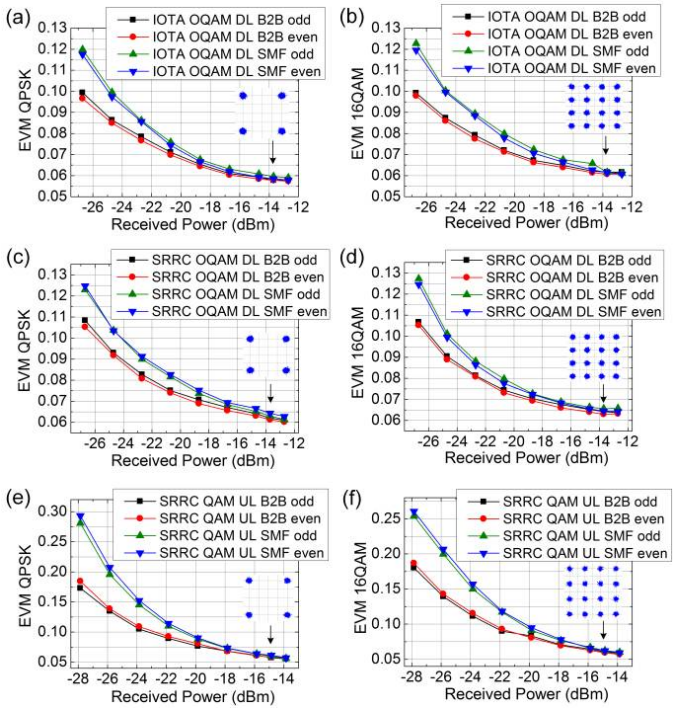

Figure 33. Measured EVM versus received optical power for odd and even channels in: (a)–(b) DL IOTA-OQAM CAP; (c)–(d) DL SRRC-OQAM CAP; and (e)–(f) UL SRRC-QAM CAP.

QPSK and 16QAM modulation formats are applied in both DL and UL with their EVM performance shown in Figure 33(a) to (f). For all the cases, clear constellations with less than 7% EVM can be achieved. In DL scenarios, less than 8% EVM can be obtained with received optical power of -22 dBm and -20 dBm with and without 15-km fiber transmission respectively. In UL transmission, the power thresholds to achieve 8% EVM are around -21 dBm and -19 dBm with and without fiber transmission respectively. The 2-dB power penalties are mainly induced by propagation attenuation and chromatic dispersion induced phase mismatch between the 60-GHz-separated optical two tones. The EVM differences between DL and UL may be resulted from the different sensitivities of the PDs and different noise figures and nonlinearities of the electrical amplifiers.

3.5 High-Capacity Tier-II Fronthaul Network with SSB-DD Multiband OQAM/QAM-CAP

3.5.1 Motivation and Backgrounds

The explosive growth of massive connectivity and traffic throughput in 5G wireless poses a great challenge for developing next-generation mobile fronthaul (MFH) networks. Moreover, recent progresses in functional-split [72] and mobile edge computing [88] may bring revolutionary changes which force us to rethink about today's MFH technology. To reduce the latency and make fast response to delay sensitive services, mobile-edge-computing (MEC) enhanced distributed units (DU) are introduced between central unit (CU) and remote radio systems (RRS) [72], which greatly increases the data traffic in tier-II fronthaul network as shown in Figure 34. Even with functional-split, more than 100-Gb/s MFH technology is still in an urgent need to support 10-100 times increase in future wireless throughput.

Recently multiband CAP modulation draws attention from researchers for its good transmission performance and better flexibility comparable to PAM-4. The bit/power-loading algorithm is simpler than discrete multi-tone (DMT), which needs to adjust every subcarrier. 107.5-Gb/s multiband CAP over multi-mode fiber with VCSEL is proposed [89] but the distance is limited to 100 m. 4×100-Gb/s WDM based multiband CAP systems are also reported [47], [79]. However, the bandwidth and transmission distance are limited by intensity-modulation and direct-detection (IM-DD) scheme. Moreover, the spectral efficiencies (SE) of the above QAM based CAP systems are reduced by a factor of $1/(1+\beta)$, where β is the roll-off factor. They are also vulnerable to truncation effect thus

requiring a large number of filter taps which complicates the DSP [68]. On the other hand, off-set QAM (OQAM) multiband modulation attracts academic interests recently. OQAM allows adjacent channels to be overlapped without interference, which avoids roll-off factor induced reduction in SE. The orthogonal condition of matched filtering is also relaxed which allows using filters with larger roll-off factors and less number of taps [68].

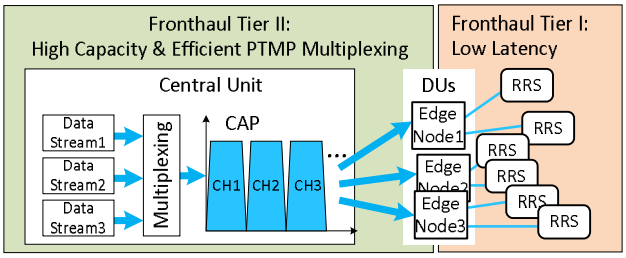

Figure 34. Architecture of proposed mobile fronthaul system. DU: distributed unit; RRS: remote radio system.

In this section, we demonstrate a 20/80-km 128-Gb/s MFH system as a high capacity data link between CU and DUs based on single-side-band and direct-detection (SSB-DD) OQAM-CAP. Compared with traditional QAM-CAP, higher SE and better transmission performance are obtained. The required number of filter taps is also reduced by 50%.

3.5.2 Operation Principle

The conceptual diagram of the proposed MFH is shown in Figure 34. Edge computing is a promising technique enhancing 5G MFH [88]. By penetrating computing resource at DUs closer towards users, the processing delay can be reduced and meanwhile high-speed data links as Tier-II MFH connecting CU and DUs are needed. At the CU, data streams are generated and multiplexed to corresponding CAP bands allocated for different edge nodes. By utilizing CAP, the complex dynamic timing slot allocation among nodes in a traditional TDM system is eliminated, which further reduces the latency.

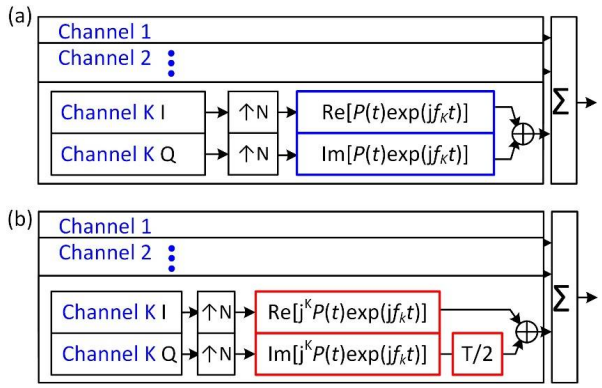

Figure 35. Transmitter DSP blocks of (a) QAM- and (b) OQAM-CAP.

The transmitter DSP stacks of QAM- and OQAM-CAP are shown in Figure 35(a) and (b) respectively. The QAM-CAP is initiated with mapping the PRBS streams into QAM symbols. After over-sampling, the samples are convoluted with the digital filter pairs. Then signals from different I/Q branches are combined and sent to the digital-to-analog converters (DACs). For OQAM-CAP multiband, the algorithm process is similar to that of QAM-CAP. It is worth noting that a periodic half-π phase shift factor is multiplied with the intermediate-frequency (IF) carriers and a half-symbol duration timing offset is introduced between the I and Q components for OQAM signals. The order of the receiving DSP stacks is reversed compared with transmitter parts where a pair of matched filters is applied before down-sampling and QAM de-mapping.

The electrical spectra of 8-band QAM- and OQAM-CAP signals are compared in Figure 36(a) and (b) respectively. The aggregated baud rate is 32 GHz with 4-GHz baud rate for each band. An over sampling rate, N_{ov}, of 10 is applied for both modulation formats. In traditional QAM-CAP multiband, square-root-raised-cosine (SRRC) filters are applied with a roll-off factor β of 0.15. Every two bands are isolated with each other and an excess bandwidth of 0.15×4=0.6 GHz is wasted in each channel. To suppress the out-

of-band-leakage (OOBL) noise 50 dB below the average signal power, $2\times6\times N_{ov}$ FIR taps are used in digital filtering. Compared with QAM-CAP, OQAM-CAP allows the channels to be aggregated at the Nyquist limit with some overlap. As shown in Figure 36(b) SRRC filters with $\beta = 0.5$ are applied and the separation between the adjacent channels is 4 GHz with a 2-GHz aliasing in each channel. However, although there is an overlapping, the signal of each channel can still be recovered without interference because of the orthogonal property of OQAM precoding [68]. $2\times3\times N_{ov}$ filter taps are used in OQAM-CAP channels to obtain the same OOBL noise floor compared with QAM-CAP. Since the number of multiplication in digital filtering is proportional to the filter length, OQAM-CAP could obtain 50% improvement in computational efficiency (CE).

3.5.3 Experimental Results and Discussions

Figure 37 shows the experimental test bed of the proposed high-capacity MFH based on OQAM/QAM-CAP. Light emitted out from a C-band external cavity laser (ECL) enters a dual-arm Mach-Zehnder modulator (DA-MZM) biased at $V_{\pi/2}$. The generation of the SSB signals is based on DA-MZM with small-driving-signal operation [90]. The original double side band (DSB) signal and its Hilbert transform are used as in-phase and quadrature components feeding into the two signal ports of DA-MZM. Under small signal, DA-MZM can be approximated as an IQ modulator. However, compared with the complex bias configurations and packaging of the IQ modulator, DA-MZM provides a low-cost alternative option. The 32-Gbaud eight-channel CAP16 signals are generated by DACs operated at 80 GSa/s and attenuated by a pair of 10-dB electrical attenuators after amplification. After modulation, the signal light is boosted by an erbium-doped fiber

amplifier (EDFA) and transmitted over 80-km standard single mode fiber (SSMF). At the DU site, another EDFA is used to compensate the transmission loss. The signal is received by a 50-GHz U2T photo detector (PD) and recorded by a Lecroy 120-GSa/s oscilloscope. The optical spectra of the DSB and SSB signals are shown in the inset of Figure 37. More than 10-dB sideband suppression ratio can be obtained.

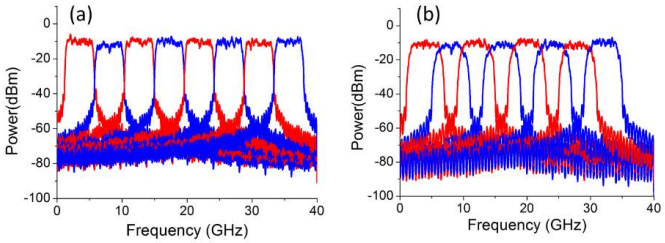

Figure 36. Electrical spectra of (a) QAM- and (b) OQAM-CAP.

One important issue in direct-detection single sideband modulation is the signal-to-signal beating interference (SSBI), which is mainly caused by unwanted mixing products after square-law detection of PD. SSBI typically distributes from DC to several times of the signal bandwidth, which can hardly be eliminated by pre- or post-equalization. Traditional optical or DSP based schemes significantly increase the complexity in hardware or computing. In this paper, we propose to combine pre-equalization and minimum bit-error-rate (BER) power loading [91] to mitigate SSBI and optimize the BER distribution. Given the *i*th channel response, H_i, noise distribution coefficient, γ_i, and modulation format dependent factor, K_M, the power partition coefficient of each channel can be deducted as

$$\mu_i = \frac{b_i}{1+b_i^2}\left(\sum_{n=1}^{N}\frac{b_n}{1+b_n^2}\right)^{-1} \tag{3.18}$$

where $b_i = \left|H_n{}^2\right| K_M \gamma_i$. Compared with DMT, such power adjustments are performed among a few bands instead of thousands of subcarriers, which is computational efficient. The received back-to-back electrical spectra of the OQAM- and QAM-CAP signals are shown in Figure 38(a)-(c) and Figure 38(d) respectively. The BER distributions of each channel in OQAM-CAP without pre-equalization, with pre-equalization, and with pre-equalization plus power loading are shown in Figure 38(a). It is noticed that, although pre-equalization significantly improves the flatness of the signal spectrum and reduces the total BER. But the signal quality of the low-frequency bands is still deteriorated due to the SSBI. However, when power loading algorithm is used after the pre-equalization, more power is allocated to the bands which suffer more from the SSBI. The BER performance among different bands can be re-balanced and the total BER is minimized.

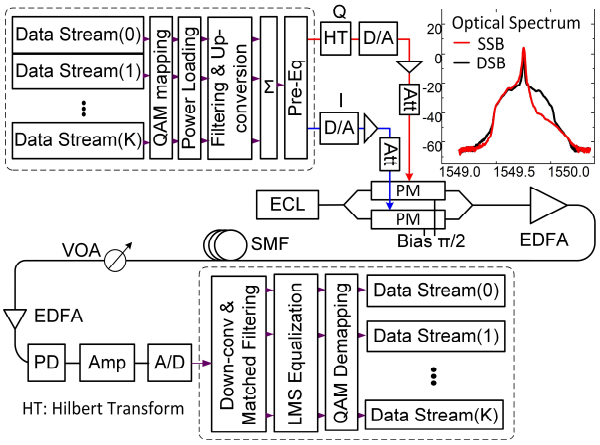

Figure 37. System diagram of the experimental testbed.

The total BER performance as a function of optical-signal-to-noise ratio (OSNR) under B2B operation and BER versus launch power after fiber transmissions are shown in Figure 39(b) and (c) respectively. As shown in Figure 39(b), for all the cases, the BER is remarkably improved when power loading is applied, which is matched with the results

shown in Figure 39(a). With a 20% SD-FEC threshold of 2E-2, a 4-dB OSNR penalty is observed when power loaded QAM-CAP16 is used instead of OQAM-CAP16, which is caused by a larger effective bandwidth occupied by QAM-CAP. Since the system is operated under greatly attenuated electrical signals with a small modulation depth, the real electrical SNR could be much smaller than OSNR. As shown in Figure 39(c), there is around 11-dB power difference between using 20-km and 80-km fiber, which is mainly attributed to increased transmission loss of longer distance. The selected constellations with BERs less than 7% HD-FEC threshold of 3.8E-3 are also shown in the inset of Figure 39(b) and (c). It is observed that OQAM-CAP and power loading technique can bring about 4-dB and 3-dB launch-power improvements respectively which demonstrates the superiority of the proposed MFH with power loaded OQAM-CAP compared to the scheme using traditional CAP.

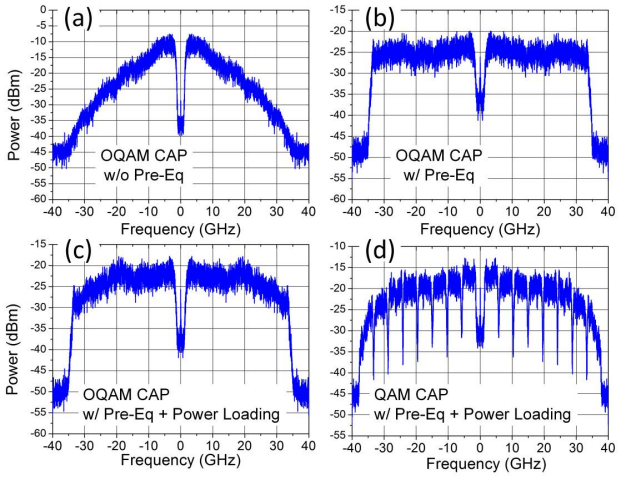

Figure 38. Selected electrical spectra: (a) – (c): OQAM- CAP; and (d) QAM-CAP.

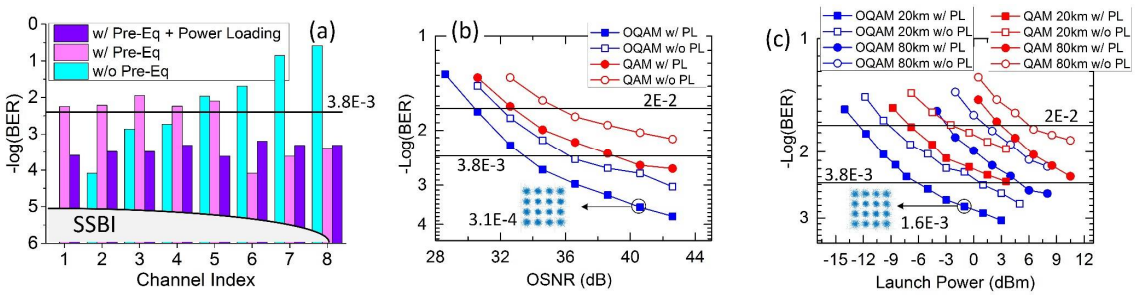

Figure 39. (a) BER distribution among channels; (b) BER versus OSNR; and (c) BER versus launch power

3.6 Summary

In summary, we have demonstrated, for the first time, a multiband OQAM CAP modulation with advanced digital filter design in a spectral efficient fiber-wireless integrated RoF system for applications with multiband, multiservice, and multiuser. The operation principles of OQAM and OQAM-CAP as well as the generation of IOTA filters are introduced. Truncation effect and its influence on digital filters are also theoretically analyzed. Three scenarios are studied and compared in this paper, namely, the IOTA-OQAM CAP, SRRC-OQAM CAP, and SRRC-QAM CAP. From both the simulation and experimental results, it is demonstrated that IOTA/SRRC-OQAM CAP can achieve around 10% improvement in SE and about 2 to 4-fold increase in CE compared with traditional SRRC-QAM CAP. For SRRC-OQAM/QAM CAP, there is a trade-off between SE and CE by applying different roll-off factors. Nevertheless, IOTA filtered OQAM CAP has the highest resistance to truncation effect thus being able to obtain the highest CE among all the three cases. On the other hand, SRRC-QAM CAP can still be a promising candidate for RoF UL transmission because it does not require strict synchronization between the adjacent channels. Bidirectional 60-GHz RoF transmission experiments are conducted over

15-km-SSMF and 1.5-m-wireless channels with IOTA/SRRC-OQAM CAP for DL and SRRC-QAM CAP for UL. Less than 7% EVM can be achieved for both QPSK and 16QAM modulations with the maxima DL and UL data rates of 9 Gbit/s and 5 Gbit/s respectively.

On the other hand, we demonstrate a 128-Gbit/s multi-band OQAM-CAP16 based Tier-II fronthaul data link supporting high-capacity mobile edge nodes in 5G. Compared with QAM-CAP, OQAM-CAP allows overlap between channels and relaxes the requirement on the number of filter taps thus obtaining around 8% and 50% improvements in spectral and computing efficiencies respectively. On the other hand, longer transmission distance and optimized BER performance are achieved by utilizing SSB modulation with power loading over multiple CAP bands.

CHAPTER 4. SIGNAL DETECTION AND PROCESSING IN BIDIRECTIONAL ANALOG RADIO-OVER-FIBER MOBILE FRONTHAUL NETWORKS

4.1 Introduction

Empowered by spectral aggregation and cell densification, future 5G mobile data network poses a huge challenge to build next generation mobile fronthaul system with higher capacity, scalability, and energy efficiency. Under this circumstance, traditional solutions based on common public radio interface (CPRI) or channel aggregation with digital signal processing (DSP) are not sufficient to support heterogeneous ubiquitous wireless access. In this paper, we demonstrate a point-to-multi-point bidirectional mobile fronthaul system. Wavelength division multiplexing plus frequency division multiplexing (WDM-FDM) is applied to support independent asynchronous small cells. Intensity-modulation and direct-detection (IM-DD) downlink (DL) as well as filed-modulation and heterodyne-detection (FM-HD) uplink (UL) are proposed. Combined with efficient virtual tone based DSP for phase recovery and carrier-frequency-offset estimation, signal degradations from beating among incoherent asynchronous UL signals are mitigated. Proof-of-concept experiments are demonstrated where 20 and 16 80-MHz component carriers (CCs) are transmitted over 25-km standard single mode fiber (SSMF) for DL and UL respectively. Less than 6% error vector magnitudes (EVMs) with 64, 16, and 4-ary quadrature amplitude modulation (QAM) are obtained.

4.2 Operation Principles and Impairment Analysis in Bidirectional Mobile Fronthaul Network

As mentioned in the previous sections, the transmission impairments in the FDM upstream is mainly caused by incoherent signals from different cells and their beating inside the PD. In the following parts, we are going to analyze the impairments in three UL schemes. The first scheme applies distributed directly modulated lasers (DMLs) which is widely used today's TDM-PON and hybrid fiber-coaxial (HFC) systems. As shown in Figure 40(a), two DMLs are implemented in two small cells. Signals from Small Cell 1 and Small Cell 2 occupy odd and even channels respectively which will be combined using a passive splitter and received by a PD at the BBU-Pool. The electric field of the output light from the DML can be represented by

$$E(t) = |E(t)|e^{j(\omega t+\phi)} = A[1+\alpha s(t)]e^{j(\omega t+\phi)} \tag{4.1}$$

where ω and ϕ are the angular frequencies and phase of the light, while A, α, and $s(t)$ are the amplitude, modulation index, and modulated electrical signals respectively. After combination, the total electric field can be expressed as the sum of electric fields from two cells as

$$\begin{aligned} E_{tot} &= E_1(t) + E_2(t) \\ &= A_1[1+\alpha_1 s_1(t)]e^{j(\omega_1 t+\phi_1)} + A_2[1+\alpha_2 s_2(t)]e^{j(\omega_2 t+\phi_2)}. \end{aligned} \tag{4.2}$$

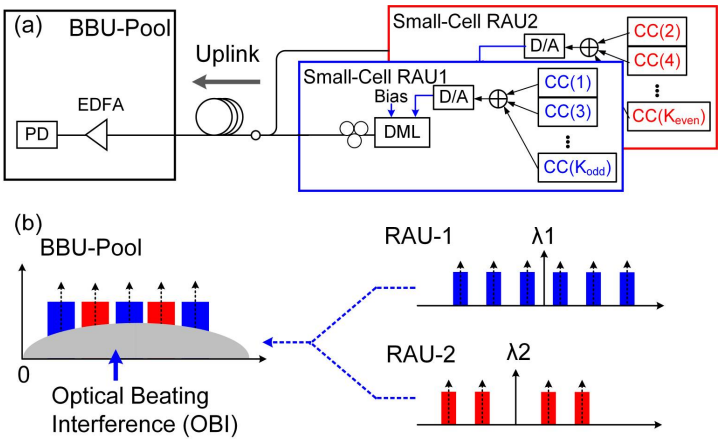

Figure 40. Mobile fronthaul uplink using distributed directly modulated lasers (DMLs): (a) system diagram; (b) resulted signal impairments.

After PD, the photocurrent I will follow the square-law detection principle which is evaluated as

$$\begin{aligned} I &\propto E_{tot} \cdot E_{tot}^{*} \\ &= A_1^2\left[1+\alpha_1 s_1(t)\right]^2 + A_2^2\left[1+\alpha_2 s_2(t)\right]^2 \\ &\quad +2A_1A_2\left[1+\alpha_1 s_1(t)\right]\left[1+\alpha_2 s_2(t)\right]\cos\left[(\omega_1-\omega_2)t+(\phi_1-\phi_2)\right], \end{aligned} \tag{4.3}$$

where $s_1(t)$ and $s_2(t)$ occupy odd and even channels and they fulfill $|\alpha_1 s_1(t)| \ll 1$ and $|\alpha_2 s_2(t)| \ll 1$ respectively, when the modulator is operated under linear region. Thus Equation (4.2) can be further simplified as

$$\begin{aligned} I \propto\ & 2\left[\alpha_1 A_1^2 s_1(t) + \alpha_2 A_2^2 s_2(t)\right] + (A_1^2 + A_2^2) \\ & +2A_1A_2\left[1+\alpha_1 s_1(t) + \alpha_2 s_2(t)\right]\cos(\Delta\omega t + \Delta\phi), \end{aligned} \tag{4.4}$$

where $\Delta\omega = \omega_1 - \omega_2$ and $\Delta\phi = \phi_1 - \phi_2$, and they are both functions of time t. The first term in Equation (4.4) is the desired signals after combination from the two cells. The second term is the direct current (DC) component. And the last term is the OBI which could be complicated if free-running lasers are used. Typically, the wavelengths of DMLs are

unstable and keep drifting even with thermal controllers. Thus, the angular-frequency-difference $\Delta\omega$ is unpredictable and sometimes could change drastically. If it is reduced to zero, OBI will be overlapped with the desired signal and seriously degrade the signal-to-interference-plus-noise ratio (SINR) as shown in Figure 40(b).

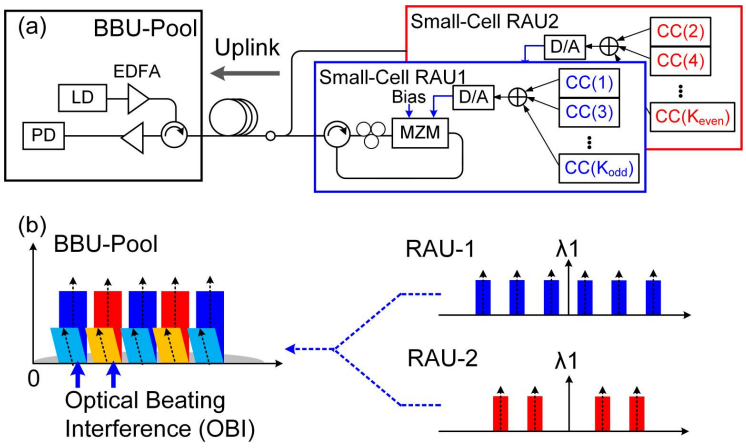

Figure 41. Mobile fronthaul uplink using distributed remote modulators: (a) system diagram; (b) resulted signal impairments.

The second scheme is to use centralized light source and distributed remote modulators as shown in Figure 41(a). In the short-reach mobile fronthaul network, DMLs can be replaced with source-free modulators, e. g., Mach-Zehnder modulators (MZMs) and the input lights for multiple small cells are provided by a centralized laser source at the BBU-Pool. To further improve the signal quality and reduce the phase noise, an external cavity laser (ECL) with laser linewidth around 100 KHz can be applied. In this case, the wavelengths from different cells will be locked with $\Delta\omega = 0$. Suppose that MZMs with push-pull operations are used; the output electric field of an MZM can be modeled as

$$E_{out} = \left|E_{in}\right| e^{j(\omega t+\phi)} \cos\left[\frac{\pi}{2V_{\pi}}(V_{bias} + s(t))\right], \tag{4.5}$$

where E_{out} and E_{in} are the output and input electric fields of the light respectively; V_π is the half-wave voltage of the MZM; and V_{bias} is the applied bias voltage. To achieve the best intensity-modulation performance, the MZM is biased at $V_{bias} = V_\pi/2$ and thus Equation (4.5) can be rearranged as

$$E_{out} = |E_{in}| e^{j(\omega t+\phi)} \cos\left[\frac{\pi}{4} + \frac{\pi}{2V_\pi} s(t)\right]. \tag{4.6}$$

At linear operation region when $|s(t)| \ll V_\pi$, Equation (4.6) can be approximated as

$$E_{out} = A\left[1+\alpha s(t)\right] e^{j(\omega t+\phi)}, \tag{4.7}$$

where $A = \sqrt{2}|E_{in}|/2$ and $\alpha = -\pi/(2V_\pi)$. It is worth nothing that Equation (4.7) is in the same form compared with Equation (4.1). Thus, after combination and photo-detection, if small nonlinear components are ignored, the photocurrent becomes similar to Equation (4.4), which is expressed as

$$\begin{aligned} I \propto\ & 2\left[\alpha_1 A_1^{\,2} s_1(t) + \alpha_2 A_2^{\,2} s_2(t)\right] + (A_1^{\,2} + A_2^{\,2}) \\ & + 2A_1 A_2 \left[1 + \alpha_1 s_1(t) + \alpha_2 s_2(t)\right] \cos(\Delta\phi), \end{aligned} \tag{4.8}$$

As indicated by Equation (4.8), although, the impact of wavelength thermal drift is eliminated, the OBI issues mainly induced by the beating among signals from various cells are not resolved as shown in Figure 41(b). The phase noise generated with incoherent light sources in different RAUs will convert into intensity noises which severely pollute the signals even when DSP technique is applied.

In the aforementioned schemes, it is noticed that due to the OBI and phase incoherency, FDM signals are challenging to be recovered through traditional intensity-modulation and direct-detection (IM-DD) systems. In order to resolve such an issue, we propose a field-modulation and heterodyne-detection (FM-HD) scheme based on aforementioned remote-modulator system for the UL transmission. As shown in Figure 42(a), the UL signals are photo-detected with an optical local oscillator (LO) in the BBU-Pool. The wavelength of the optical LO is not overlapped with the optical carrier modulated with signals. To optimize the field modulation performance in RAUs, the MZMs are biased at V_π. Then the electric field of the modulator output light can be expressed as

$$E_{out} = -\left|E_{in}\right| e^{j(\omega t+\phi)} \sin\left[\frac{\pi}{2V_\pi} s(t)\right]. \tag{4.9}$$

With the given small signal modulation condition for best modulation linearity, $|s(t)| \ll V_\pi$, Equation (4.9) is simplified as

$$E_{out} \approx \alpha A s(t) e^{j(\omega t+\phi)}, \tag{4.10}$$

where $\alpha = -\pi/(2V_\pi)$ and $A = |E_{in}|$. After incorporating the signal lights from Small-Cell 1 and Small-Cell 2 as well as the optical LO, the total electric field can be derived as

$$E_{out} = \alpha_1 A_1 s_1(t) e^{j(\omega_1 t+\phi_1)} + \alpha_2 A_2 s_2(t) e^{j(\omega_1 t+\phi_2)} + A_L e^{j(\omega_L t+\phi_L)}, \tag{4.11}$$

where A_L, ω_L, and ϕ_L are the amplitude, angular frequency, and phase of the LO light. After beating inside the PD, the photocurrent can be obtained as

$$
\begin{aligned}
I \propto\ & E_{tot} \cdot E_{tot}{}^{*} \\
=\ & 2\alpha_1 A_1 A_L s_1(t)\cos\left[\omega_{IF}t + \Delta\phi_{L1}\right] \\
& +2\alpha_2 A_2 A_L s_2(t)\cos\left[\omega_{IF}t + \Delta\phi_{L2}\right] \\
& +2\alpha_1\alpha_2 A_1 A_2 s_1(t)s_2(t)\cos(\Delta\phi_{12}) \\
& +\alpha_1{}^2 A_1{}^2 s_1(t)^2 + \alpha_2{}^2 A_2{}^2 s_2(t)^2 + A_L{}^2,
\end{aligned}
\tag{4.12}
$$

where $\omega_{IF} = \omega_L - \omega_1$, $\Delta\phi_{L1} = \phi_L - \phi_1$, $\Delta\phi_{L2} = \phi_L - \phi_2$, and $\Delta\phi_{12} = \phi_1 - \phi_2$. The first two terms of Equation (4.12) are the desired signals from two cells after combination and the last four terms are the undesired OBI components. As shown in Figure 42(b), the optical LO provides a reference for asynchronous signals from different cells. After beating inside the PD, signals will be up-converted to an intermediate frequency (IF) located at ω_{IF} and OBI terms are mainly distributed on the low-frequency band. By properly choose the wavelength of the LO, signals carried by the IF will not be interfered by the OBI components as shown in Figure 42(b). Moreover under heterodyne detection, instead of converting into the intensity noise, the phase noises can be reconstructed by tracking the phase fluctuations of the IF or pilot tones which enables us to use specific DSP techniques to rectify the phase of the vector signals. Therefore by using FM-HD method, the OBIs and phase noises are largely mitigated. All the devices for UL transmission remain identical to that of traditional IM-DD schemes except only a low-cost distributed feedback (DFB) laser implementing as the optical LO in the BBU-Pool. Therefore, the proposed UL receiving systems have relatively simple structures as well as improved stability and affordability. It could be a promising candidate to realize bidirectional WDM-FDM mobile fronthaul supporting future 5G system with spectral aggregation and cell densification.

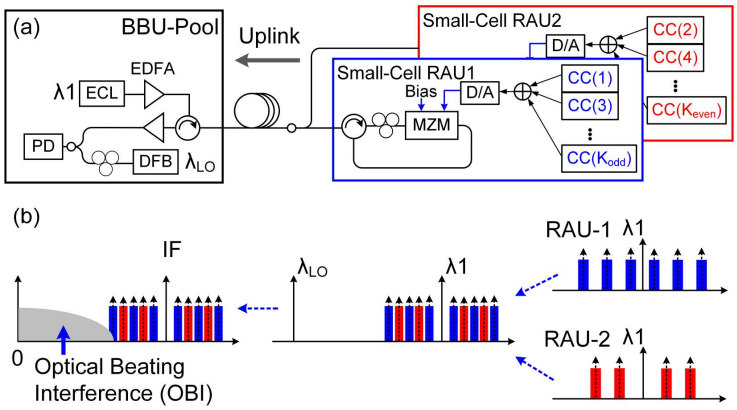

Figure 42. System diagram (a) and signal flow (b) of proposed mobile fronthaul uplink with field-modulation and heterodyne-detection scheme.

4.3 Experimental Demonstration and Results

A proof-of-concept experimental test bed of the proposed bidirectional mobile fronthaul is shown in Figure 15(a). The test bed is set up to study the operation of one WDM-channel in the proposed WDM-FDM mobile fronthaul network. A pair of coarse WDM (CWDM) multiplexers is used to separate DL and UL wavelengths. The DL system is based on conventional IM-DD scheme, where electrical signals are modulated onto the light through an MZM which is under push-pull operation and biased at $V_\pi/2$. Twenty 80-MHz aggregated CCs are transmitted from the BBU-Pool to two independent small-cell RAUs over 25-km SSMF. At the RAU sites, the optical signals will be directly detected by the PD and recovered with offline DSP. In the experiment, one CC contains 1024 subcarriers and it is used to imitate a future 5G signal band. Small Cell 1 and Small Cell 2 selectively receive odd and even CCs respectively. The electrical spectrum of the DL signal received at Small Cell 1 is shown in Figure 15(e).

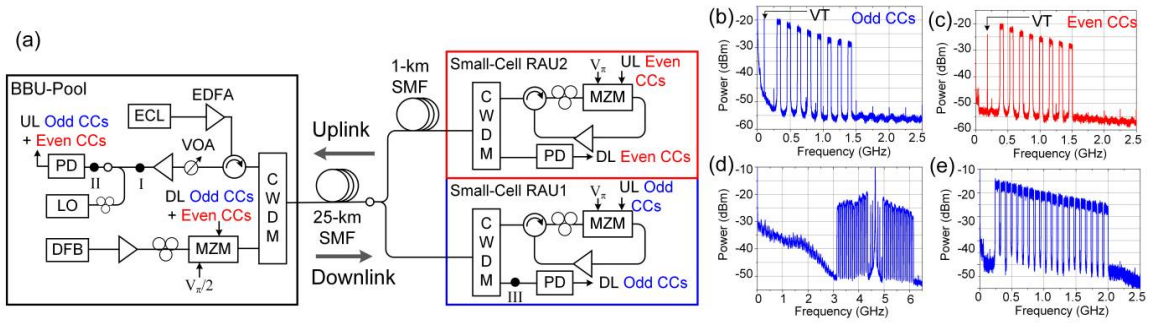

Figure 43. Bidirectional experimental demonstration of proposed mobile fronthaul system: (a) test-bed diagram; (b)-(c) odd- and even-channel electrical spectra after square-law detection at Point I respectively; (d)-(e) electrical spectra after square-law detection at Point II and III respectively.

The UL transmission system is based on aforementioned FM-HD scheme. The light from one ECL at the BBU-Pool is boosted by an erbium-doped-fiber amplifier (EDFA) before fed into two small-cell RAUs. At each RAU site, a polarization controller (PC) is used to adjust the polarization state of the light to maximize the modulation depth. As noted, the UL light is field modulated by an MZM biased at V_π. The UL signal is composed of 16 80-MHz LTE-like CCs, while the odd CCs are modulated onto the light in RAU1 and the remaining even CCs are modulated onto the light in RAU2 to imitate the FDM operations among the two cells, which are shown in Figure 43(b) and (c) respectively. The lights carrying different FDM signals are then combined and transmitted back to the BBU-Pool after 25-km SSMF. At the BBU-Pool, the signals mixing with the optical LO are detected with a single-end PD. It is worth nothing that a 1-km SSMF segment is added before RAU2 to de-correlate the lights entering two different cells. Since all the laser sources are centralized, the BBU-Pool is able to precisely control and adjust the wavelength of the ECL and DFB, where system controlling and maintenance efficiency are largely enhanced. The electrical spectrum of the received UL signals is shown in Figure 43(d). The signals are up-converted to the IF at 4.7 GHz generated from the beating between the

signal- and LO-lights. In this case, the signals are totally immune from the undesired OBI components which occupy the low-frequency band from 0 to 3 GHz.

To improve the quality and successfully recover the UL FDM signals. Two technical issues need to be addressed. First, the remote MZMs at the RAUs need to be biased at V_π. Figure 44(a) shows the power and electric-field responses of the MZM when it is biased at $V_\pi/2$ and V_π. The signal spectra at different cases are also compared in Figure 44(b) and (c). Traditionally, in intensity-modulation scheme, MZM is biased at $V_\pi/2$ to achieve the best linearity in its power response expressed as

$$\frac{|I_{out}|}{|I_{in}|} \propto \frac{1}{2}\left[\cos\left(\frac{\pi}{V_\pi}(V_{bias}+s(t))\right)+1\right] \tag{4.13}$$

However, as indicated in Equation (4.12), in FM-HD, system detects the electric field of the signal instead of its power and the field response is given by

$$\frac{|E_{out}|}{|E_{in}|} \propto \cos\left(\frac{\pi}{2V_\pi}(V_{bias}+s(t))\right) \tag{4.14}$$

where the best linearity occurs at $V_{bias} = V_\pi$. As shown in Figure 44(b), when the bias is close to $V_\pi/2$, the electric field is nonlinearly distorted, and the low-frequency OBI grows up which competes against the desired signals and consumes the gain inside the PD and amplifiers resulting in a reduced SINR of desired signals. On the other hand, at the bias of V_π, the OBI will be suppressed. Second, the phase noises after heterodyne detection need to be exactly eliminated. In this work, we apply virtual tone (VT) based DSP for phase recovery [92]. A VT is an OFDM pilot subcarrier carrying known pre-coded symbols which is inserted near the data-loaded subcarriers as shown in Figure 44(b) and (c). Such VTs are allocated at different frequencies for different cells. After fiber transmission, the

bundled signals and VT from one cell suffer from the same phase noise and carrier frequency offset (CFO). At the UL receiver site, the VT can be extracted to cancel out the same phase noise and CFO carried by the paired OFDM signals. This method is proved to be an effective solution to overcome the phase incoherency among asynchronous cells although it sacrifices a part of the spectral efficiency.

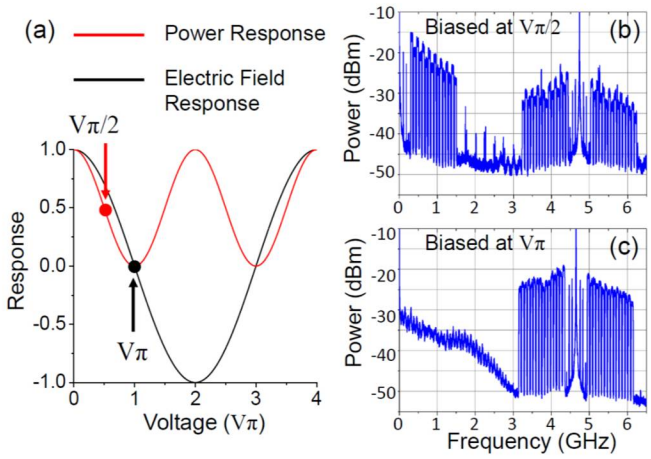

Figure 44. (a) Power and electric-field responses of a Mach-Zehnder modulator. (b)-(c) Electrical spectra after heterodyne detection when the MZM is biased at $V_\pi/2$ and V_π respectively.

The experimentally measured constellation diagrams and error-vector magnitudes (EVMs) versus received power are shown in Figure 45. In the experiment, three modulation formats, QPSK, 16QAM, and 64QAM are applied with the results illustrated in Figure 45(a, d), 16(b, e), and 16(c, f) respectively. For all DL and UL cases, less than 6% EVMs are obtained with and without applying 25-km SSMF, which passes the 8% EVM threshold of 64QAM defined in current LTE standards [93]. The received power penalty with 25-km fiber transmission are attributed to higher insertion loss and chromatic dispersion induced power fading. As shown in Figure 45, the sensitivity with 8%-EVM at the UL receiver end is around -16 dBm. The power of the ECL is boosted to 12 dBm by the EDFA before

launching into the fiber. Another EDFA with a gain of 17 dB is also implemented at the UL receiver site. Given the receiver sensitivity and laser power, the gain of the optical link is enough to support 6 small-cell RAUs and compensate the loss induced by bidirectional 25-km fiber transmission (11 dB), CWDM multiplexers (3 dB), modulators (9 dB), circulators (5 dB), and PCs (0.5 dB). It is worth noting that the EVM performance of the OFDM signal could be further improved by compensating the nonlinear distortion resulted from the electrical amplifications [94].

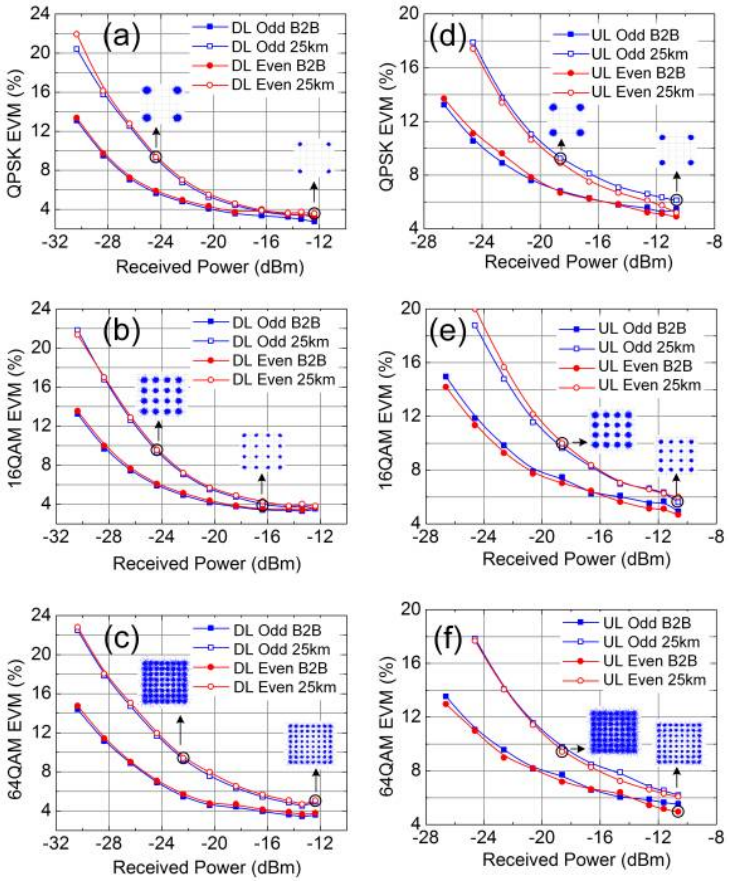

Figure 45. Average error-vector-magnitude (EVM) of aggregated component carriers versus received optical power.

In comparison with the existing schemes, our proposed WDM-FDM based bidirectional mobile fronthaul eliminates the interference from OBI components and thus

achieving better received signal quality. It also exhibits the advantages with high flexibility, enabling PTMP bidirectional transmission, and high capability to support increased number of connected cells. Moreover, FDM data transmission from each cell site doesn't need to wait for a specific time slot, which reduces its latency and synchronization requirements in comparison with TDM schemes. However, on the other hand, there are also some issues which deserve to be further studied and made improvements in the future. Since MZMs are typically polarization sensitive, it requires polarization control and tracking systems at the distributed RAUs which adds to the complexity and cost of the overall network. One possible solution is to apply reflective semiconductor optical amplifiers (RSOAs), electro-absorption modulators (EAMs), or polarization insensitive silicon photonics [95]. Meanwhile, a polarization multiplexed receiver can also be implemented at the BBU-Pool [96]. Moreover, the number of connected cells could be further increased if PDs with higher sensitivities are used.

4.4 Filter-Bank Multi-Carrier in Next-Generation Mobile Fronthaul Networks with Centralized Pre-Equalization

4.4.1 Motivations and Backgrounds

The drastic growth of demands in high quality wireless services has triggered the investigation of fifth generation (5G) mobile data networks, which is commonly forecasted to be deployed around 2020 [1]. To support future 5G mobile communication systems employing millimeter wave (MMW) and small cells, fiber and wireless access networks will be integrated to provide mobile fronthaul (MFH) solutions with higher capacity, flexibility, and spectral efficiency (SE). Compared with traditional MFH networks based

on common public radio interface (CPRI), analog-domain carrier aggregation (CA) [14], [18] and radio-over-fiber (RoF) [97], [98] schemes increase the bandwidth efficiency and reduce the latency. However, except from existing wireless-link penalties, component carriers (CCs) in analog CA and RoF schemes also suffer from power fading, nonlinear distortions, and other signal quality degradations from optical transmitters, receivers, and fiber transmissions, which requires us to enhance the digital-signal-processing (DSP) capabilities of baseband-unit (BBU) pool with pre-distortion, post-compensation, and link adaptation in next-generation fiber-wireless-integrated MFH networks.

On the other hand, fueled by the development and popularity of new technologies such as wireless sensor networks and Internet of Things, massive machine-type communications (MTC) become a key challenge to be addressed in the 5G systems [99]. Different from the traditional human-to-human (HTH) equipment, most MTC devices are inexpensive with limited computational or power resources. To support those devices, one of the solutions is to aggregate high-performance computing machines as well as high speed DSP resources at the BBU pool. In comparison with traditional distributed systems, complex and time-consuming functions like pre-equalization and pre-distortion can be partly or even totally performed at the BBU pool which releases the DSP burden thus reducing the cost on the distributed user terminals. In addition, the centralized processing power also enables more advanced and efficient network coordination and management.

Recent studies about filter-bank multicarrier (FBMC) have been reported in both optical and wireless areas [83], [100]. In comparison with orthogonal frequency division multiplexing (OFDM), FBMC uses proto-type filters to define the time-frequency window of each subcarrier (SC). The undesired sidelobes of SCs can be significantly suppressed,

which enables the system to seamlessly aggregate asynchronous CCs from different users, services, and locations without interference. The above features distinguish FBMC from other multi-carrier formats to support asynchronous centralized signal processing and concurrently maintain a high SE.

In this section, we compared the performances of FBMC as well as OFDM with and without centralized pre-equalization in a fiber-wireless integrated MFH network. Proof-of-concept experiments are conducted on an RoF testbed with two user terminals and one BBU pool. The testbed operates with an MMW frequency around 50 GHz. Bidirectional transmissions of 1.1-Ghz 5 aggregated CCs are realized over 25-km standard single mode fiber (SSMF) and 1.2-meter wireless channel. Experimental results demonstrate that under the synchronized down-link (DL) circumstance, both FBMC and OFDM can achieve similar performances. However, for asynchronous up-link (UL) transmissions with OFDM, the receiver at the BBU pool fails to obtain the correct channel information due to strong inter-band interference (IBI) between adjacent CCs from different users, but the performance of FBMC is not affected, which proves that FBMC can support signal processing and recovery among asynchronous data without sacrificing SE in next generation 5G compatible MFH networks.

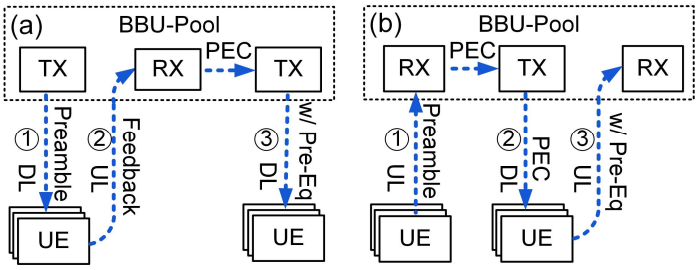

Figure 46. Flow diagrams of centralized pre-equalization process for (a) DL and (b) UL transmission in MFH networks supporting next-generation mobile technology. TX: transmitter; RX: receiver; PEC: pre-equalizer coefficients; UE: user equipment.

4.4.2 Operation Principles

The process of the centralized pre-equalization is accomplished by three steps, from Step 1 to Step 3, as shown in Figure 39(a) and (b). Assuming the channel is non-reciprocal, in DL transmission process, preambles acting as training symbols are inserted periodically in the data streams at BBU pool and transmitted to the user equipment (UE). At the UE ends, those training symbols are demodulated, quantized, and feedback to the receiver at the BBU pool. Feedbacks from multiple users will be used to estimate the channel and pre-distort the amplitude and phase of the DL signals globally in frequency domain._The minimum-mean-square-error (MMSE) method is used to achieve the pre-equalization coefficients [101]. In contrast, the UL pre-equalization process is initiated by sending preamble symbols from the UE to the BBU pool, which will be used for channel estimation to obtain pre-equalizer coefficients (PECs). PECs are communicated to the UE which will be used to perform UL pre-equalization. The above operation mode is somewhat similar to traditional close-loop adaptation [102] except that most of the computations are performed at the BBU pool, which reduces the complexity, power consumption, and cost at the distributed user terminals. In the following part, it is experimentally verified that FBMC could be a better candidate than OFDM for next generation fiber-wireless fronthaul

network with functioning centralization, such as centralized pre-equalization, due to its more concentrated spectral distribution with highly suppressed IBI. It is worth nothing that, limited by the experimental condition, in this proof-of-concept study, Step 2 shown in Figure 39(a) and (b) is realized by offline simulation. However, a comprehensive real-time experiment is going to be studied in future.

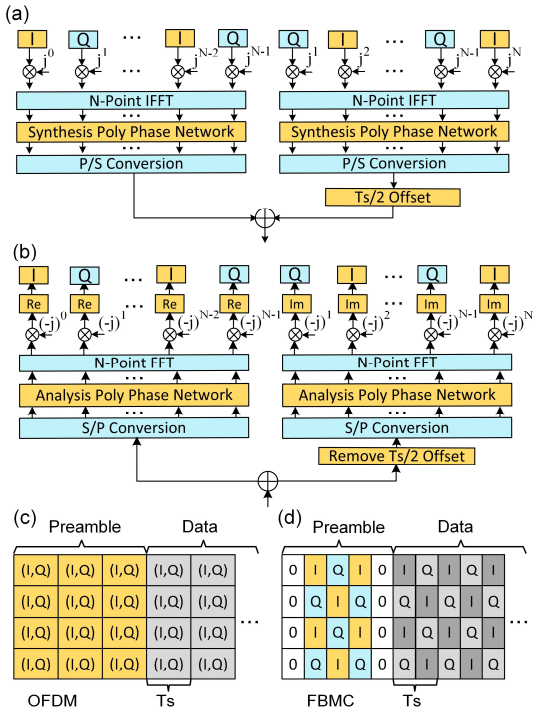

Figure 47. (a) and (b): schematic diagrams of FBMC transmitter and receiver respectively. (c) and (d): preamble and data structures of OFDM as well as FBMC.

The DSP blocks of a two-branch FBMC transmitter with N IFFT/FFT size are shown in Figure 47(a) [98]. $2\times N$ pulse amplitude modulated (PAM) symbol streams are sent into the transmitter as the input. A half-π phase delay is introduced between the adjacent symbol sequences. After IFFT, polyphase networks (PPNs) are used for pulse shaping towards N SCs. Square-root-raised-cosine (SRRC) filters with a roll-off factor of 1 are used as prototype filters to generate the coefficients of the PPNs. After PPN, the signal is parallel-to-serial converted and the output of the right branch is delayed by half of the symbol

period $T_S/2$ before it is combined with the output from the left branch. Because there is a $T_S/2$ timing offset between the in-phase and quadrature PAM components, such a modulation scheme is called offset quadrature amplitude modulation (OQAM). The DSP blocks for an FBMC receiver are shown in Figure 47(b), where the order of the DSP blocks is reversed to that shown in Figure 47(a). It is worth nothing that the time-frequency lattice structure of FBMC with OQAM modulation is different from that of OFDM. As shown in Figure 47(c), in OFDM, each time-frequency resource element (RE) is occupied by a complex QAM symbol (I+ jQ) with a symbol duration of T_S, where I and Q denote in-phase and quadrature components respectively. However, as shown in Figure 47(d), I and Q components in FBMC are interleaved and each RE only carries one real PAM symbol (I or Q) with a halved symbol period of $T_S/2$. To estimate the signal-to-interference-plus-noise ratio (SINR) and execute pre -equalization, preamble symbols are transmitted before the data blocks as shown in Figure 47(c) and (d). The preambles used for both OFDM and FBMC last three symbol periods ($3T_S$ and $3/2T_S$ respectively). However, one of the side effects of using FBMC is that, before equalization, there is always an intrinsic imaginary interference among neighboring SCs and symbols, which complicates the preamble design for channel estimation [103]. In this paper, to obtain accurate channel information without disturbance from the non-preamble symbols, zero guard symbols are inserted to isolate the preamble blocks from the data blocks as shown in Figure 47(d).

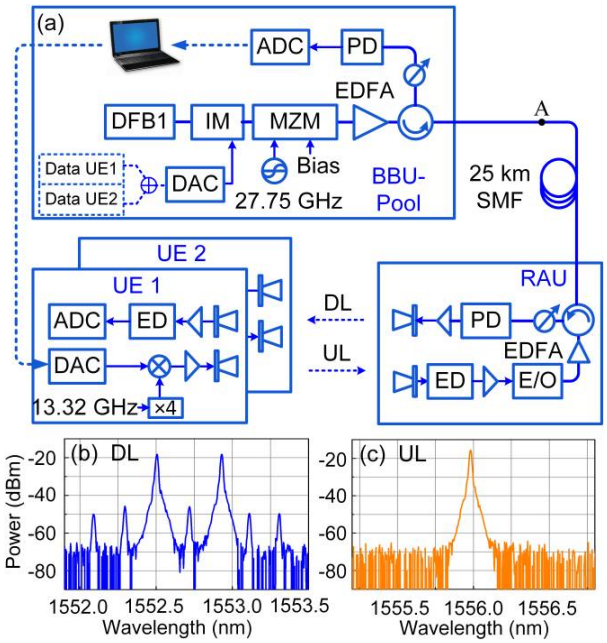

Figure 48. (a) Experimental setup for comparisons between OFDM and FBMC in a fiber-wireless integrated MFH network; (b) and (c): measured optical spectra at point A for DL and UL transmissions respectively.

4.4.3 Experimental Setup

Figure 48(a) shows the proof-of-concept fiber-wireless MFH network testbed to compare the transmission and pre-equalization performances between FBMC and OFDM based schemes. The testbed is composed of one BBU pool, one radio access unit (RAU), and two UE terminals. In this system, one DFB laser working at 1552.7 nm is used as DL light source. Five 220-MHz 128-SC OFDM/FBMC CCs with center frequencies at 0.445, 0.665, 0.885, 1.105, and 1.325 GHz are aggregated and modulated onto the light by an intensity modulator (IM). The electrical spectra of offline generated OFDM and FBMC CCs are shown in Figure 49(a) and (b) respectively. It can be observed that the out-of-band leakage of OFDM is much stronger than that of FBMC. To maximize the SE, the CCs are quasi-seamlessly aggregated with only one SC acting as a guard band between adjacent CCs. Therefore, the SC index allocated for CC1 to CC5 is from 1 to 128, 130 to 257, 259

to 386, 388 to 515, and 517 to 644 respectively. The data of UE1 and UE2 is carried by odd and even CC sets respectively with modulation formats of 16QAM or 64QAM.

For DL transmission, the two CC sets are combined offline and sent to Tektronix 7122C arbitrary waveform generator (AWG) with a sampling rate of 4.5 GSa/s and a symbol duration T_S of 0.582 ms. After intensity modulation, a 40-GHz Mach-Zehnder modulator (MZM) biased at the minimum intensity-output point is used to suppress the central optical carrier. Two optical side bands with 55.5-GHz separation are preserved. The optical spectrum after optical-carrier-suppressed (OCS) modulation is shown in Figure 48(b). After 25-km SSMF transmission, the optical MMW signals are detected by a 70-GHz photodetector (PD). A pair of horn antennas with 15-dBi gains is used to deliver and receive the MMW signals. The wireless transmission distances from the RAU to both UE1 and UE2 are set to be 1.2 m, which is limited by the output power of the radio transmitters. Within each UE site, an envelope detector (ED) is used to down-convert the signals before they are sampled by a digital scope and demodulated offline. The upstream transmission links with two TX antennas and one RX antenna are also set up as shown in Figure 48(a). The odd and even CC sets are generated by UE1 and UE2 respectively. A delay of $0.05T_S$ is introduced between the two CC sets to imitate asynchronous ULs with different transmission latencies. The CC sets are mixed with 53.28-GHz local oscillators (LOs) and up-converted to MMWs before they are emitted out, combined, and received at the RAU. An ED is used to down-convert the signals, which are amplified and modulated onto the light by a 10-GHz IM. After 25-km SSMF transmission, the signals are detected and sampled by a digital scope. The UL optical spectrum after fiber transmission is shown in Figure 48(c).

4.4.4 Experimental Results and Analysis

The electrical spectra of OFDM and FBMC CCs before and after pre-equalization are shown in Figure 49(c) to (i). As shown in Figure 49(c), (e), (f), and (h), the power degradations from 0 to 1.5 GHz are mainly induced by limited response bandwidth of electrical/optical devices and chromatic dispersion induced fading after fiber transmission. With the pre-equalization process, flattened channel response can be obtained as shown by Figure 49(d), (g), and (i).

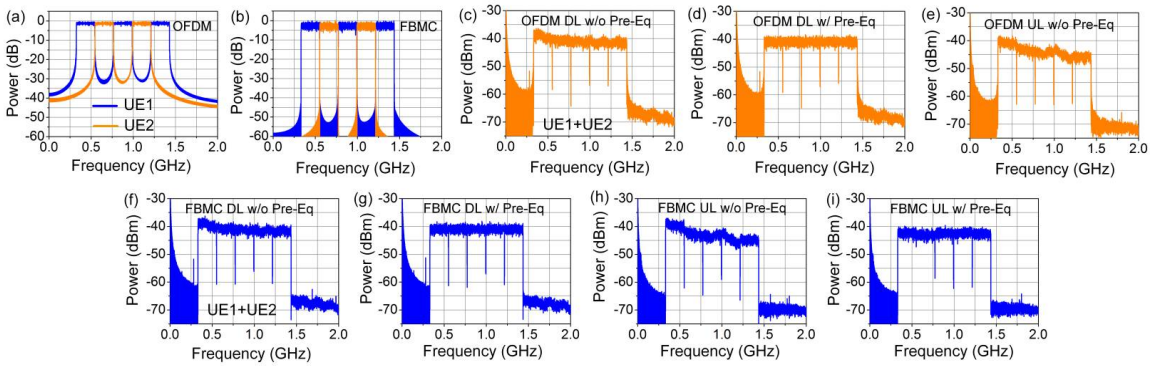

Figure 49. (a) and (b): electrical spectra of offline generated OFDM and FBMC respectively; (c) to (e): electrical spectra of received OFDM signals for DL without pre-equalization, DL with pre-equalization, and UL without pre-equalization respectively; (f) to (i): electrical spectra of received DL and UL FBMC signals with and without pre-equalization.

The results of SINR with and without pre-equalization are shown by Figure 50. For UL transmission, as shown in Figure 50(a), since the odd and even CCs from UE1 and UE2 are decorrelated respectively, the large out-of-band leakage of OFDM will introduce serious interference to the adjacent bands thus leading to significant SINR degradation especially at the band-edge SCs. Because the original channel response is distorted by the SINR dips centered at one-SC guard bands between adjacent CCs, accurate channel information cannot be obtained which results in the failure of pre-equalization for OFDM

UL transmission. In comparison, because of the rapid power decay at band edges of FBMC, a high side lobe suppression ratio can be obtained. Thus the channel response is not affected by IBI and pre-equalization works effectively even with asynchronous UL transmission. The issue of strong IBI among asynchronous OFDM CCs also leads to significant power penalties on error vector magnitude (EVM) as shown in Figure 51(c) and (d). However, under the circumstance of DL transmission when all the CCs are synchronized, both OFDM and FBMC have similar performances with pre-equalization.

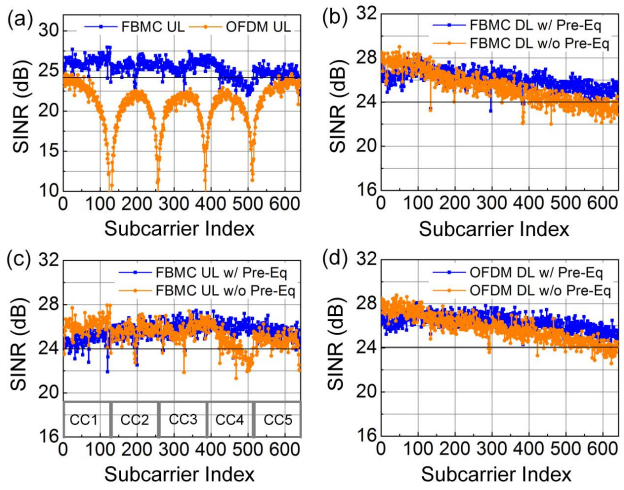

Figure 50. SINR as functions of SC index with 25-km SSMF transmissions for (a) FBMC versus OFDM UL, (b) FBMC DL, (c) FBMC UL, and (d) OFDM DL.

Typically, equalization among multiple users in UL is challenging to be realized by distributed post-equalization schemes only. However, with centralized pre-equalization, the transmission quality of CCs from different users can be balanced, and the overall number of SCs passing the SINR threshold (e. g. 24 dB) is significantly increased as shown in Figure 50(b) to (d). The results of constellations and EVM versus received power are shown in Figure 51 with the electrical amplifiers and PD operating in the linear region. For all the conditions except OFDM UL transmission, less than 6% EVM with 64QAM can be obtained.

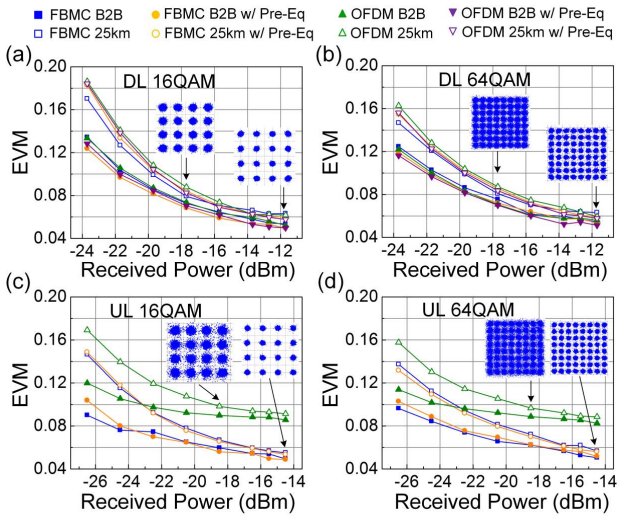

Figure 51. EVM as functions of received optical power for (a) DL 16QAM, (b) DL 64QAM, (c) UL 16QAM, and (d) UL 64QAM.

4.5 Summary

Spectral aggregation and cell densification are two of the key strategies to effectively boost the throughput of future 5G mobile data networks. Meanwhile, they have higher requirements on fronthaul network's capacity, scalability, and cost. To solve these issues, in this work, we proposed a small-cell compatible WDM-FDM based bidirectional mobile fronthaul network. In comparison with traditional CPRI, CA/CDA, or TDM based schemes, the proposed system could support increased number of connected cells with higher flexibility and lower latency. On the other hand, because of the impairments caused by OBI and phase noise, traditional IM-DD scheme that fails to support FDM UL transmission is replaced with our designed FM-HD method which can recover the UL signals from distributed asynchronous cells with the help of VT based DSP. A proof-of-concept bidirectional transmission experiment is demonstrated which successfully transmits 20 80-MHz DL CCs and 16 80-MHz UL CCs between the BBU-Pool and two

independent small-cell RAUs. Qualified EVM performances and clear constellations are obtained which proves the feasibility of the proposed fronthaul system.

Meanwhile, we have investigated FBMC with the centralized pre-equalization and compared its performances with traditional OFDM in a fiber-wireless integrated analog MFH for 5G applications. Bidirectional RoF transmission experiments are conducted over 25-km SSMF and 1.2-m wireless channel with one BBU pool connecting with two UE sites. 1.1-GHz 5-CCs dense CA over 50-GHz MMW is obtained. The results show that the pre-equalization is effective to compensate the channel penalties among multiple users. Both OFDM and FBMC signals can achieve comparable performances in DL. However, for asynchronous UL transmission, pre-equalization becomes ineffective for OFDM because of its serious out-of-band power leakage and IBI, which also leads to higher power penalties on EVM performances. In comparison, FBMC performs better with centralized pre-equalization due to its more concentrated spectral power distribution and less inter-band crosstalk. With these advantages, FBMC could be a promising modulation scheme compatible with next-generation MFH with centralized functions to reduce the distributed cost and support spectral efficient asynchronous network coordination and management for future 5G applications.

CHAPTER 5. CONCLUSIONS

The final chapter summarizes my doctoral works in next-generation digital radio-over-fiber based mobile fronthaul systems and multiband modulation as well as related digital signal processing techniques in future fiber-wireless integrated networks. The technical contributions and achievements of this research work are concluded in Section 5.1. Future research directions and potential improvements about to these works are discussed in Section 5.2.

5.1 Technical Conclusions

This dissertation investigates the key technologies in digital mobile fronthaul systems with bidirectional transmission, data compression, advanced modulation formats, and multiband multiplexing which could provide potential solutions for 5G compatible fiber-wireless integrated access networks. The major technical contributions are summarized as follows.

5.1.1 Advanced Data Compression Techniques in Digital Mobile Fronthaul Systems

Because of its lower bandwidth efficiency, rumours arise that digital radio-over-fiber technologies may not be a qualified candidate for 5G compatible high-capacity mobile backhaul or tier-II fronthaul. But it is not the case in short range and latency-stringent tier-I mobile fronthaul network because of the high resistance against nonlinear distortions, straightforward DSP architecture, and compatibility with different formats. In our study, we focused on improving the bandwidth efficiency of D-RoF through compressing the effective quantization digits using fast statistical estimation, Lloyd algorithm, and

differential pulse coded modulation. After combining with high-order modulation formats, bandwidth efficiency of D-RoF systems can even be increased by 4 times.

To achieve data compression, traditional statistical estimation methods are based on probabilistic distribution fitting which is computational complex because of using a large number of samples to estimate the expectation and variance. In our work, fast statistical estimation method is proposed. It assumes the discrete waveform samples are distributed on the range of $[\mu + K\sigma, \mu - K\sigma]$. After using bias-tee to eliminate the DC component and normalization of the waveform amplitude scales, the variance can be immediately estimated without statistical fitting process. To further simplify the computation, truncated folded Gaussian distribution is applied which halves the number of estimated boundaries. Fast statistical estimation is proved to be an accurate method if the window length coefficient, K, is properly set.

On the other hand, although, fast statistical estimation based data compression is an efficient and precise method, it is based on Gaussian distribution assumption and cannot be used to resolve the data compression issue in non-Gaussian distributed waveforms. Thus, to develop a generalized data compression algorithm to be used for any kind of wireless data format is of great importance in 5G mobile network with diverse service environment. Therefore, we proposed relaxed Lloyd algorithm which is format agnostic. Compared with traditional methods including FSE, lowest quantization noise level can be achieved especially when fewer quantization levels are applied. A good trade-off between quantization noise level and computing complexity can be achieved. The recovered signal quality can be further improved when combining relaxed Lloyd algorithm with differential pulse coded modulation.

5.1.2 Multiband CAP Modulation and Efficient Data Multiplexing in Mobile Fronthaul Networks

Other than higher average data throughput, ultra-low latency has recently become a critical requirement in 5G-NR standards. However, traditional time division multiplexing in both E-PON and G-PON systems may fail to achieve this goal because of the following reasons. Firstly, in TDM systems, the distributed access points will be periodically swept and waiting for the window allowed for their transmission, which lacks the flexibility and wastes too much time in buffering. Secondly, to fulfil its functions correctly and stably, TDM systems may require a set of sophisticated bidirectional coordination and communications, which further increases the system delay. Thus, it is necessary to consider new data multiplexing scheme in next-generation mobile fronthaul systems and among them frequency-domain multiband multiplexing can be a desired option.

In multiband systems, different data transmitted to distributed RAUs can be mapped and packaged into different frequency bands and they don't need to be synchronized when choosing bandlimited digital filters like square-root raised cosine filters. Regular QAM and offset-QAM based multiband CAP modulation are discussed and compared in Chapter 3. It is demonstrated that regular QAM CAP multiband modulations are typically based on bandlimited digital filters thus different data in different channels can be well isolated without interference and strict synchronization requirements. If channels are pre-allocated to corresponding RAUs, the time spent on buffering to avoid congestion can be eliminated. On the other hand, OQAM-based CAP multiband modulation recently attracts the attention from academic. It has higher spectral efficiency and lower computational complexity because it relaxes the orthogonality condition in the time-frequency lattice space and

allows the use of Gaussian like filters which is highly resistant to truncation effect thus leading to significantly shortened filter length. Some representative results about OQAM multiband CAP modulation in Tier-II mobile fronthaul are also selected and demonstrated in Section 3.5.

5.1.3 Bidirectional Point-to-Multi-Point Data Transmission in Analog Mobile Fronthaul Systems

In this part, the data transmission penalties in a bidirectional point-to-multi-point mobile fronthaul are analysed. It is noticed that, because the light-wave signals in different independent distributed small cells have different phases and polarizations, incoherent optical beating components will be generated and interfered with the desired signal bands and thus reducing the signal-to-noise-plus-interference ratio of the recovered signals.

To avoid such penalties in the up-link transmission, field modulation and heterodyne detection technique is developed. By utilizing it, the optical beating components and the desired signals will not be overlapped in frequency domain which enables us to filter out the optical signals from different RAUs. By inserting virtual tones, it enables us to track and restore the phase vibrations as well as the carrier frequency off-set of the signals which benefits the signal recovery process and improves the received signal quality. The influence on the systems under different bias voltages has also been studied and compared.

5.2 Future Work

It has been demonstrated in this dissertation that digital radio-over-fiber technologies will become an important part in future multi-tier 5G compatible mobile fronthaul networks. Data compression is an important tool to overcome its problem of lower bandwidth efficiency. However, there are still some technical issues remained to be solved. Firstly, it is still needed to study the performance of the data compression algorithm when there are noise and channel penalties in up-link transmission. Secondly, the data compression methods studied in this dissertation inevitably result in increasing the quantization noise. However, there exist some data compression methods based on sparse coding and machine learning assisted processing which could potentially obtain lossless data compression. Moreover, higher compression gain could be potentially achieved through some data traffic based methods.

Except from those improvements in data compression, there are also other directions which can be studied to improve the performance of digital mobile fronthaul. Delta-sigma modulation is also an effective method to improve the transmission efficiency of digital fronthaul. It is possible to replace traditional uniform quantizer in delta-sigma modulator with non-uniform quantizer combined with FSE or Lloyd based algorithm to optimize the distribution of the quantization levels. The quantization noise level is expected to be reduced and thus more bandwidth could be released to carry wireless signal components. It is also an interesting topic to design the protocol and interface to allow the coexistence of traditional CPRI, data compressed D-RoF, functional split, and even analog signals and to enable the network adaptively selecting the best option under different application scenarios.

Furthermore, future digital fronthaul system could also be considered to be implemented over coherent-PON systems which could maximize the system spectral efficiency and to support the emerging new technologies like massive MIMO and beamforming, which require a large network capacity. On the other hand, since in MIMO and beamforming systems, the channel can sometimes be modeled as a sparse matrix and the data streams in adjacent antenna bins are highly correlated which indicates that data compression could potentially obtain higher compression gain in these systems. Thus, advanced data compression in mobile fronthaul supporting massive MIMO and beamforming systems can be another impactful research topic.

REFERENCES

[1]. V. Jungnickel K. Manolakis, W. Zirwas, B. Panzner, V. Braun, M. Lossow, M. Sternad, R. Apelfröjd, and T. Svensson., "The role of small cells, coordinated multipoint, and massive MIMO in 5G," *IEEE Commun. Mag.*, vol. 52, no. 5, pp. 44-51, May 2014.

[2]. 3GPP Technical Report 38.913, "Study on Scenarios and Requirements for Next Generation Access Technologies," Mar. 2016.

[3]. Recommendation ITU-R M.2083-0, "Framework and overall objectives of the future development of IMT for 2020 and beyond," Sep. 2015.

[4]. R. G. Maunder, "The 5G channel code contenders," ACCELERCOMM white paper.

[5]. G. K. Chang, M. Xu and F. Lu, "Fiber-wireless convergence for next generation heterogeneous mobile data communications," in *Proc. IEEE Photonics Society Summer Topical Meeting Series*, pp. 117-118, Jul. 2017.

[6]. China Mobile, "C-RAN: The road towards green ran," White Paper, 2011.

[7]. K. Miyanabe K. Suto, Z. M. Fadlullah, H. Nishiyama, N. Kato, H. Ujikawa, and K.-I. Suzuki, "A cloud radio access network with power over fiber toward 5G networks: QoE-guaranteed design and operation," *IEEE Wireless Commun.*, vol. 22, no. 4, pp. 58-64, Aug. 2015.

[8]. M. Peng, Y. Li, Z. Zhao, and C. Wang, "System architecture and key technologies for 5G heterogeneous cloud radio access networks," *IEEE Network*, vol. 29, no. 2, pp. 6-14, Mar, 2015.

[9]. T. Pfeiffer, “Next generation mobile fronthaul and midhaul … [Invited],” *J. Opt. Commun. Netw.*, vol. 7, no. 11, pp. B38-B45, Nov. 2015.

[10]. A. Maeder, M. Lalam, A. De Domenico, E. Pateromichelakis, D. Wubben, J. Bartelt, R. Fritzsche and P. Rost, “Towards a flexible functional split for cloud-RAN networks,” in *Proc. EuCNC* Jun. 2014, paper 6882691.

[11]. 3GPP Technical Report, “Radio access architecture and interfaces,” Release 14, Mar. 2017.

[12]. IEEE 1914 Next Generation Fronthaul Interface (NGFI) WG: http://sites.ieee.org/sagroups-1914/

[13]. Common Public Radio Interface (CPRI), The CPRI Specification version V7.0, 2015.

[14]. X. Liu, F. Effenberger, N. Chand, L. Zhou, and H. Lin. “Demonstration of bandwidth-efficient mobile fronthaul enabling seamless aggregation of 36 E-UTRA-like wireless signals in a single 1.1-GHz wavelength channel,” in *Proc. OFC*, Mar. 2015, paper M2J.2.

[15]. F. Effenberger and X. Liu, “Power-efficient method for IM-DD optical transmission of multiple OFDM signals,” *Opt. Express*, vol. 23, no. 10, pp. 13571-13579, May 2015.

[16]. X. Liu, H. Zeng, N. Chand, and F. Effenberger, “Experimental demonstration of high-throughput low-latency mobile fronthaul supporting 48 20-MHz LTE signals with 59-Gb/s CPRI-equivalent rate and 2-μs processing latency,” in *Proc. ECOC*, Sep. 2015, paper We.4.4.3.

[17]. X. Liu, H. Zeng, N. Chand, and F. Effenberger, “CPRI-compatible efficient mobile fronthaul transmission via equalized tdma achieving 256 Gb/s CPRI-equivalent data

rate in a single 10-GHz-bandwidth IM-DD channel," in *Proc. OFC*, Mar. 2016, paper W1H.3.

[18]. M. Zhu, X. Liu, N. Chand, F. Effenberger, and G.-K. Chang, "High-capacity mobile fronthaul supporting LTE-advanced carrier aggregation and 8 × 8 MIMO," in *Proc. OFC*, Mar. 2015, paper M2J.3.

[19]. M. Zhu, F. Li, F. Lu, J. Yu, C. Su, G. Gu, and G.-K. Chang, "Wavelength resource sharing in bidirectional optical mobile fronthaul," *J. Lightwave Technol*. vol. 33, no. 15, pp. 3182-3188, Aug. 2015.

[20]. C. Kottke, K. Habel, M. H. Eiselt, H. Griesser, and J. P. Elbers, "Coherent subcarrier-WDM-PON system with SSB modulation and wavelength reuse," in *Proc. OFC*, Mar. 2013, paper OM2A.3.

[21]. J. von Hoyningen-Huene, H. Griesser, M. H. Eiselt, and W. Rosenkranz, "Experimental demonstration of OFDMA-PON uplink-transmission with four individual ONUs," in *Proc. OFC*, Mar. 2013, paper OTh3A.2.

[22]. S. Amiralizadeh, A. T. Nguyen, C. S. Park, and L. A. Rusch, "Single-fiber lightwave centralized WDM-OFDMA-PON with colorless optical network units," *J. Opt. Commun. Netw.* vol. 8, no. 4, pp. 196-205, Mar. 2016.

[23]. R. Schreier and G. C. Temes, Understanding Delta-Sigma Data Converters, ISBN 978-0-471-46585-0, Wiley 2004.

[24]. J. Wang, Z. Yu, K. Ying, J. Zhang, F. Lu, M. Xu, and G.-K. Chang, "Delta-sigma modulation for digital mobile fronthaul enabling carrier aggregation of 32 4G-LTE / 30 5G-FBMC signals in a single-λ 10-Gb/s IM-DD channel," in *Proc. OFC*, Mar. 2016, paper W1H.2.

[25]. K. Miyamoto, S. Kuwano, J. Terada, and A. Otaka, “Analysis of mobile fronthaul bandwidth and wireless transmission performance in split-PHY processing architecture,” *Opt. Express* vol. 24, no.2, pp. 1261-1268, Jan. 2016.

[26]. J. Terada, T. Shimada, T. Shimizu, and A. Otaka, “Optical Network Technologies for Wireless Communication Network,” in *Proc. ECOC*, pp. 232-234, Sep. 2016.

[27]. Open Base Station Architecture Initiative (OBSAI), Reference Point 3 Specification, Version 4.2, 2010.

[28]. M. Xu, X. Liu, N. Chand, F. Effenberger, and G.-K. Chang, “Fast statistical estimation in highly compressed digital RoF systems for efficient 5G wireless signal delivery,” in *Proc. OFC*, Mar. 2017, paper M3E.7.

[29]. K. Zhong, X. Zhou, T. Gui, L. Tao, Y. Gao, W. Chen, J. Man, L. Zeng, A. P. T. Lau, and C. Lu, “Experimental study of PAM-4, CAP-16, and DMT for 100 Gb/s short reach optical transmission systems,” *Opt. Express*, vol. 23, no. 2, pp. 1176-1189, Jan. 2015.

[30]. C. Chen, X. Tang, and Z. Zhang, “Transmission of 56-Gb/s PAM-4 over 26-km single mode fiber using maximum likelihood sequence estimation,” in *Proc. OFC*, Mar. 2015, paper Th4A.5.

[31]. C. Cole, I. Lyubomirsky, A. Ghiasi, and V. Telang, “Higher-order modulation for client optics,” *IEEE Commun. Mag.*, vol. 51, no. 3, pp. 50–57, Mar. 2013.

[32]. S. H. Kim, H. S. Chung, and S. M. Kim, “Experimental demonstration of CPRI data compression based on partial bit sampling for mobile front-haul link in C-RAN,” in *Proc. OFC*, Mar. 2016, paper W1H.5

[33]. K. Tanaka, and A. Agata, “Next-generation optical access networks for C-RAN,” in *Proc. OFC*, Mar. 2015, paper Tu2E.1.

[34]. N. Shibata, T. Tashiro, S. Kuwano, N. Yuki, Y. Fukada, J. Terada, and A. Otaka, “Performance evaluation of mobile front-haul employing ethernet- based TDM-PON with IQ data compression [Invited],” *J. Opt. Commun. Netw.*, vol. 7, no. 11, pp. B16-B22, Nov. 2015.

[35]. B. Guo, W. Cao, A. Tao, and D. Samardzija, “LTE/LTE-A signal compression on the CPRI interface,” *Bell Labs Tech. J.*, vol. 18, no. 2, pp. 117–133, Sep. 2013.

[36]. ETSI, Open Radio Equipment Interface (ORI), ORI interface specification, Part 1: Low Layers, Release 4, 2014.

[37]. S. Megeed, X. Liu, H. Zeng, and F. Effenberger, “Demonstration of a FPGA-based CPRI-over-Ethernet real-time system achieving 120 Gb/s throughput over a 10-km SSMF link with 16 bi-directional 10GE connections,” in *Proc. OFC*, Mar. 2017, paper Th4B.2.

[38]. 3GPP RP-160671, “Study on NR New Radio Access Technology,” new SID proposal, Mar. 2016.

[39]. ITU-T, “The tactile internet watch report,” white paper, Aug. 2014.

[40]. T. Tashiro, S. Kuwano, J. Terada, T. Kawamura, N. Tanaka, S. Shigematsu, and N. Yoshimoto, “A novel DBA scheme for TDM-PON based mobile fronthaul,” *Proc. OFC*, paper Tu3F.3, Mar. 2014.

[41]. J. Kani, “Solutions for future mobile fronthaul and access-network convergence,” *Proc. OFC*, tutorial paper W1H.1, Mar. 2016.

[42]. M. Xu, X. Liu, N. Chand, F. Effenberger, and G.-K. Chang, “Flex-frame timing-critical passive optical networks for delay sensitive mobile and fixed access services,” in *Proc*. *OFC*, paper Th4B.6, Mar. 2017.

[43]. A. Helmy, H. Fathallah, and H. Mouftah, “Interleaved polling versus multi-thread polling for bandwidth allocation in long-reach PONs,” *J. Opt. Commun. Netw.*, vol. 4, no. 3, pp. 210-218, March 2012.

[44]. J.-Y. Lee, I-S. Hwang, A. Nikoukar, and A. T. Liem, “Comprehensive performance assessment of bipartition upstream bandwidth assignment schemes in GPON,” *J. Opt. Commun. Netw.*, vol. 5, no. 11, pp. 1285-1295, Nov. 2013.

[45]. Y. Luo and N. Ansari, “Limited sharing with traffic prediction for dynamic bandwidth allocation and QoS provisioning over Ethernet passive optical networks,” *J. Opt. Netw.* vol. 4, no. 9, pp. 561-572, Sep. 2005.

[46]. T. Kobayashi, H. Ou, D. Hisano, T. Shimada, J. Terada, A. Otaka, “Bandwidth allocation scheme based on simple statistical traffic analysis for TDM-PON based mobile fronthaul,” in *Proc*. *OFC*, paper W3C.7, Mar. 2016.

[47]. M. I. Olmedo, T. Zuo, J. B. Jensen, Q. Zhong, X. Xu, S. Popov, and I. T. Monroy, “Multiband Carrierless Amplitude Phase Modulation for High Capacity Optical Data Links,” *J. Lightwave Technol*. vol. 32, no. 4, pp. 898-804, Feb. 2014.

[48]. J. Zhang, X. Li, J. Xiao, G. Chang, and F. Li, “Demonstration of 24-Gb/s carrier-less amplitude and phase modulation (CAP) 64QAM radio-over-fiber system over 40-GHz Mm-wave fiber-wireless transmission,” in *Proc*. *OFC*, paper M2D.5. Mar. 2014.

[49]. T. P. McKenna, J. A. Nanzer and T. R. Clark, "Experimental demonstration of photonic millimeter-wave system for high capacity point-to-point wireless communications," *J. Lightwave Technol*., vol. 32, no. 20, pp. 3588-3594, Oct. 2014.

[50]. J. D. Reis, A. Shahpari, R. M. Ferreira, D. M. Neves, M. Lima, and A. L. Teixeira, "Nyquist signaling for spectrally-efficient optical access networks," in *Proc. OFC*, paper W3G.7, Mar. 2014.

[51]. B. Sahin, I. Guvenc and H. Arslan, "A survey on multicarrier communications: prototype filters, lattice structures, and implementation aspects," *IEEE Commun. Surveys* and *Tutorials*, vol. 16, no. 3, pp. 1312-1338, Third Quarter 2014.

[52]. A. Liu, J. Pan, T. Detwiler, A. Stark, Y. Hsueh, G. Chang and S. E. Ralph, "Joint ICI cancellation for superchannel coherent optical systems in nonlinear transmission regimes," in *Proc. OFC,* Mar. 2013, paper OTu2I.4.

[53]. M. Xiang, S. Fu, H. Tang, M. Tang, P. Shum and D. Liu, "Linewidth-tolerant joint digital signal processing for 16QAM Nyquist WDM superchannel," *IEEE Photon. Technol. Lett.*, vol. 27, no. 2, pp. 129-132, Jan. 2015.

[54]. M.-F. Huang, A. Tanaka, E. Ip, Y.-K. Huang, D. Qian, Y. Zhang, S. Zhang, P. N. Ji, I. B. Djordjevic, T. Wang, Y. Aono, S. Murakami, T. Tajima, T. J. Xia and G. A. Wellbrock, "Terabit/s Nyquist superchannels in high capacity fiber field trials using DP-16QAM and DP-8QAM modulation formats," *J. Lightwave Technol*., vol. 32, no. 4, pp. 776-782, Feb. 2014.

[55]. Z. Zheng, D. Wang, X. Zhu, X. Lv, K. Zou, Y. Zhu, F. Zhang and Z. Chen, "Orthogonal-band-multiplexed offset-QAM optical superchannel generation and coherent detection," *Sci. Rep.*, vol. 5, no. 17891, pp. 1-10, Dec. 2015.

[56]. J. Zhao and A. D. Ellis, “Offset-QAM based coherent WDM for spectral efficiency enhancement,” *Opt. Express*, vol. 19, no. 15, pp. 14617–14631, Jul. 2011.

[57]. S. Randel, A. Sierra, X. Liu, S. Chandrasekhar, and P. Winzer, "Study of multicarrier offset-QAM for spectrally efficient coherent optical communications," in *Proc. ECOC*, Sep. 2011, paper Th.11.A.1.

[58]. J. Li, E. Tipsuwannakul, T. Eriksson, M. Karlsson and P. A. Andrekson, “Approaching Nyquist limit in WDM systems by low-complexity receiver-side duobinary shaping,” *J. Lightwave Technol.*, vol. 30, no. 11, pp. 1664-1676, Jun. 2012.

[59]. C. Xie and S. Chen, “Quadrature duobinary modulation and detection,” in *Proc. OFC*, Mar. 2015, paper W4K.6.

[60]. S. W. Smith, *The Scientist and Engineer's Guide to Digital Signal Processing*, California Technical Publishing, 1st ed., 1997, ch. 16.

[61]. G. Bosco, V. Curri, A. Carena, P. Poggiolini and F. Forghieri, “On the performance of Nyquist-WDM terabit superchannels based on PM-BPSK, PM-QPSK, PM-8QAM or PM-16QAM subcarriers,” *J. Lightwave Technol.*, vol. 29, no. 1, pp. 53-61, Jan. 2011.

[62]. X. Liu, H. Zeng, N. Chand and F. Effenberger, “Efficient mobile fronthaul via DSP-based channel aggregation,” *J. Lightwave Technol.*, vol. 34, no. 6, pp. 1556-1564, Mar. 2016.

[63]. T. Jiang, W. Xiang, P. C. Richardson, D. Qu, and G. Zhu, “On the nonlinear companding transform for reduction in PAPR of MCM signals,” *IEEE Trans. Wireless Commun.*, vol. 6, no. 6, pp. 2017–2021, Jun. 2007.

[64]. C. W. Brokish and M. Lewis, “A-Law and mu-Law companding implementations using the TMS320C54x,” Texas Instruments Digital Processing Solutions, Dec. 1997.

[65]. J. Wang, Z. Jia, L. A. Campos, C. Knittle, and G.-K. Chang, “Optical coherent transmission of 20x192-MHz DOCSIS 3.1 channels with 16384-QAM based on delta-sigma digitization,” in *Proc. OFC*, Mar. 2017, paper Th1K.1.

[66]. A. de la Oliva, J. A. Hernandez, D. Larrabeiti, and A. Azcorra, “An overview of the CPRI specification and its application to C-RAN-based LTE scenarios,” *IEEE Commun. Mag.*, vol. 54, no. 2, pp. 152–159, Feb. 2016.

[67]. J. Zhang, J. Yu, F. Li, N. Chi, Z. Dong and X. Li, “11 × 5 × 9.3Gb/s WDM-CAP-PON based on optical single-side band multi-level multi-band carrier-less amplitude and phase modulation with direct detection,” *Opt. Express*, vol. 21, no. 16, pp. 18842-18848, Aug. 2013.

[68]. M. Xu, J. Zhang, F. Lu, J. Wang, L. Cheng, D. Guidott, G.-K. Chang, “Orthogonal multiband CAP modulation based on offset-QAM and advanced filter design in spectral efficient MMW RoF systems,” *J. Lightwave Technol.*, vol. 35, no. 4, pp. 997-1005, Jul. 2016.

[69]. X. Liu, P. J. Winzer, S. Chandrasekhar, S. Randel and S. Corteselli, “Multiband DFT-spread-OFDM equalizer with overlap-and-add dispersion compensation for low-overhead and low-complexity channel equalization,” in *Proc. OFC*, Mar. 2013, paper OW3B.2.

[70]. M. Xu, J.-H. Yan, J. Zhang, F. Lu, J. Wang, L. Cheng, D. Guidotti, and G.-K. Chang, “Bidirectional fiber-wireless access technology for 5G mobile spectral aggregation

and cell densification," *J. Opt. Commun. Netw.*, vol. 8, no. 12, pp. B104-B110, Dec. 2016.

[71]. J. Zhang, M. Xu, J. Wang, F. Lu, L. Cheng, M. Zhu, M. I. Khalil, J. Yu, and G.-K. Chang, "Carrier aggregation for MMW inter-RAT and intra-RAT in next generation heterogeneous mobile data network based on optical domain band mapping," in *Proc. ECOC*, Sep. 2015, paper We.4.4.5.

[72]. C.-L. I and Jinri Huang, "RAN revolution with NGFI (xHaul) for 5G," in *Proc. OFC* paper W1C.7, Mar. 2017.

[73]. M. Xu, F. Lu, J. Wang, L. Cheng, D. Guidotti, and G.-K. Chang, "Key technologies for next-generation digital RoF mobile fronthaul with statistical data compression and multiband modulation", *J. Lightwave Technol.*, vol. 35, no. 17, pp. 3671-3679, 2017.

[74]. N. Benvenuto and G. Cherubini, Algorithms for Communications Systems and Their Applications. New York: Wiley, 2002.

[75]. Z. Jia, J. Yu, G. Ellinas and G. K. Chang, "Key enabling technologies for optical–wireless networks: optical millimeter-wave generation, wavelength reuse, and architecture," *J. Lightwave Technol.*, vol. 25, no. 11, pp. 3452-3471, Nov. 2007.

[76]. A. Chowdhury, H. C. Chien, Y. T. Hsueh and G. K. Chang, "Advanced system technologies and field demonstration for in-building optical-wireless network with integrated broadband services," *J. Lightwave Technol.*, vol. 27, no. 12, pp. 1920-1927, Jun. 2009.

[77]. *IEEE Std.*, IEEE802.11ad [Online]. Avaliable: http://standards.ieee. org/findstds/standard/802.11ad-2012.html.

[78]. F. Boccardi, R. W. Heath, A. Lozano, T. L. Marzetta and P. Popovski, “Five disruptive technology directions for 5G,” *IEEE Commun. Mag.*, vol. 52, no. 2, pp. 74-80, Feb. 2014.

[79]. J. L. Wei, Q. Cheng, D. G. Cunningham, R. V. Penty, I. H. White and H. Griesser, “High performance 400 Gigabit Ethernet links using hybrid multiband CAP/QAM scheme,” in *Proc. OFC*, Mar. 2015, paper Th5B.3.

[80]. Z. Jia, J. Yu, H. C. Chien, Z. Dong and D. Di Huo, “Field transmission of 100 G and beyond: multiple baud rates and mixed line rates using Nyquist-WDM technology,” *J. Lightwave Technol.*, vol. 30, no. 24, pp. 3793-3804, Dec. 2012.

[81]. D. Hillerkuss, R. Schmogrow, M. Meyer, S. Wolf, M. Jordan, P. Kleinow, N. Lindenmann, P. C. Schindler, A. Melikyan, X. Yang, S. Ben-Ezra, B. Nebendahl, M. Dreschmann, J. Meyer, F. Parmigiani, P. Petropoulos, B. Resan, A. Oehler, K. Weingarten, L. Altenhain, T. Ellermeyer, M. Moeller, M. Huebner, J. Becker, C. Koos, W. Freude and J. Leuthold, “Single-laser 32.5 Tbit/s Nyquist WDM transmission,” *J. Opt. Commun. Netw.* vol. 4, no. 10, pp. 715-723, Oct. 2012.

[82]. M. Xu, J. Zhang, F. Lu, L. Cheng, J. Wang, D. Guidotti, T. Kanesan, S. M. Mitani, and G.-K. Chang, “Multiband OQAM CAP modulation in MMW RoF systems with enhanced spectral and computational efficiency,” in *Proc. OFC*, Mar. 2016, paper Tu3B.3.

[83]. B. Farhang-Boroujeny, “OFDM versus filter bank multicarrier,” *IEEE Signal Processing Mag.*, vol. 28, no. 3, pp. 92-112, May 2011.

[84]. J. Du and S. Signell, “Classic OFDM systems and pulse-shaping OFDM/OQAM systems,” *Technical Report* (*KTH – Royal Institute of Technology*), pp. 1-32, Feb. 2007.

[85]. K. Okada, K. Kondou, M. Miyahara, M. Shinagawa, H. Asada, R. Minami, T. Yamaguchi, A. Musa, Y. Tsukui, Y. Asakura, S. Tamonoki, H. Yamagishi, Y. Hino, T. Sato, H. Sakaguchi, N. Shimasaki, T. Ito, Y. Takeuchi, N. Li, Q. Bu, R. Murakami, K. Bunsen, K. Matsushita, M. Noda, and A. Matsuzawa, “Full four-channel 6.3-Gb/s 60 GHz CMOS transceiver with low-power analog and digital baseband circuitry,” *IEEE J. Solid-State Circuits*, vol. 48, no. 1, pp. 46–65, Jan. 2013.

[86]. J. Pan, C. Liu, T. Detwiler, A. J. Stark, Y. T. Hsueh, and S. E. Ralph, “Inter-channel crosstalk cancellation for Nyquist-WDM superchannel applications,” *J. Lightwave Technol.*, vol. 30, no. 24, pp. 3993-3999, Dec. 2012.

[87]. F. Pancaldi, G. M. Vitetta, R. Kalbasi, N. Al-Dhahir, M. Uysal and H. Mheidat, “Single-carrier frequency domain equalization,” *IEEE Signal Processing Mag.*, vol. 25, no. 5, pp. 37-56, Sep. 2008.

[88]. ETSI, “Mobile Edge Computing a Key Technology Towards 5G,” ETSI White Paper (2015).

[89]. R. Puerta, M. Agustin, L. Chorchos, J. Tonski, J.-R. Kropp, N. Ledentsov, V. A. Shchukin, N. N. Ledentsov, R. Henker, I. T. Monroy, J. J. V. Olmos, and J. P. Turkiewicz, “107.5 Gb/s 850 nm Multi- and Single-Mode VCSEL Transmission over 10 and 100 m of Multi-Mode Fiber,” in *Proc. OFC*, Mar. 2016, paper Th5B.5.

[90]. L. Zhang, Q. Zhang, T. Zuo, E. Zhou, G. N. Liu, and X. Xu, "C-band Single Wavelength 100-Gb/s IM-DD Transmission over 80-km SMF without CD Compensation Using SSB-DMT," in *Proc. OFC*, Mar. 2015, paper Th4A.2.

[91]. L. Goldfeld, V. Lyandres, and D. Wulich. "Minimum BER Power Loading for OFDM in Fading Channel" *IEEE Trans. Commun.*, Vol. 50, no. 11, pp. 1729-1733, Nov. 2002.

[92]. W. R. Peng, B. Zhang, K. M. Feng, X. Wu, A. E. Willner, and S. Chi, "Spectrally efficient direct-detected OFDM transmission incorporating a tunable frequency gap and an iterative detection techniques," *J. Lightwave Technol.*, vol. 27, no. 24, pp. 5723-5735, Dec. 2009.

[93]. A. Pizzinat, P. Chanclou, T. Diallo, and F. Saliou, "Things you should know about fronthaul (Invited Paper)," in *Proc. ECOC*, Sep. 2014, paper Tu.4.2.1.

[94]. Y. Wang, J. Yu, and N. Chi, "Demonstration of 4×128-Gb/s DFT-S OFDM signal transmission over 320-km SMF with IM/DD," *IEEE Photon. J.*, vol. 8, no. 2, pp. 1-9, Apr. 2016.

[95]. D. J. Thomson, F. Y. Gardes, S. Liu, H. Porte, L. Zimmermann, J.-M. Fedeli, Y. Hu, M. Nedeljkovic, X. Yang, P. Petropoulos, and G. Z. Mashanovich, "High performance Mach–Zehnder-based silicon optical modulators," *IEEE J. Select. Topics Quantum Electron.*, vol. 19, no. 6, pp. 85-94, Nov. 2013.

[96]. D. Qian, N. Cvijetic, J. Hu, and T. Wang, "108 Gb/s OFDMA-PON with polarization multiplexing and direct detection," *J. Lightwave Technol.*, vol. 28, no. 4, pp. 484-493, Feb. 2010.

[97]. P. T. Dat, A. Kanno, and T. Kawanishi, “Bidirectional transmission of LTE-A carrier aggregation signal over a seamless fiber-wireless system in W-Band,” in *Proc. OFC*, Mar. 2015, paper W1F.5.

[98]. M. Xu, J. Zhang, F. Lu, Y. Wang, D. Guidotti, and G.-K. Chang, “Investigation of FBMC in mobile fronthaul networks for 5G wireless with time-frequency modulation adaptation,” in *Proc. OFC*, Mar. 2016, paper W3C.2.

[99]. H. Shariatmadari, R. Ratasuk, S. Iraji, A. Laya, T. Taleb, R. Jäntti, A. Ghosh, “Machine-type communications: current status and future perspectives toward 5G systems,” *IEEE Commun. Mag*., vol.53, no.9, pp. 10-17, May 2015.

[100]. S.-Y. Jung, S.-M. Jung, and S.-K. Han, “AMO-FBMC for asynchronous heterogeneous signal integrated optical transmission,” *IEEE Photon. Technol. Lett*., vol.27, no.2, pp. 133-136, Jan. 2015.

[101]. K. Fazel and S. Kaiser, *Multi-Carrier and Spread Spectrum Systems*. Hoboken, NJ: John Wiley & Sons, 2003, pp. 65-105.

[102]. T. Keller and L. Hanzo, “Adaptive modulation techniques for duplex OFDM transmission,” *IEEE Trans. Veh. Technol*., vol. 49, no. 5, pp. 1893-1906, Sep. 2000.

[103]. E. Kofidis, D. Katselis, A. Rontogiannis, and S. Theodoridis, “Preamble-based channel estimation in OFDM/OQAM systems: a review,” *Elsevier Signal Processing*, vol. 93, no. 7, pp. 2038-2054, Jul. 2013.